MEASUREMENT OF THE B_S MESON LIFETIME

Yi Cen

A DISSERTATION

in

PHYSICS

Presented to the Graduate Faculty of the University of Pennsylvania in Partial Fulfillment of the Requirements for the Degree of Doctor of Philosophy

1994

Supervisor of Dissertation

Graduate Group Chairman

ACKNOWLEDGMENTS

This work would not have been possible without the support of a large number of collaborators, associates, and friends. I owe a deep debt of gratitude to my advisor, Professor Bob Hollebeek, who introduced me into the field of experimental particle physics, gave me the freedom to pursue my interests and guided me towards a successful end to my graduate studies. I also owe an especially deep debt of gratitude to Professor Brig Williams. His amazing scientific talent and keen insight have been a source of inspiration. None of this research would have been possible had he not guided and fostered my scientific pursuits. I also deeply thank Professor Larry Gladney. In all these years he has acted as an invaluable source of scientific and academic advice. I am also very grateful to Professor Nigel Lockyer, the chairman of my thesis committee, for his constant encouragement, friendship and personal advice. I also thank the other members of my doctoral committee, Professors P. Langacker and J. Dolan for comments and suggestions.

I have been very fortunate to know and work with Dr. F. Ukegawa. His contribution and knowledge have made this work possible. I would like to give special thanks to Dr. G. Unal whose talent in physics has provided valuable input to many of our discussions. I would also like to thank my CDF collaborators and the members of the technical staff at Fermilab for their many contributions. Lastly and most importantly, I wish to thank Miss Ping Han for her love and support that have made my time at

university of pennsylvania much more enjoyable.

ABSTRACT

MEASUREMENT OF THE B_S MESON LIFETIME

Yi Cen

Robert Hollebeek

This thesis presents the measurement of the strange B meson (B_s) lifetime. The lifetime of the bottom hadron is largely determined by the weak decay of the bottom quark and is closely related to the Cabibbo-Kobayashi-Maskawa (CKM) matrix element V_{cb}. The naive spectator decay model gives a universal lifetime for all the bottom hadrons. The lifetime of the individual B hadron species can provide knowledge of the bottom hadron decay beyond the spectator picture. B_s mesons are produced from the $p\bar{p}$ collisions in the Fermilab Tevatron at a center-of-mass energy of 1.8 TeV. Using the CDF detector, semileptonic decays of the B_s meson are partially reconstructed by identifying events containing a lepton with an associated D_s^- meson. A sample of 76 $\ell^+D_s^-$ signal events with decay vertices inside the silicon microvertex detector are selected from the data collected during 1992-1993. From these events, the B_s lifetime has been measured to be

$$\tau_s = 1.42\ ^{+0.27}_{-0.23}\ (\mathrm{stat})\ ^{+0.11}_{-0.11}\ (\mathrm{syst})\ \mathrm{ps}.$$

This is the current best measurement of the B_s lifetime in the world.

Contents

List of Tables

List of Figures

Chapter 1

Introduction

1.1 Bottom Lifetime and V_{cb}

The bottom hadron's lifetime was first measured by the MARKII[1] and MAC[2] experiments in 1983. They inferred from the impact parameter distribution of prompt leptons produced in high energy e^+e^- annihilation that the bottom hadron lifetime was about 1 pico-second long. The weak decay of the B hadrons can be most naively thought of as the beta decay of a free bottom quark (see Figure 1.1). The study of the lepton spectrum from the $\Upsilon(4S)$ experimental data[3] shows that the bottom

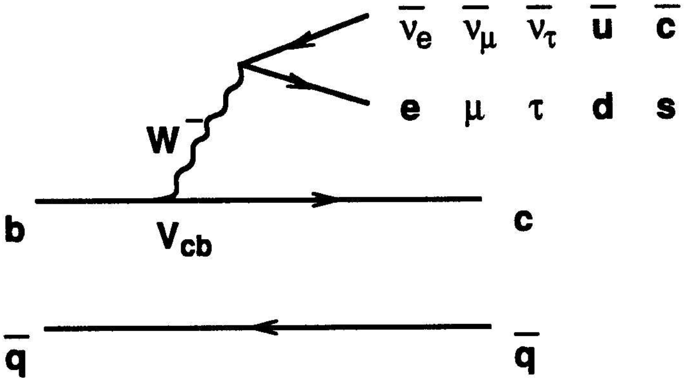

Figure 1.1: A spectator picture of the bottom hadron decay

quark decays predominantly to charm quark. The $b \rightarrow u$ transition is very small ($|V_{ub}|^2/|V_{cb}|^2 \sim 10^{-2} << 1$). The bottom quark lifetime τ_b can be compared to the muon lifetime,

$$\tau_\mu = \frac{192\pi^3}{G_F^2 m_u^5}. \tag{1.1}$$

The following two additions have to be considered: The V-A charge current of $\bar{b}\gamma^\lambda(1-\gamma^5)c$ is multiplied by the CKM matrix element V_{cb}. There are nine Cabibbo-allowed channels into which the W can decay, i.e.

$$b \rightarrow c(\ e\bar{\nu}_e,\ \mu\bar{\nu}_\mu,\ \tau\bar{\nu}_\tau,\ \text{or } \mathbf{d\bar{u}},\ \mathbf{s\bar{c}})$$

Three of them are lepton channels and six (counting three colors) are the hadron channels. The lifetime τ_b is related to the total width by

$$\frac{1}{\tau_b} = \Gamma_{\text{tot}} \simeq 5.8\frac{G_F^2 m_b^5}{192\pi^3}|V_{cb}|^2 F(\epsilon) \tag{1.2}$$

where $F(\epsilon)$ is the phase space factor given by $F(\epsilon) = 1 - 8\epsilon^2 + \epsilon^6 - \epsilon^8 - 24\epsilon^4 \ln\epsilon$ and $\epsilon \equiv m_c/m_b$. Because of the extra phase space suppression ($\sim$ 10-20%) suffered by the $\tau\bar{\nu}_\tau$ and the $\mathbf{s\bar{c}}$ relative to the others due to heavier masses of the τ and c, the contribution from all channels gives the factor ~ 5.8 instead of 9. The corresponding lifetime for a bottom mass of 4.95 GeV/c^2 and a charm quark mass of 1.55 GeV/c^2 is:

$$\tau_b \simeq 1.8 \times (\frac{0.05}{|V_{cb}|})^2 \text{ ps}. \tag{1.3}$$

This naive model is commonly referred to as the spectator model. It leads to a unique lifetime (the bottom quark lifetime) for all the bottom hadrons. The scale of the average B^1 lifetime is set by the formula (1.3).

The measurement of the average B lifetime has been pursed by many experiments. Table 1.1 lists only the recent results from LEP and CDF. They are separated into three different groups according to the type of data sample used. In addition to the method of fitting the lepton impact parameter distribution to measure the B lifetime, there are other techniques including the direct vertex measurement (see Table 1.1 column 'Channel'). The combined world lifetime result has an uncertainty of less than 3%.

The bottom lifetime is useful for measuring the magnitude of the CKM matrix element V_{cb}. To avoid the uncertainty in calculating the hadronic decays, most often the semileptonic partial width is used,

$$\Gamma_{sel} = \frac{\mathcal{B}_{sel}}{\tau_b} = \frac{G_F^2 m_b^5}{192\pi^3} V_{cb}^2 F(\epsilon). \tag{1.4}$$

V_{cb} can thus be obtained from the measurement of the lifetime τ_b, semileptonic branching ratio $\mathcal{B}_{sel}$, and from the knowledge of the bottom quark mass m_b. The measurement error is thus

$$\frac{\Delta|V_{cb}|^2}{|V_{cb}|^2} \simeq \frac{\Delta\tau_b}{\tau_b} \oplus \frac{\Delta\mathcal{B}_{sel}}{\mathcal{B}_{sel}} \oplus \frac{\Delta(m_b^5 F(\epsilon))}{m_b^5 F(\epsilon)} \tag{1.5}$$

where $\Delta\mathcal{B}_{sel}/\mathcal{B}_{sel} \sim 3\%$ and the $\Delta m_b^5 F(\epsilon)/(m_b^5 F(\epsilon)) \sim 15\%$. The dominant uncertainty

---

[1] B usually stands for mesons or hadrons while lower case b is often referred to quark.

Table 1.1: A list of the recent average B lifetime measurements

Expt.	Ref.	Channel	Lifetime (ps)
ALEPH	Marseille-92	vertex	$1.41\ ^{+0.13}_{-0.12}\ \pm 0.04$
DELPHI	DN 93-85	vertex	$1.34\ ^{+0.19}_{-0.15}\ \pm 0.08$
OPAL	PLB266,485	vertex	$1.32\ ^{+0.31}_{-0.25}\ \pm 0.15$
CDF	PRL/93-71	vertex	$1.46\ \pm 0.06\ \pm 0.06$
	Average	$B \to J/\psi$	$1.430\ \pm 0.065$
ALEPH	PLB295,174	2D e, μ IP	$1.49\ \pm 0.03\ \pm 0.06$
ALEPH	Marseille-92	3D e, μ IP	$1.487\ \pm 0.023\ \pm 0.038$
DELPHI	DN 93-83	2D μ IP	$1.37\ \pm 0.05\ \pm 0.05$
L3	Connel-91	2D e, μ IP.	$1.518\ \pm 0.035\ \pm 0.032$
OPAL	PPE/93-92	2D e, μ IP.	$1.523\ \pm 0.034\ \pm 0.038$
	Average	$B \to \ell X$	$1.499\ \pm 0.043$
ALEPH	PPE/93-116	$r\phi$ dipole	$1.511\ \pm 0.022\ \pm 0.078$
DELPHI	DN 93-84	Vertex	$1.612\ \pm 0.014\ \pm 0.048$
DELPHI	DN 93-83	2D hadron IP.	$1.41\ \pm 0.04\ \pm 0.05$
DELPHI	DN 93-94	Topological Vertices	$1.59\ \pm 0.06\ \pm 0.09$
	Average	$B \to$ hadrons	$1.564\ \pm 0.060$
	Combined	J/ψ+lepton+hadron	$1.489\ \pm 0.038$

here is the bottom quark mass. The current V_{cb} value is $0.037 \pm 0.005 \pm 0.004$[4].

1.2 Beyond the Spectator Picture

The spectator model implies that the lifetimes of hadrons containing a heavy quark should not depend on the kind or number of light quarks in the hadron. Historically, the large difference between the lifetimes for charged and neutral D mesons demonstrates that this naive picture is not correct for charm decay[5]. In fact, among different types of charm hadrons, the following pattern exists:

$$2\tau(\Lambda_c) < \tau(D^0) \sim \tau(D_s^+) < \frac{1}{2}\,\tau(D^+) \tag{1.6}$$

Various theoretical explanations include either nonspectator processes or the interference between internal and external spectator diagrams. These explanations are also applicable to the bottom hadron decays.

- The t-channel W-exchange process shown in Figure 1.2 only exists for the neutral B mesons and the Λ_b. This could conceivably reduce $\tau(B_d)$, $\tau(B_s)$ and $\tau(\Lambda_b)$ relative to the charged B mesons.

- There are two spectator diagrams, external and internal, as shown in Figure 1.3 for a charged B meson decay. In the external diagram, the quarks produced by the W^- decay hadronize separately from the spectator quark and c quark from b quark, while in the internal diagram, they are 'color mixed' with the spectator quark and c quark. Since the final states in these two diagrams have identical flavor, the diagrams can interfere.

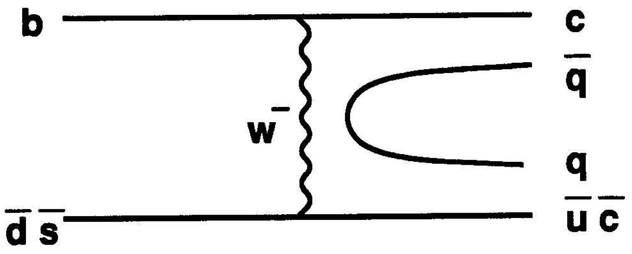

Figure 1.2: A t-channel W exchange diagram for the neutral B and Λ_b.

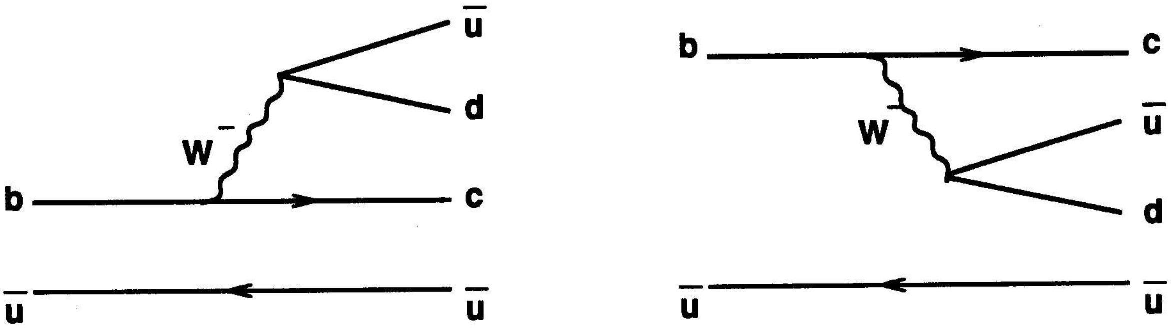

Figure 1.3: Two spectator, diagrams in the B_u hadronic decay which have the same final hadron states. They interfere with each other.

It is generally believed however that as the mass of the heavy quark increases, the lifetime of the different hadrons carrying the same heavy flavor should approach each other. In the bottom case, one would expect only 10-20% difference among all types of B hadrons[6]. The most recent calculations have suggested[7]

$$\frac{\tau(B_u^+)}{\tau(B_{d,s}^0)} \simeq 1 + 0.05\frac{f_B}{(200MeV)^2}, \tag{1.7}$$

where f_B is the B meson decay constant is estimated to be $f_B \approx 183 \pm 26$ MeV. Different B hadron lifetimes are also expected to follow the hierarchy,

$$\tau(\Lambda_b) < \tau(B_s) \sim \tau(B_d) < \tau(B_u). \tag{1.8}$$

Table 1.2: A list of recent B^+ and B^0 lifetime measurements

Expt.	Ref.	Channel	Lifetime (ps)	
			B^+	B^0
ALEPH	PPE/93-42	$\ell^+ D^0, \ell^+ D^{(*)-}$	$1.47\ ^{+0.22}_{-0.19}\ ^{+0.15}_{-0.14}$	$1.51\ ^{+0.20}_{-0.10}\ ^{+0.07}_{-0.13}$
DELPHI	ZPC57,181	$\ell^+ D^0, \ell^+ D^{(*)-}$	$1.30\ ^{+0.33}_{-0.29} \pm 0.16$	$1.17\ ^{+0.29}_{-0.23} \pm 0.16$
OPAL	OPN-106	$\ell^+ D^0, \ell^+ D^{(*)-}$	$1.66\ ^{+0.20}_{-0.20}\ ^{+0.11}_{-0.12}$	$1.63\ ^{+0.14}_{-0.14}\ ^{+0.10}_{-0.11}$
ALEPH	Marseille-93	$J/\psi K^+, D^{(*)} n\pi$	$1.77\ ^{+0.45}_{-0.34} \pm 0.14$	$1.19\ ^{+0.43}_{-0.29} \pm 0.14$
DELPHI	DN 93-94	topological	$1.81\ ^{+0.12}_{-0.12} \pm 0.19$	$1.37\ ^{+0.15}_{-0.15} \pm 0.21$
CDF	Moriond-94	$J/\psi X_s^+, J/\psi X_s^0$	$1.61\ ^{+0.16}_{-0.16} \pm 0.05$	$1.57\ ^{+0.18}_{-0.18} \pm 0.08$
	Average		1.64 ± 0.11	1.50 ± 0.10

The first direct neutral B_d lifetime $\tau(B_d)$ was measured with large statistical error by the MARKII experiment using the $\ell^- D^{*+}$ events[8]. Significant improvements on the neutral B_d and charged B_u lifetimes were made by the LEP and CDF experiments. A list of the most recent B_u^+ and B_d^0 lifetime measurements are shown in Table 1.2. The relative uncertainty has been reduced below 10% which is comparable to the expected difference. No significant deviation has yet been seen in the experiment.

1.3 B_s Meson Lifetime

Besides the interest in the lifetime hierarchy, there is another aspect which makes the B_s lifetime interesting. It is well known that in the neutral kaon system, the two CP eigenstates $K_{\mathbf{short}}$ (CP = +) and $K_{\mathbf{long}}$ (CP = −), have quite different lifetimes. Such a phenomena could also exist in the B_s system. Here the two CP states

$$B_{\mathbf{short,long}} = \frac{1}{\sqrt{2}}(B_s^0 \mp \overline{B}_s^0)(\text{ CP} = \pm), \tag{1.9}$$

are expected to have slightly different decay widths. A recent parton model calculation gave[7]

$$\frac{\Delta\Gamma(B_s)}{\Gamma(B_s)} \simeq 0.18 \frac{f_{B_s}^2}{(200MeV)^2}. \tag{1.10}$$

and another estimate based on the exclusive decay summation also suggested 15% splitting in the width[9]. This means that the lifetime difference between the so-called 'long' and 'short' B_s mesons is actually comparable to or even larger than the difference between the B_u and B_d.

Because the production cross section of the B_s meson is much smaller ($\sim 1/3$) than the other B mesons (B_u and B_d), the B_s lifetime has been measured so far with very limited statistics by the ALEPH[10],DELPHI[11] and OPAL[12] experiments. In fact the B_s meson mass was only determined a year ago by CDF[13, 14] and three LEP experiments[15]. Table 1.3 lists the recent values of the B_s mass from CDF, ALEPH and DELPHI. The objective of this thesis is to measure the lifetime of the B_s meson at the CDF with more statistics.

Experiment	Final states	Events	Mass [MeV/c^2]
ALEPH	$\psi'\phi$	1	
	$D_s^+\pi^-$	1	$5368.6 \pm 5.6(stat.) \pm 1.5(syst.)$
DELPHI	$D_s^-\pi^+$	1	
	$D_s^-a_1^+$	1	
	$J/\psi\phi$	1	$5374 \pm 16(stat.) \pm 2(syst.)$
CDF	$J/\psi\phi$	33 ± 7	$5367.7 \pm 2.4(stat.) \pm 4.8(syst.)$
Average			5368.4 ± 3.8

Table 1.3: A list of recent B_s meson mass measurements.

Heavy quarks are copiously produced in the hadron-hadron collisions[16]. The leading order QCD diagrams for the heavy quark pair $Q\overline{Q}$ production are shown in Figure 1.4 and 1.5. They can be compared with the $e^+ + e^- \rightarrow Q + \overline{Q}$ process shown in Figure 1.6. The total cross section of the $b\bar{b}$ production at Tevatron is estimated to be ~ 50 μb. This is almost four orders of magnitude higher than the cross section at LEP. Although the background of light quarks from QCD production is enormous, the bottom events can be separated from the background events by requiring leptons which come primarily from heavy quark decays.

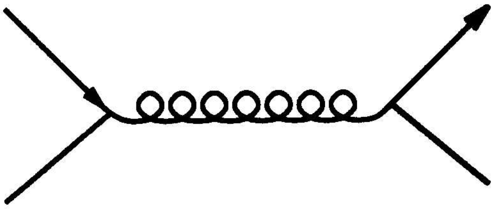

Figure 1.4: The lowest-order diagram for the $q\overline{q} \rightarrow Q\overline{Q}$ process .

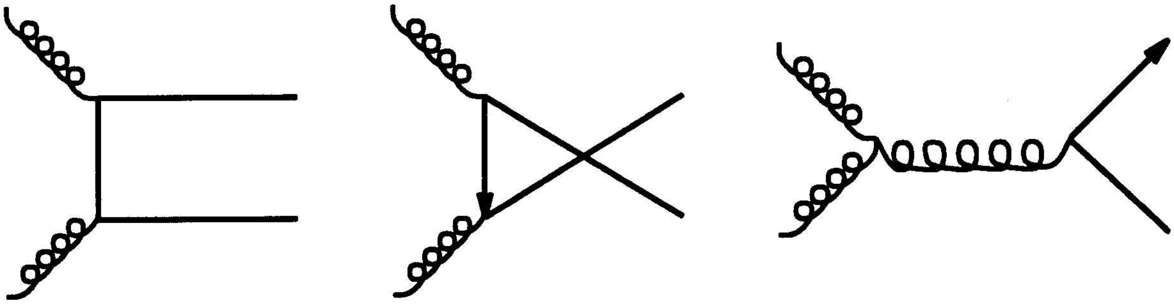

Figure 1.5: Lowest-order diagrams for the $g\overline{g} \rightarrow Q\overline{Q}$ process.

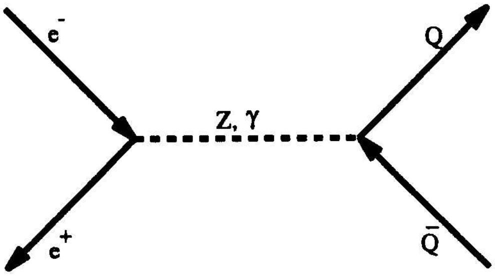

Figure 1.6: The lowest-order diagram for the $e^{-}e^{+} \rightarrow Q\overline{Q}$ process.

In this thesis, the semileptonic decay channel of the B_s[17]

$$B_s \rightarrow \ell^+ D_s^- \nu X \tag{1.11}$$

will be used, which is expected to have a branching ratio of ~ 8-10% similar to the other B mesons. The semileptonic decay provides large statistics. The associated production of the $\ell^+ D_s^-$ is a clean signature for the B_s meson and the decay vertex of the event can be reconstructed from the lepton and the D_s trajectories. The lifetime of the B_s can then be determined from the fit of its decay length distribution. The organization of the rest of the thesis is the following: brief introduction to the CDF detector, description of the tools for the analysis, identification of a lepton, reconstruction of the D_s meson, measurement of the vertices and decay lengths, study of the data sample, fitting the lifetime, systematics discussion and the final conclusion.

Chapter 2

CDF detector

The CDF detector is located at the $B\Phi$ collision point of the Tevatron ring as shown in figure 2.1 where 6 bunches of protons and antiprotons are circulating in opposite directions. In this chapter we will describe the detector components of CDF.

The CDF detector is a general-purpose detector which was designed to study the physics of $p\bar{p}$ collisions at a center-of-mass energy of 1.8 TeV[18]. It has both azimuthal and forward-backward symmetry and covers almost the entire solid angle (see Figure 2.2). In the central region a superconducting solenoid of length 4.8 m and radius 1.5 m provides a 1.5-Tesla magnetic field. Inside there are three tracking chambers, SVX, VTX, CTC as indicated in the detector side-view Figure 2.3. The momentum of charged particles can be measured with these detectors. Surrounding the solenoid are sampling calorimeters (CEM, CHA etc.) which were built to contain and measure the electromagnetic and hadronic energy of the electrons, photons and jets. There are three sets of the drift chambers (CMU, CMP and CMX) outside the

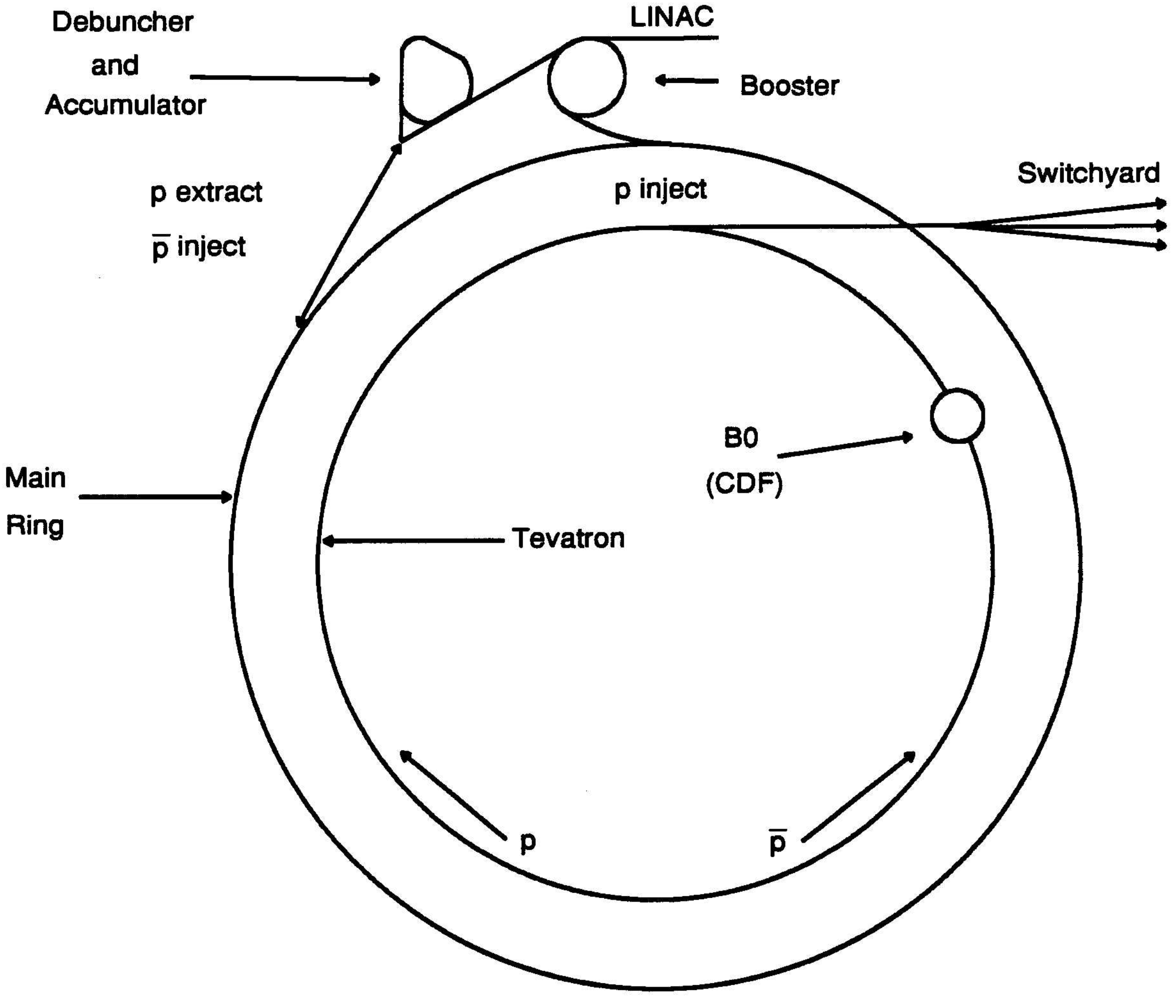

Figure 2.1: A top view of the Tevatron rings and the BΦ collision point

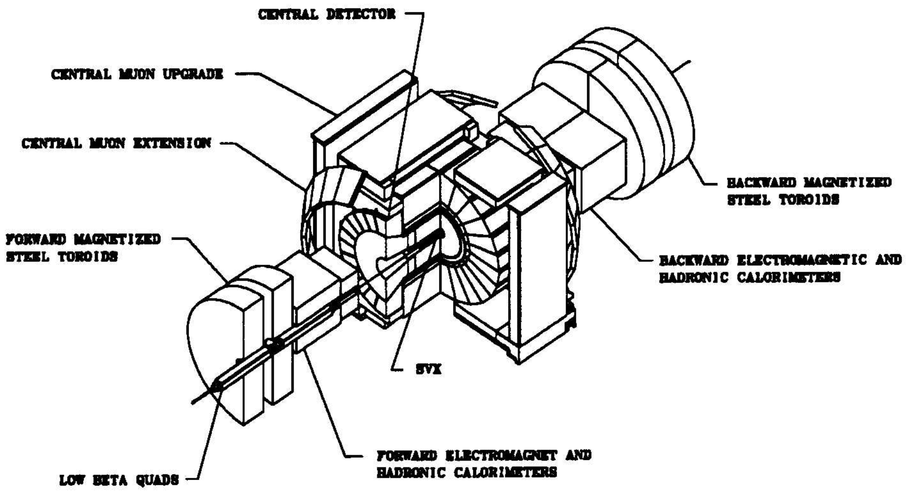

Figure 2.2: A three-dimensional view of the CDF detector

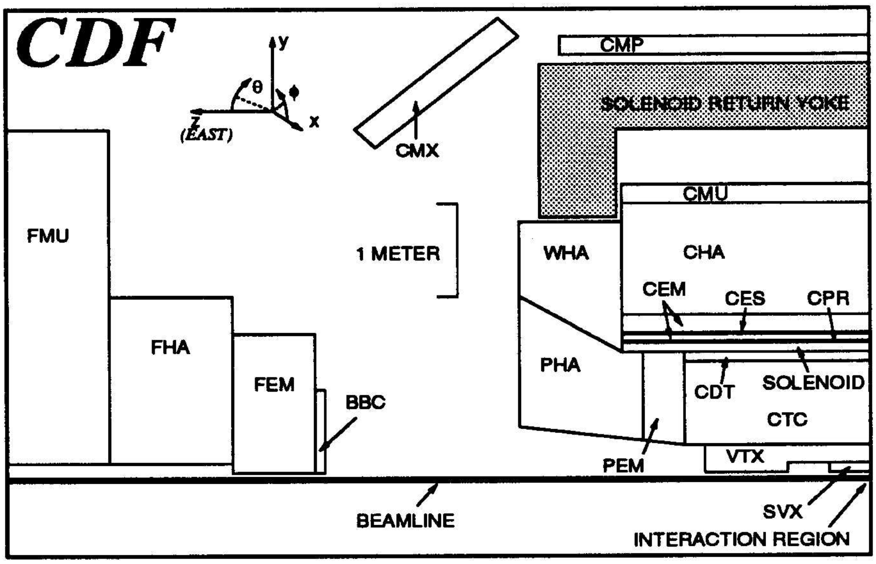

Figure 2.3: A side-view of the CDF detector

calorimeters which are used to detect muons. Of all the features of this detector, the most important ones for this analysis are charged particle tracking and lepton identification in the central region ($1 < \eta < 1$). We are going to describe these components in the following section.

2.1 Silicon Vertex Detector

Surrounding the 1.9 cm radius beryllium beampipe is the silicon vertex detector (SVX) which was installed in 1992, the first time for precision vertex measurement at a hadron collision machine[19]. It consists of four concentric cylindrical layers of silicon strip detectors located at radii between 3.0 and 7.9 cm outside the beam pipe. These detectors are arranged as a twelve sided barrel at each radial position. Each slice of 30 deg is called a wedge. There are two modules placed along the beam axis with a gap of 2.15 cm in the middle. A picture of one module is shown in Figure 2.4. The active region along the beam is 51 cm which covers about 60% of $\bar{p}p$ collisions as the width of the $p\bar{p}$ interaction vertex along the beam is about 30 cm.

Each silicon strip detector consists of a 300 μm thick silicon single crystal with aluminum readout strips on top parallel to the beam axis. The pitch between readout strips is 60 μm for the inner 3 layers and 55 μm for the most out layer. The detectors are electrically bonded to each other along the beam in groups of three. At each radius of each of the twelve wedges, there are thus a total of six those detectors, in two groups

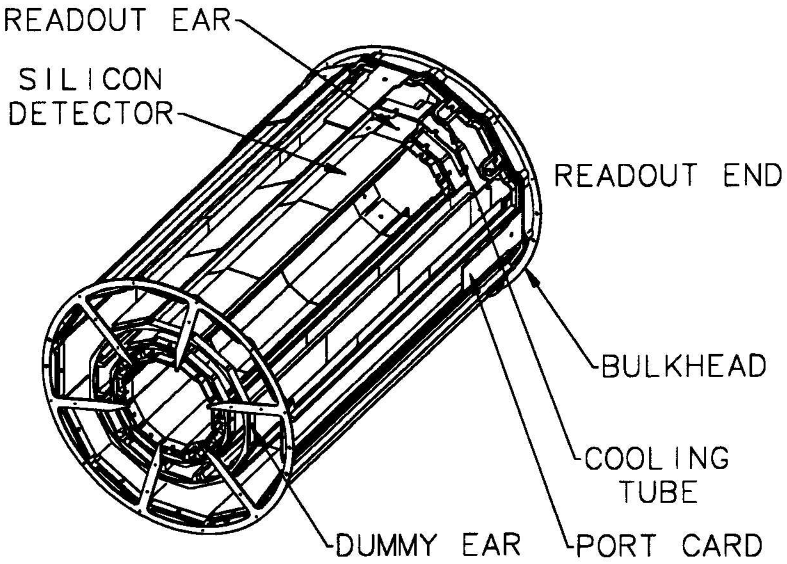

Figure 2.4: A draw of the one SVX barrel

of three with readout from both outside ends (three of them are shown in Figure 2.4). The readout chips are DC coupled. Table 2.1 lists some of those basic geometry constants for each SVX wedge. The SVX provides precision track reconstruction in the plane transverse to the beam. The SVX single-hit spatial resolution is measured in data to be $\sigma \sim 13$ μm.

2.2 Vertex Time Projection Chamber

Outside the SVX is a time projection vertex chamber (VTX), installed in 1992, which provides the measurement of the $p\bar{p}$ interaction vertex along the z axis with a resolution of 1 mm. It extends the tracking up to radius of 22 cm and also connects to the

Table 2.1: A set of SVX geometry constants

Layer	Radius (cm)	Thickness (μm)	Pitch (μm)	readout strips
1	3.005	300	60	256
2	4.256	300	60	384
3	5.687	300	60	512
4	7.866	300	55	768

central tracking chamber with its z measurement.

2.3 Central Tracking Chamber

The central tracking chamber (referred as the CTC) which sits outside the VTX, is a 3.2-m-long cylindrical drift chamber with an outer radius of 1.3 m. Shown in Figure 2.5 is the end view of the CTC. The CTC contains 84 concentric layers of sense wires arranged into 9 superlayers. Five of the superlayers (starts from inside 0, 2, 4, 6, 8), in which the wires are parallel to the beam line, each contain 12 sense wire layers. They provide the information in the r-ϕ plane. These five axial layers are interleaved with four superlayers of stereo wires (1, 3, 5, 7) in which the angle between the sense wires and the beam line alternates between ±3 deg. Each stereo superlayer contains 6 sense wire layers. The resolution of a stereo wire in the z coordinate, is $\sim$ 4 mm. Together, the axial and stereo wires provides tracking in the r-z plane.

Both axial and stereo superlayers are also divided into cells so that the maximum drift distance is less than 40 mm, corresponding to about 800 ns of drift time.

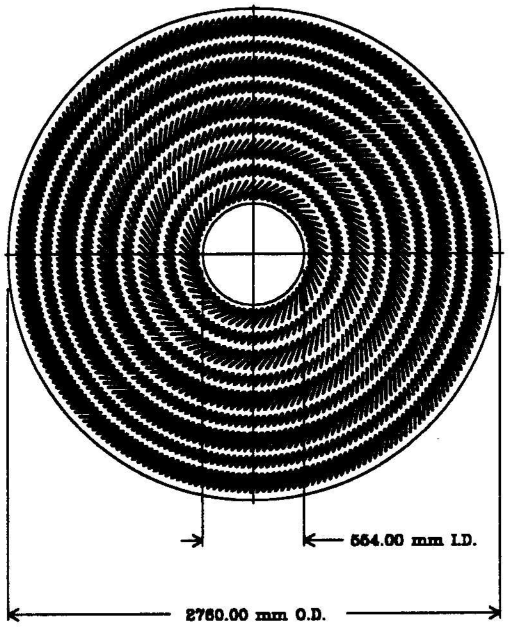

Figure 2.5: End view of the Central Tracking Chamber showing the superlayers and the cells

2.4 Central Electromagnetic Calorimeters

The central calorimeter outside the solenoid covers $|\eta| < 1.1$ region and has two components, the electromagnetic (CEM) in front and the hadronic behind (CHA). They are segmented in azimuth of 15 deg and pseudorapidity of 0.11 to form a projective tower geometry which points back to the nominal interaction point.

The CEM consists of alternating layers of scintillator sampling medium and lead

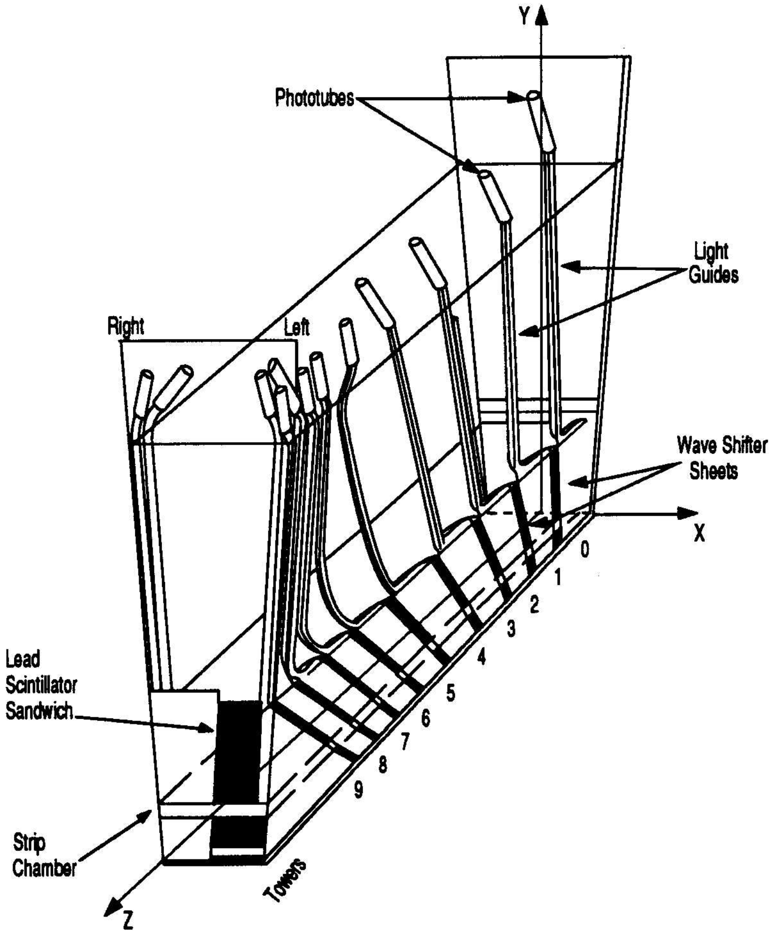

Figure 2.6: Schematics of the wedge module of the central calorimeter

sheet absorbers corresponding to a total of 16 radiation lengths (X_0). It has 24 modules in azimuth on each side of the beam direction and each those modules(called 'wedge') contains 10 towers. A typical size of a tower cell is 46 cm in r-ϕ (x) and 24 cm along the beam direction (z). Figure 2.6 is a schematic of the wedge module of the central calorimeter.

Located at $5.9X_0$ depth within the CEM, where electromagnetic showers are expected to be at their maximum, is one layer of wire proportional chambers (indicated as the CES in Figure 2.3) with the orthogonal strips and wires readout. The strip chambers determine the electromagnetic shower position and transverse development in both the z and r-ϕ view at the shower maximum.

In order to sample the early development of electromagnetic showers in the material of the coil which has $\sim 1X_0$, one layer of wire proportional chambers (indicated as the CPR in Figure 2.3) were also installed in between the solenoid and the CEM. These chambers provide the EM cluster information only in the r-ϕ view.

2.5 Central Muon Chambers

The central muon chambers (CMU) which cover $|\eta| < 0.6$ consist of four layers of drift chambers located outside the central hadronic calorimeter. Muons with $p_T > 1.4$ GeV/c must penetrate ~ 6 interaction lengths (CHA and magnet yoke) to reach the chamber. In 1992 another 0.6 m of steel was added behind the CMU for additional hadron absorption, and an additional four layers of drift chambers were added behind the steel to detect muons. This system is referred to as the central upgrade (CMP). About 84% of the solid angle are covered inside $|\eta| < 0.6$ by the CMU and 63% by CMP while 53% are covered by both chambers. In addition, the coverage of the central muon system has been extended to an η of 1.0 by additional muon chambers called CMX. We will use only CMU and CMP in this analysis.

Chapter 3

Tools

There are two different approaches to measure the B lifetime. The average B hadron lifetime can be inferred from the impact parameter distribution of prompt leptons. Those coming from B decays should have a mean impact parameter around the B lifetime ($c\tau \sim 450\ \mu$m). The second approach involves a direct measure of the decay length traveled by the B. Such a technique does not rely on Monte Carlo modeling of the background like the first approach and therefore has no biases. An even more appropriate way is to measure the individual lifetimes, in which case partial identification of the B hadron is necessary.

To measure the decay length, both the primary and the secondary decay vertices have to be determined with high precision. A typical B meson which passes the lepton trigger(see later) would have a minimum P_T of 15 GeV/c. It travels on an average about a tenth of a cm before it decays. In order to get the lifetime measurement error down to the 10% level, the resolution on the decay length must be about 100 μm or better. This could not be accomplished easily by measurement in the central drift chamber alone. A high precision micro vertex detector is therefore needed.

In this chapter, the SVX tracking which links the CTC track and SVX clusters will be first introduced. Then vertex finding tools including the beam position and the common vertex fitting will be discussed. Finally, the Monte Carlo simulation module will be described.

3.1 Tracking with SVX

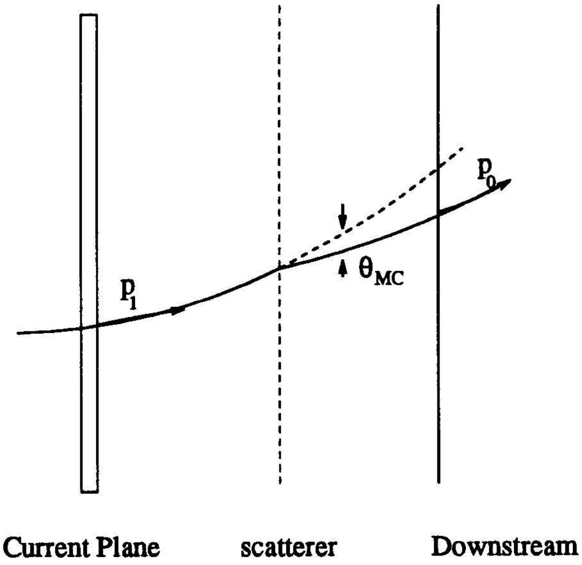

Figure 3.1: A picture of the progressive track fitting

The SVX is used to improve the tracking of the Central Tracking Chamber. An efficient tracking algorithm based on the track merging technique is implemented to link the existing tracks from CTC down towards the beam pipe progressively by incorporating new measurements from SVX.

As shown in Figure 3.1, a track fit $\vec{p}_0$ from a downstream detector can be considered as a good estimator for the track parameter $\vec{p}_1$ at the current measuring plane. Multiple scattering caused by the material in the middle does not affect this estimator because the scattering angle information can not be obtained from the downstream fit. Nevertheless the information loss due to multiple scattering changes the covariance matrix V_0. Taking into account the multiple scattering contribution, the covariance matrix has to be updated as $V_0' = V_0 + V_{MS}$. The matrix of the multiple scattering part, V_{MC}, can be expressed as,

$$(V_{MS})_{\alpha\beta} = \frac{\partial p_\alpha}{\partial \vec{\theta}} V_{MS}(\vec{\theta}, \vec{\theta}) \frac{\partial p_\beta}{\partial \vec{\theta}} \tag{3.1}$$

If a new cluster is found at the current layer, the fit is updated by minimizing the joint χ^2:

$$\chi'^2 = \chi_0^2 + (\Delta\vec{p})^t (V_0^*)^{-1} \Delta\vec{p} + \frac{(x(\vec{p}) - x')^2}{\sigma^2} \tag{3.2}$$

This χ^2 has one degree of freedom since it involves five direct measurements propagated from the downstream fit and a new measurement at current layer. The updated fit can be written as

$$\vec{p}_1 = \vec{p}_0 + [(V_0^*)^{-1} + A]^{-1} \frac{\partial x}{\partial \vec{p}} \frac{(x' - x(\vec{p}))}{\sigma^2} \tag{3.3}$$

and the covariance matrix is,

$$V_1 = [(V_0^*)^{-1} + A]^{-1} \tag{3.4}$$

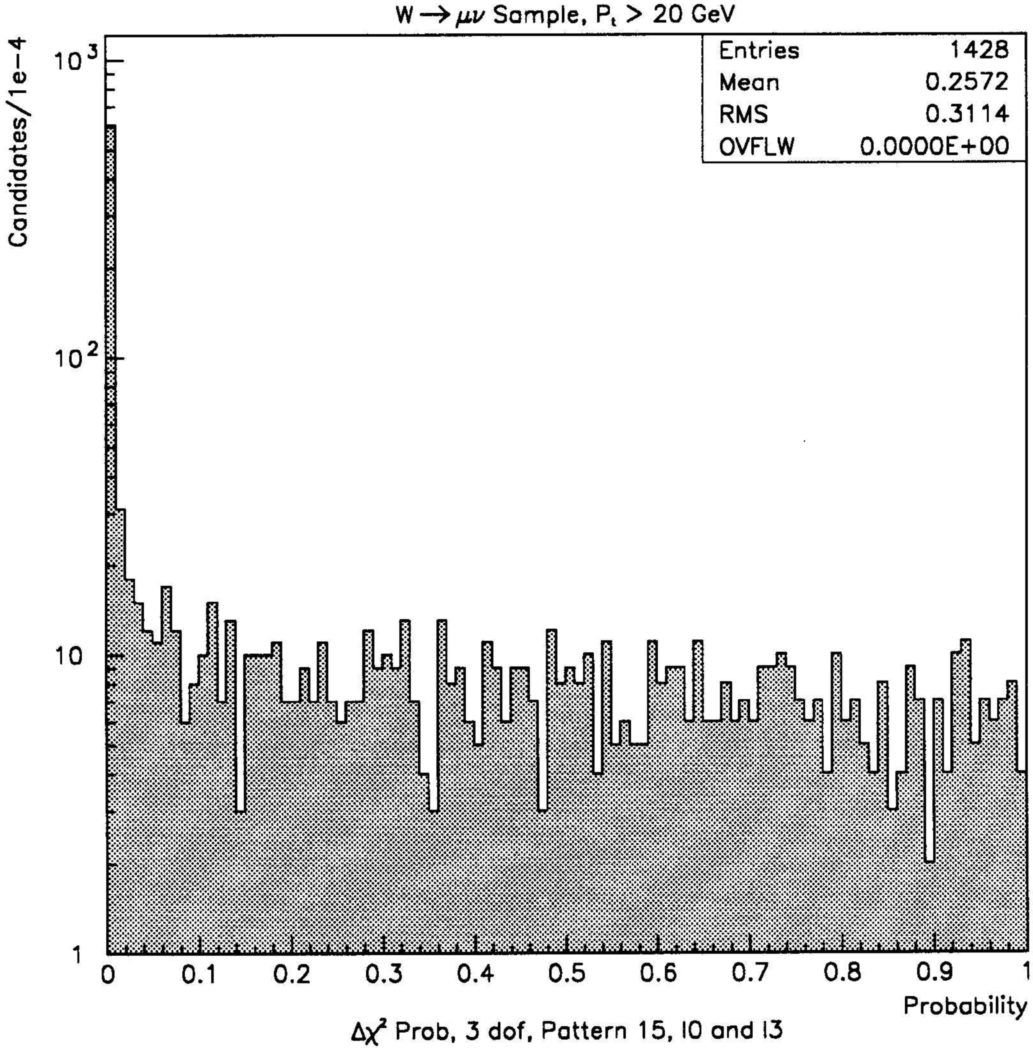

Figure 3.2: A $\delta\chi^2$ probability distribution, assuming 3 degrees of freedom between layers 0 and 3. Tracks are taken from a W muon sample to have 4 hits and $P_t > 20$ GeV/c.

where A is defined as:

$$A = \frac{1}{\sigma^2} \frac{\partial x}{\partial \vec{p}} \frac{\partial x}{\partial \vec{p}}. \tag{3.5}$$

The chi-square difference $\delta\chi^2$ between the lowest and highest hit layers are considered to have n-1 degrees of freedom where n is the number of hits. Shown in Figure 3.2, is the $\delta\chi^2$ probability distribution between layers 0 and 3 of the 4 hit tracks from the W muon sample where the number of degree of freedom is assumed to be 3. The flat distribution except at very small probability region suggests the correct degree of freedom. The $\delta\chi^2$ is a quantity which carries essentially only the information from SVX and has little bias from the CTC error.

SVX track candidates are selected based on the $\delta\chi^2$ as follows:

- A probability of $> 0.01\%$ for $\delta\chi^2$ is required for all except two hit track candidates.
- Among all the candidates which have the same hits, the one with the lowest total χ^2 is chosen over the rest.
- A 4 hit track is favored over a 3 hit track and 3 hit is favored over 2 hit candidate.

3.2 Study of Isolated Tracks

Electrons from the $W^- \rightarrow e^-\overline{\nu}_e$ and $Z \rightarrow e^+e^-$ are clean and well isolated. They serve as nice tools to study the tracking.

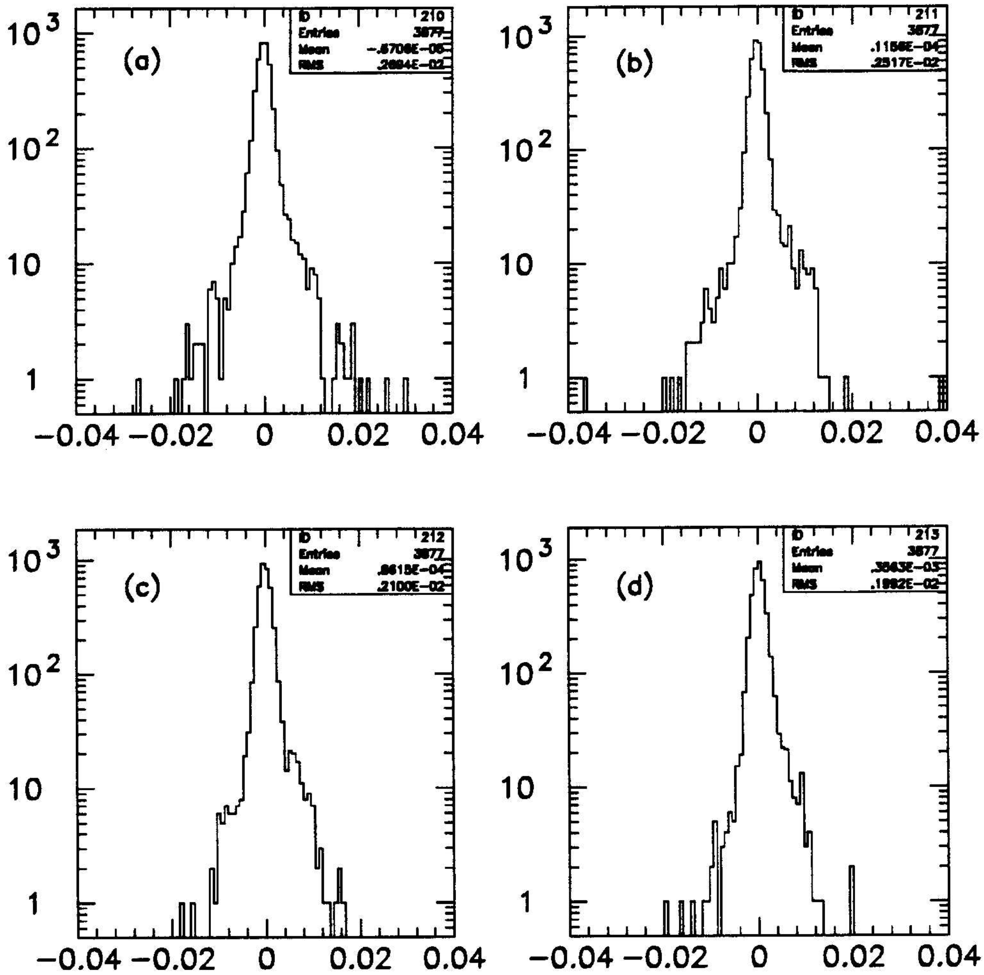

Figure 3.3: Residual distributions (unit of cm) of the 4 SVX layers for the W electrons.

3.2.1 Residual

To characterize the SVX tracking, a standard residual survey is done using the W electrons. The residual here is defined to be the distance between the center of the actual cluster used in the fit and the intersecting point of the track with the silicon plane. Figure 3.3 shows the residuals of W electrons from layer 0 to layer 3. Only those tracks with four SVX hits are plotted. All four layer residuals are consistent with having a narrow gaussian as a major part with σ of 10 μm and a few percent border tail contribution. Their rms values are less than 30 μm which can be compared to the actual cluster width of about 10 to 15 μm.

3.2.2 χ^2

As mentioned earlier, the χ^2 is a very important quantity to measure the quality of the track fit. A well behaved χ^2 should distribute like the standard chi-square function.

$$F(x) = \frac{x^{n/2-1}\exp(-\frac{x}{2})}{2^{n/2}\Gamma(n/2)} \tag{3.6}$$

In Figure 3.4 the chi-square distribution of four hit and three hit electron tracks from the W sample are plotted. The chi-square functions with 4 degree and 3 degree of freedom are fit to the data and superposed on the plot. It shows good agreement between the functions and the χ^2 distribution. In the 3 hit plot, the χ^2 is scaled up by 20% when fit to the function.

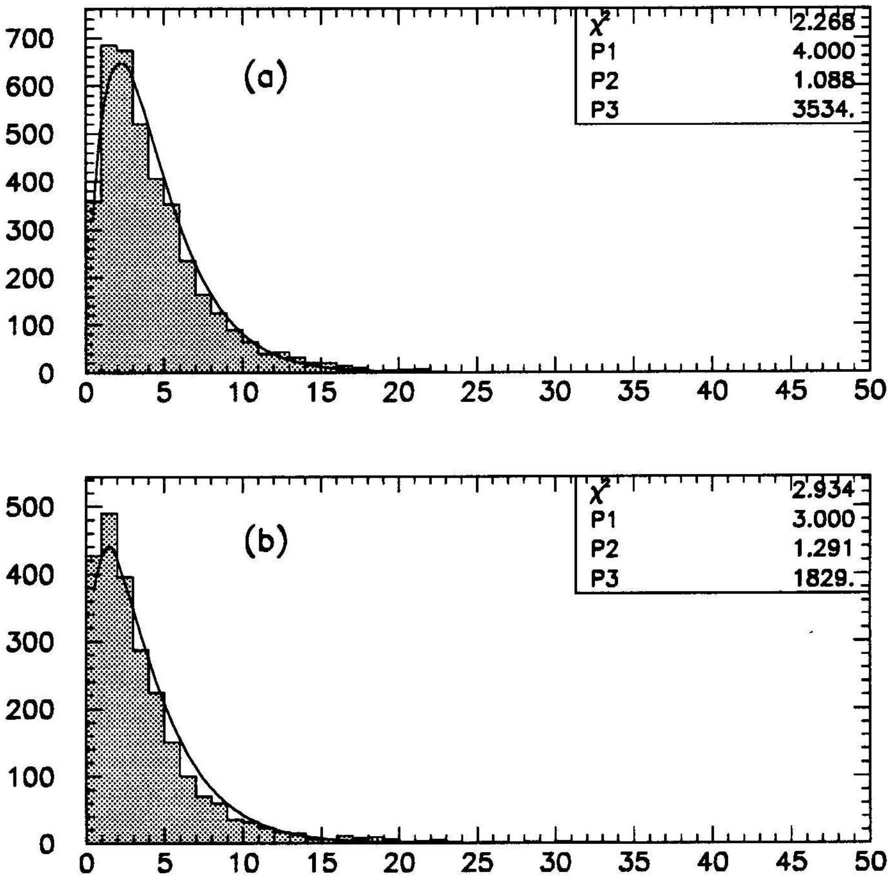

Figure 3.4: (a) χ^2 distribution of 4 hits electron tracks and a 4 *dof* chi-square function fit.(b) χ^2 distribution of 3 hits electron tracks and a 3 *dof* chi-square function fit.

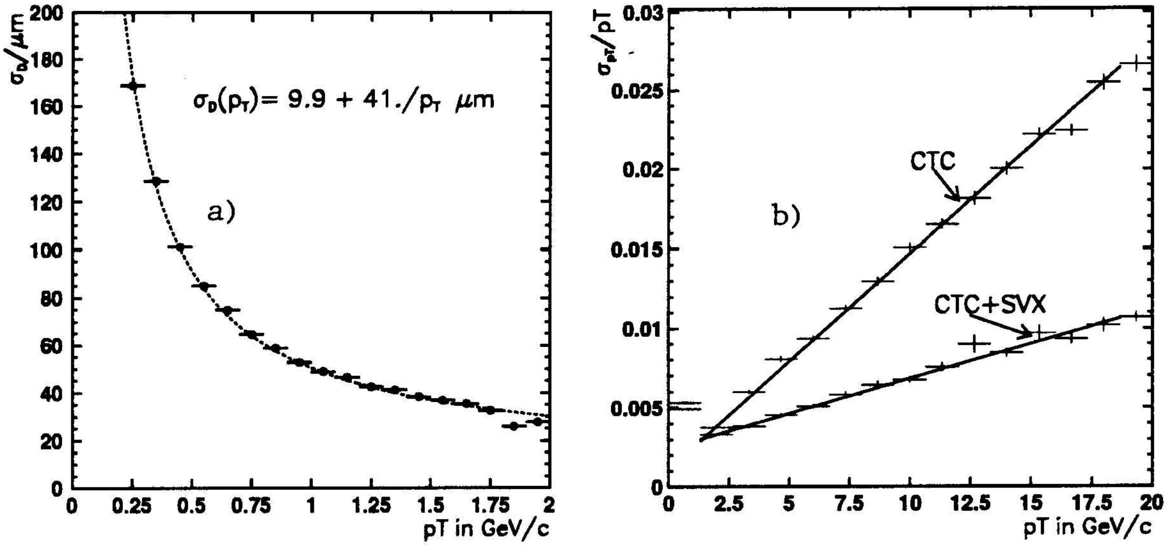

Figure 3.5: (a) Impact parameter resolution as a function of p_T obtained from data. (b)Improvement in momentum resolution of the tracking when SVX measurements are linked in.

3.2.3 Impact Parameter

SVX measures hits in two dimensional coordinates. One of the most important tracking improvements is to the impact parameter which is also the most relevant parameter for vertex fitting. The resolution of the impact parameter, σ_D, is limited by the vertex detector's intrinsic part σ_{in} and also by the multiple coulomb scattering effect which is proportional to the $1/p_T$. Figure 3.5(a) shows the impact parameter resolution as a function of the p_T measured from the data. It can be parameterized by the following form:

$$\sigma_D = A + \frac{B}{p_T} \tag{3.7}$$

with the asymptotic resolution of $A \simeq 10\ \mu\mathrm{m}$ and the p_T dependency $B = 41\ \mu\mathrm{m}\ \mathrm{GeV}/c$.

SVX also improves the curvature measurement as it extends the lever arm from CTC by about 30 cm with 2 or more hits. Shown in Figure 3.5(b) is the calculated error $\sigma(p_T)$ over p_T as a function of p_T. A linear parameterization

$$\sigma(p_T) = A + B \times p_T \tag{3.8}$$

gives $A = 0.11\%$ and $B = 0.14\%$ for the CTC only measurement. An improvement by SVX tracking gives $B = 0.044\%$ which is a factor of 3 better resolution.

3.3 The Primary Vertex

Unlike e^+e^- machines where the beam position has a big uncertainty in the x direction due to the synchrotron radiation by the electron, a proton beam spot is quite small and isotropic. Size of the beam spot in both the x and y direction are equal at about 36 to 38 μm. The z interaction point moves around the center with a width of 30 cm. The $x - y$ position shifts linearly corresponding to the z movement.

At CDF the beam position is determined for each run. The algorithm used is based on minimizing the χ^2 of the impact parameter, of all the primary tracks, i.e.

$$\chi^2(x_0, y_0, s_x, s_y) = \sum_{i=1}^{N} \frac{(d_i - d(\phi_0, z_0))^2}{\sigma_i^2} \tag{3.9}$$

where $\sigma_i^2 = \sigma_d^2 + 2\sigma_B^2$ and $d(\phi_0, z_0)$ is a linear function of the beam position,

$$d(\phi_0, z_0) = -(x_0 + s_x \cdot z_0) \cdot \sin\phi_0 + (y_0 + s_y \cdot z_0) \cdot \cos\phi_0 \tag{3.10}$$

(x_0, y_0) is the position of the beam at $z = 0$. s_x and s_y are the x and y slope of the beam.

In order to make a good fit of the beam, tracks are selected to have a minimum p_T of 1 GeV/c so as to reduce the multiple scattering error. All tracks are required to have 4 SVX hits and only travel through one detector barrel. Distance with respect to the nominal beam position is cut at 2 mm. An iterative procedure is used until 60% of the originally selected tracks survive. The beam profiles are shown in Figure 3.6. A distribution of the primary vertex with respect to the fitted beam position is shown in the x-y dimensional plot and a plot of projection to the x axis is show on the right side. It suggests a comparable resolution on both x and y direction and it shows a well centered (at 0) gaussian with sigma $\sim 40\mu$m. The bottom plot presents a profile of the x position under the z direction movement of the beam. Measurements using two different barrels are shown. The triangles (circles) correspond to the measurement from barrel 0 (1). Straight line fits for the two barrels, one dashed and one dotted are aligned close to each other. This shows a good barrel-barrel alignment.

The beam is stable up to 4 micron during a run. It moves, on average, 5 microns in the x direction and 11 micron in the y direction from run to run.

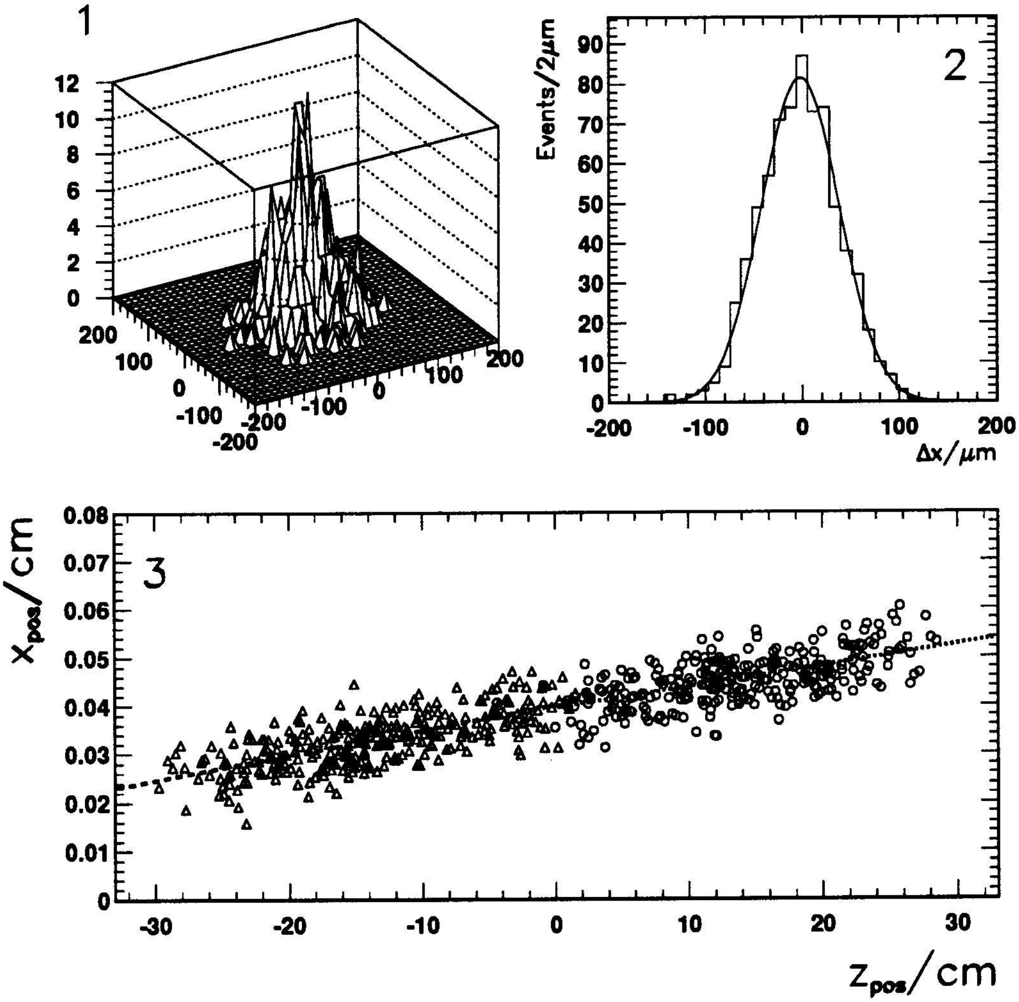

Figure 3.6: 1) Beam profile in $x - y$ 2-dimension (unit of μm. 2) An x-axis projection and a gaussian fit. 3) A z-distribution of the primary vertex.

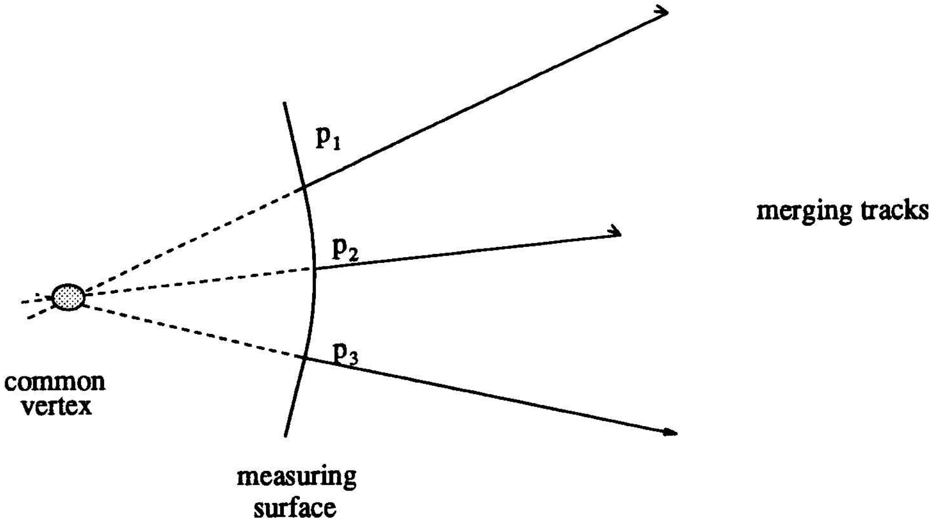

Figure 3.7: An illustration of the common vertex fitting.

3.4 Common Vertex Fitting

In the case when there are several tracks originating from a common space point which can either be a primary interaction point or a secondary decay vertex, a vertex constraint technique is often widely used to improve the resolution of existing track fits[20]. The χ^2 can also differentiate those tracks which are not associated with the same vertex.

The idea was first introduced in bubble chamber experiments. Consider a track parameter fit $\tilde{\mathbf{p}}_i$ of n merging tracks as a set of 5 n virtual measurements (see Figure 3.7). Each track is constrained through the common vertex point $\mathbf{v_s}$ and can be parameterized by its 3 coordinates (x_s, y_s, z_s) and 3 parameters of the generalized momentum vector $\mathbf{q}_i$. For instance, a helical track of $\mathbf{p} = (C, \phi_0, \cot\theta, d_0, z_0)^t$ can be expressed using only the parameters $\mathbf{q} = (C, \phi_0, \cot\theta)^t$ and the vertex coordinates

$\mathbf{v_s} = (x_s, y_s, z_s)^t$ as

$$\begin{cases} d_0 &= y_s \cos\phi_0 - x_s \sin\phi_0 - \frac{1}{c}\sin^2 cs \\ z_0 &= z_s - \lambda s \end{cases} \tag{3.11}$$

Here $\lambda = \cot\theta$, $\phi = 2cs + \phi_0$, $r = 1/2c$, and s is the projected length along the track which can be found by:

$$s = \frac{1}{2c}\sin^{-1}[2c(x_s\cos\phi_0 + y_s\sin\phi_0)] \tag{3.12}$$

A linear expansion can be used as an approximation to the function $\mathbf{p_i}(\alpha_i)$ near the point $\alpha_\mathrm{i}{}^0$, where $\alpha_\mathrm{i} = (\mathbf{v_s}, \mathbf{q_i})^t$. In general,

$$\mathbf{p_i} = \mathbf{p_i}(\alpha_\mathrm{i}{}^0) + \mathbf{T_i}\cdot(\alpha_\mathrm{i} - \alpha_\mathrm{i}{}^0) \tag{3.13}$$

where

$$\mathbf{T_i} = \frac{\partial \mathbf{p_i}}{\partial \alpha_\mathrm{i}}\Big|_{\alpha_\mathrm{i}{}^0} \tag{3.14}$$

If this is being done by an iterative procedure, the expansion point is just the previous estimate of the parameters. No matter how far the final answer is from the initial point, the linear model at each step is still valid.

The least-squares ansatz for the vertex fitting can be defined as:

$$\chi^2 = \sum_{i=1}^{N}(\mathbf{p_i} - \tilde{\mathbf{p}}_\mathbf{i})^t G_i^{-1}(\mathbf{p_i} - \tilde{\mathbf{p}}_\mathbf{i}) \tag{3.15}$$

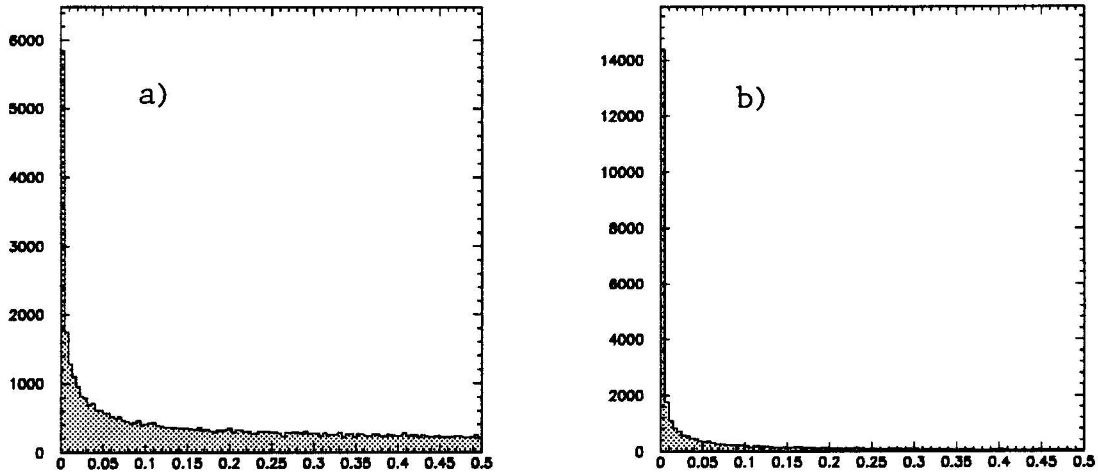

Figure 3.8: Inclusive electron sample:(a) A χ^2 probability distribution (*dof* assumed 1) from the vertex constrained fit of two SVX tracks. (b) A χ^2 probability distribution (*dof* assumed 3) from the vertex constrained fit of three SVX tracks.

where G_i is the 5×5 error matrix of track i. Minimizing the χ^2 yields a linear equation:

$$\sum_{i=1}^{n}(\mathbf{T_i}^t G_i^{-1}\mathbf{T_i})\alpha_i + (\mathbf{T_i}^t G_i^{-1})\delta\mathbf{p_i} = 0 \tag{3.16}$$

It is straight forward to solve the equation. The resulting 3(n+1) parameters can be improved through each step.

One important quantity is the χ^2 as defined earlier. It should have $5n - 3(n+1) = 2n-3$ degrees of freedom. Figure 3.8(a) and 3.8(b) show the probability distributions of the χ^2 from the vertex fitting of two tracks and three tracks respectively. The degrees of freedom are assumed to be 1 and 3 accordingly.

3.5 Monte Carlo Sample

The simulation is another important tool. Here we briefly describe the Monte Carlo sample of B_s semileptonically decays which will be used later in this analysis.

We use a toy generator which generates single bottom quarks with a flat pseudorapidity distribution inside $|\eta(b)| < 1.1$ and with the p_T spectrum from the Neason-Dawson-Ellis calculation (see Figure 3.9). We are interested in the b which will be sensitive to our lepton trigger threshold (mainly 9 GeV). This corresponds to the b quark p_T threshold of 15 GeV/c. In this simple generator, the process of fragmentation is not implemented. However we generate the B_s mesons from the b quarks according to the heavy quark fragmentation model created by Peterson et.[21]

$$f(z) \sim \frac{1}{z[1 - 1/z - \epsilon_Q/(1-z)]^2}, \tag{3.17}$$

where

$$z = \frac{E_Q + p_{Q||}}{E_q + p_{q||}}. \tag{3.18}$$

E_Q and E_q represent the energy of meson and quark respectively. $p_{Q||}$ and $p_{q||}$ are their momentum parallel to the quark direction. The parameter $\epsilon_b = \langle m_q^2 + p_{qT}^2 \rangle / \langle m_Q^2 + p_{QT}^2 \rangle$ is set to 0.006 ± 0.002 which was determined from experimental data[22].

We use the decay table from the CLEO Monte Carlo to force the B_s decay semileptonically. Only events with the $\ell^+ D_s^-$ states are accepted. We also force the D_s^- to decay exclusively to $\phi\pi^-$ and $\phi \rightarrow K^+K^-$.

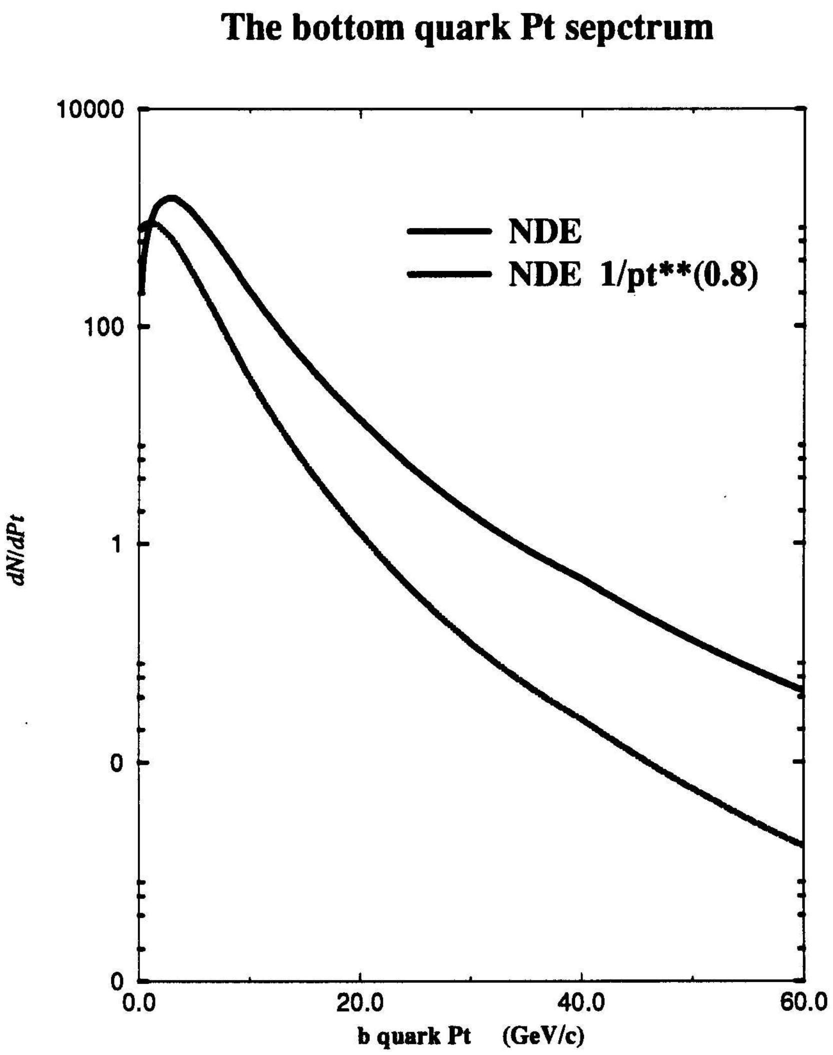

Figure 3.9: The p_T distributions of the bottom quark from NDE calculation. Also shown is a modified NDE spectrum by using the weight factor $p_T^{(-0.8)}$.

Finally, we carry all generated events through the full CDF detector simulation with the model named CDFSIM. The B_s and D_s meson decay vertices are created according to their lifetimes. The simulated data are processed with the same offline production models which have been used for the real data. We also keep the information about all the particles' four vectors and decay vertices for reference.

Chapter 4

Identification of Leptons

When two high energy hadrons collide, most of the time it produces only jets of gluons and light quarks. Heavy quark production (t, b or c) accounts for only a small fraction of the total. At Tevatron energies, for example, we expect the $b\bar{b}$ production cross section to be a thousand times smaller than the total $p\bar{p}$ cross section. To select bottom quark events, we look for leptons as a signature of the semileptonic decays. Because both gluon and light quarks do not contribute to the source of leptons, those backgrounds can be filtered out by requiring a high p_T lepton.

4.1 Lepton Triggers

At CDF, a multi-level trigger system which includes Level 1, Level 2 and Level 3, is being used for simultaneously selecting collisions from multiple channels of interesting physics. The events for this analysis have been collected using inclusive electron and muon triggers.

4.1.1 Electron

The Level 1 electron trigger is based on the total energy of any single calorimeter tower $(\Delta\eta = 0.2) \times (\Delta\phi = 15^\circ)$. An event is required to have an electromagnetic energy $E_T > 6$ GeV to pass the main electron trigger. Another 4 GeV threshold is also used for a prescaled trigger, i.e, the trigger rate is forced down by a selected prescale factor. Here the prescale factor 20 is used which means that only 5% of the events passed the threshold are accepted by this trigger.

At Level 2, electromagnetic clusters are constructed as sets of contiguous trigger towers each with $E_T > 7$ GeV (4 GeV), including at least one "seed" tower with $E_T > 9$ GeV (5 GeV) for the main (prescaled) trigger. Longitudinal information is also used at Level 2. The ratio of hadronic to electromagnetic energy in the cluster (HAD/EM) is required to be less than 0.125. A hardware fast track processor (CFT) finds a list of $r - \phi$ tracks at 5 different P_T thresholds. We require at least one track with transverse momentum of $p_T > 9.2$ GeV/c (6 GeV/c) to be associated with the cluster in the main (prescaled) trigger.

The CDF Level 3 trigger uses multi CPU processors and software reconstruction algorithms to make decisions 'online'. The algorithms used in this 'online' system are identical to those used in 'offline' reconstruction. We will describe them in the section on lepton selection.

4.1.2 Muon

The Level 1 central muon trigger requires a pair of hits on radially aligned wires in the CMU chambers. The transverse momentum, p_T, of the muon track segment is measured by using the arrival times of the drift electrons at the sense wires to determine the deflection angle due to the magnetic field. The muon trigger requires a muon track segment found in the CMU with $p_T > 6$ GeV/c in coincidence with a muon track segment in the CMP with $p_T > 3.3$ GeV/c.

The Level 2 main (prescaled) trigger requires a 5 degree match in the $r - \phi$ plane between a CFT track with $p_T > 9.2(6.0)$ GeV/c and a segment in the muon chambers which fires the Level 1 trigger.

4.2 Electron Selection

Electron candidates are selected by requiring an electromagnetic energy cluster associated with a CTC track in the central region. The energy cluster is required to have the shower profiles consistent with that expected from a real electron, both longitudinal and lateral. The track must match the cluster geometric position. The momentum of the track measured by the tracking chamber must also match the energy of the cluster measured by the calorimeter. Figure 4.1 illustrates an electron going through the central CDF detector.

The electron clustering algorithm starts with "seed" towers with E_T threshold

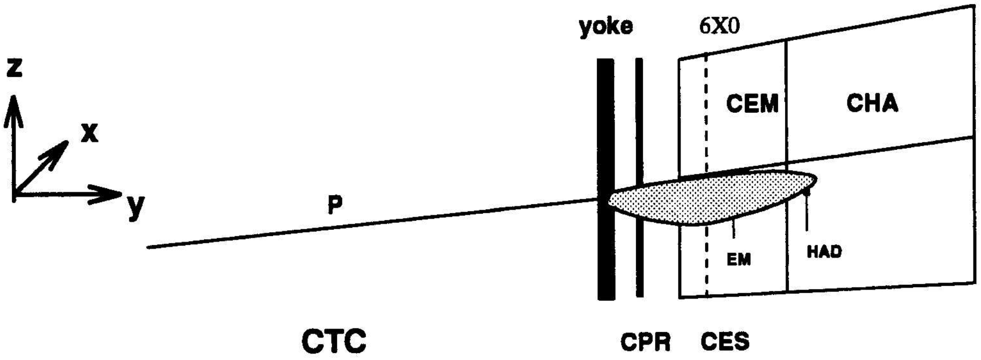

Figure 4.1: A diagram of the electron identification in the CDF central detector.

of 3 GeV. Adjacent towers with $E_T > 0.1$ GeV are added. An electron shower is generally contained within one or two towers. Because the border between towers in the azimuthal direction contains roughly 1 cm of inactive material, and because high p_T electron showers are typically smaller than this distance, the electron shower rarely spread across the ϕ boundary between wedges. The CEM clusters are restricted to three or fewer towers in the z direction and a single ϕ wedge. At level 3 the main (prescaled) E_T threshold of the cluster is 9 GeV (6 GeV). In the offline reconstruction a cut at 6 GeV is made.

The lateral shower profile across the towers can be described using a variable LSHR2 defined as:

$$\text{LSHR2} = 0.14 \sum_{k=2} \frac{M_k - P_k}{\sqrt{0.14^2 E + (\Delta P_k)^2}} \tag{4.1}$$

where the sum is over 2 towers in the cluster adjacent to the seed tower. M_k is the measured energy in the adjacent tower and P_k is the expected energy in the adjacent tower. E is the electromagnetic energy in the cluster, and ΔP_k is an estimate of the error in P_k. The expected energy P_k is predicted using the event vertex, the center of the shower as measured in the strip chamber and a shower profile parameterization obtained from test beam measurements. The uncertainty in this quantity, ΔP_k is taken to be the variation in P_k arising from a 1 cm shift in the center of the shower. The factor 0.14 represents a statistical fluctuation. We require that LSHR2$<$ 0.2 both at Level 3 and in the offline selection.

In an EM calorimeter tower, lateral shower profiles are measured by fine segmented strips and wires of the CES in both ϕ and z directions. The profiles are fit to the test beam electron data. The χ_z^2 and χ_ϕ^2 obtained from the fits are used to test for an electron candidate. At Level 3 we require the matching to have $\chi_z^2 < 10$ and $\chi_\phi^2 < 15$. In the offline electron selection, cuts $\chi_z^2 < 10$ and $\chi_\phi^2 < 10$ are used.

A significant amount of the background in the electron sample comes from overlaps, where a charged pion track overlaps with an EM cluster of a photon from a π^0 decay. Requiring a track pointing at the cluster which matches both the position and the energy of that cluster can reduce this background. To be specific, CTC tracks are extrapolated to the radius of the strip chambers and the extrapolated positions are compared with the shower position measured by the strip clusters. The positions must agree in both the z and xy directions. Cuts $\Delta z < 5$ cm and $\Delta x < 3.0$ cm have been used at Level 3. Tighter requirements $\Delta z < 3$ cm and $\Delta x < 1.5$ cm are used for the offline selection. The energy measured by the calorimeter should match the momentum measured by the tracking chamber for an electron. At Level 3 the requirement for the trigger is $p_T > 6$ GeV/c (4 GeV/c prescaled). A matching cut $0.75 < E_T/P_T < 1.5$ in used in the offline electron selection.

The only longitudinal shower information available comes from the comparison of the energy deposited in the front EM calorimeter and in the rear hadron calorimeter. An isolated electron (eg. from W decay) would have only small energy leakage to the hadron compartment. A tight cut of HAD/EM < 0.04 would be quite efficient for those electrons. However electrons from B decays are generally not so isolated, especially high p_T ones. For the semileptonic decay $b \rightarrow \ell^+ \nu c$, hadrons from subsequent charm decays are usually near by. To be efficient, a cut of HAD/EM < 0.1 is used in general and a tight cut HAD/EM < 0.04 is made only when there is only one 3-D track pointing to the electron tower. The electron identification cuts are summarize in Table 4.1.

4.2.1 Photon Conversion Electrons

Leptons from W,Z decays and Drell-Yang production are not treated in this analysis, because the quantities are small. The major sources of electrons other than heavy quark decays are Dalitz decays of π^0 and photon conversion which produce an electron and position pair. Some of the 'conversion' electrons can be identified by finding an accompanied partner track in the CTC. The two tracks can be extrapolated to a

Table 4.1: A list of the electron selection cuts

Identification Variables	Offline Cut
E_T	> 6.0 GeV
E_T/P_T	[0.75,1.5]
LSHR2	< 0.2
χ^2_z	< 10
χ^2_ϕ	< 10
$\|\Delta z\|$	< 3.0 cm
$\|\Delta x\|$	< 1.5 cm
Had/EM	< 0.1

common point where they are parallel and satisfy the following requirements:

$$| S |< 0.2 \text{ cm}$$

$$| \Delta \cot\theta |< 0.06$$

Here S is the separation of two tracks in $r - \phi$ plane at the point where they are tangent. The identified conversion electrons are removed from the electron sample.

4.2.2 Residual Fake Hadrons

A small fraction of charged pions happen to shower early in the calorimeter and deposit most of their energy in the EM component. These pions behave just like

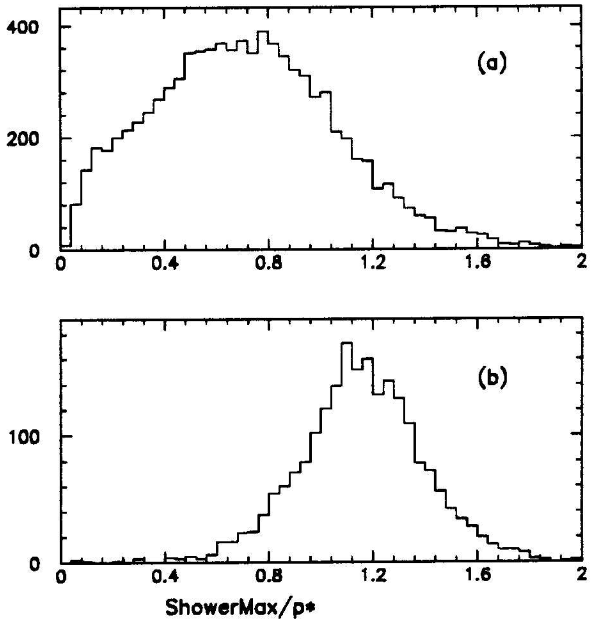

Figure 4.2: ShowMax/p^* (a) 0.04 <Had/EM< 0.1 region (b)W electrons.

electrons and since they pass all the selection cuts for electrons they remain as residual backgrounds. These fake hadrons do not have the same charge correlation with charm mesons as the leptons from B do. So for this analysis they are not important. However, since most of these hadrons have the same kinematic properties as the selected electrons and no long lived b or c quarks are involved, they can be used as a control sample to study the effect of decay length resolution (see Chapter 10).

Although it is not easy to identify the fake hadrons with calorimeter information, they can be separated by using information from the strip chamber pulse size and from the preshower radiator measurement.

Electrons and pions have quite different longitudinal shower profiles in the electromagnetic calorimeter. An electron shower has a maximum shower point at about 5.9 X_0 radiation lengths while a pion has a quite flat shower profile. So the two sources can be distinguished by looking at the shower energy collected by the strip chamber at this maximum point. A properly normalized CES pulse size can be defined as:

$$\text{ShowerMax}/p^* = G \cdot E_{wire}(7) \cot\theta / F(p) \tag{4.2}$$

where the $E_{wire}(7)$ is a CES wire cluster energy summed over 7 channels. G is the gas gain correction factor and $F(p)$ is determined from calibration to be $F(p) = 10.0 * (P/10.0)^{(.85+.15\exp(-P/15.0)-0.1P/100.0)}$. Figure 4.2 shows the distributions of the 'ShowerMax/p^*' for a sample of 'electrons' with HAD/EM > 0.04 and a sample of W electrons. Events from the region of $0.04 <$ HAD/EM< 1.0 are dominated by the fake hadrons, and therefore they have generally low pulse size (ShowerMax/p^* most below 1). In contrast, W electrons have quite large ShowerMax/p^*. A fake hadron background sample can be selected by requiring the ShowerMax/$p^* < 0.4$. On the other hand an electron rich sample can come from the ShowerMax/$p^* > 1$ cut.

The PreShower pulse can also be used to distinguish electrons from the fake hadrons. The following definition of 'PreShower/p^*' is used.

$$\text{PreShower}/p^* = G \cdot E_{clust}(3) \sin\theta / (P_e/10.0)^{0.3} \cdot 0.001 \tag{4.3}$$

where $E_{clust}(3)$ is a cluster energy summed over 3 channels. The energy dependency of the pulse is removed by this definition. Two distributions of the 'PreShower/p^*' are

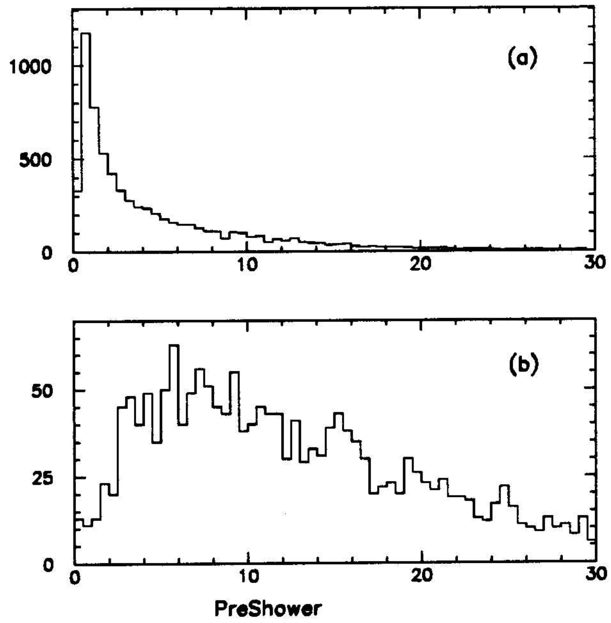

Figure 4.3: PreShower/p^*: (a)0.04 <Had/EM< 0.1 region (b)W electrons.

shown in Figure 4.3 for the HAD/EM > 0.04 sample and the W electron sample. The fakes have very low response and they peak below 2.0. The W electrons have quite larger response from the CPR and the distribution is also much broader. The fakes and electrons can thus be separated by the PreShower/$p^* < 3$ and PreShower/$p^* > 8$ cuts respectively.

4.3 Muon Selection

Muons do not interact strongly with matters. They lose energy in materials primarily through uniform ionization and they are called minimum ionization particles (MIP) therefore. Since the rate of energy loss for muons is much lower than that for hadrons,

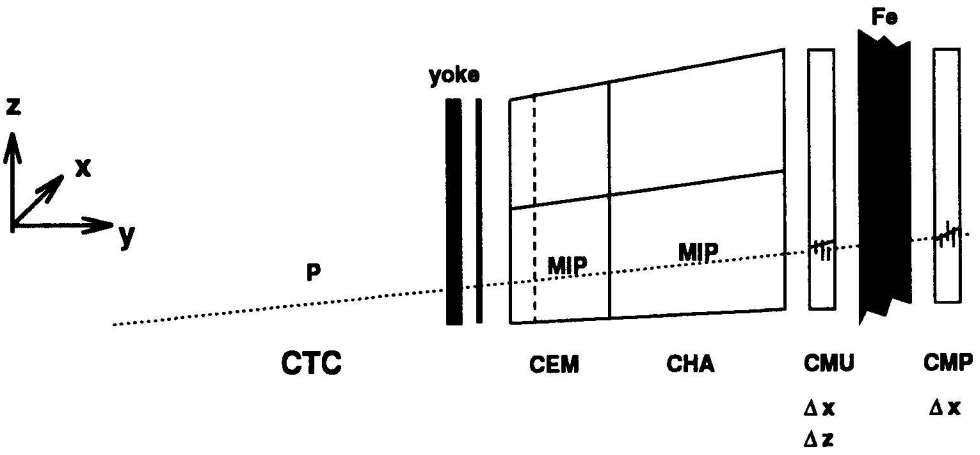

Figure 4.4: A diagram of the muon identification in the CDF central detector

.

they can be distinguished by their ability to penetrate materials. As shown in Figure 4.4 all the central muon chambers (CMU) are built behind the calorimeters which plus the magnet yoke have a total of 6 interaction lengths. These amount of materials generally can contain about 95% of the hadron shower at incident energy of 20 GeV. The depth of the materials normally increases logarithmically with the incident energy. To reduce the rate of hadron punch through, another 3.5 interaction lengths of steel is added and a new set of chambers called CMP are installed behind that steel. With the help of CMP confirmation, hadronic punch-through backgrounds to the muon signal can be reduced considerably as shown in Figure 4.5. In this analysis, the muons are identified by matching a CTC track to muon track segments found in both the CMU and CMP chambers. The Level 3 trigger requires a reconstructed track of $p_T > 7.5$ GeV/c or $p_T > 6$ GeV/c and a fired Level 2 prescaled trigger. This

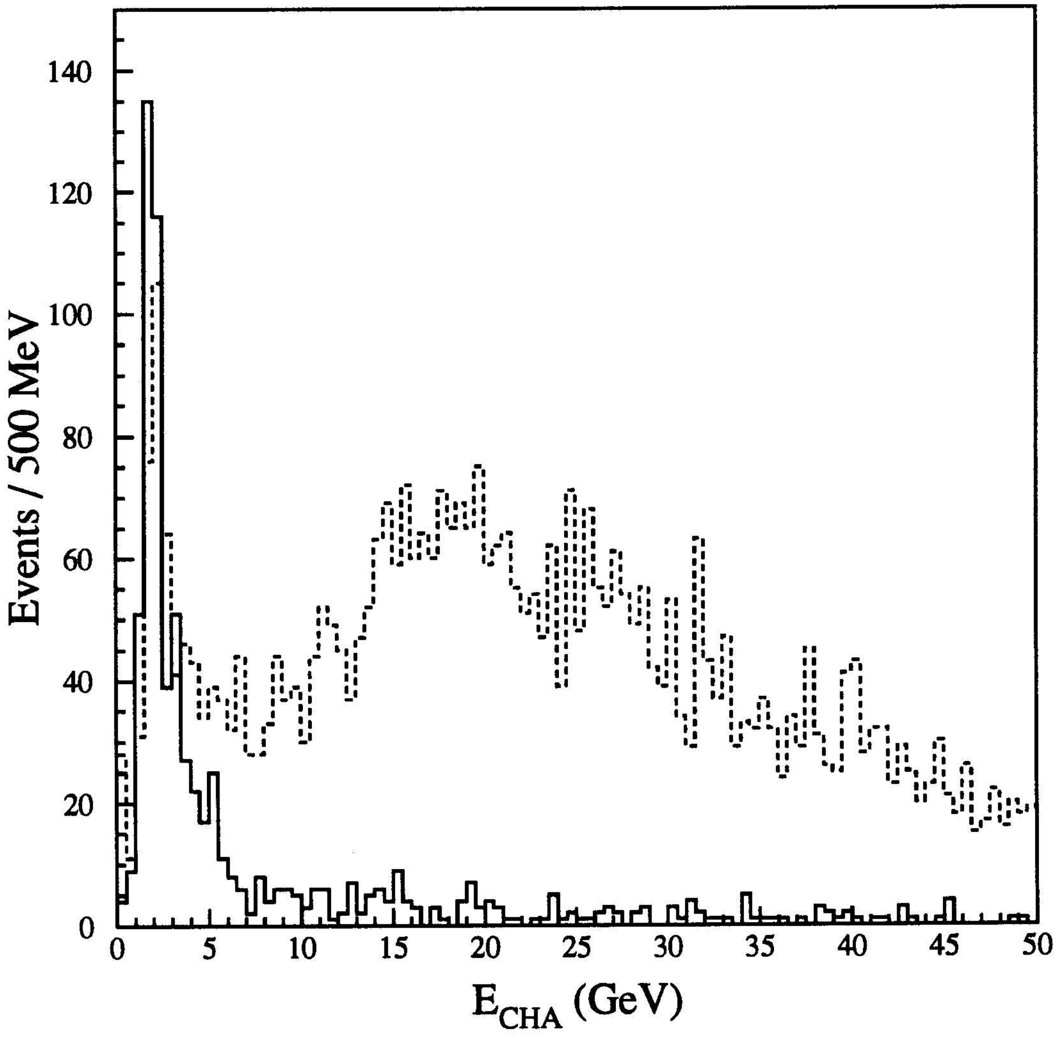

Figure 4.5: Hadronic Energy deposited in the muon tower: dashed histogram is for tracks with a stub in the Central Muon system (CMU), and the open histogram is that for tracks that have a stub in the Central Muon Upgrade (CMP).

track is extrapolated to the radius of the CMU chamber and must match within 10 cm of a segment in the muon chamber. In the offline, a reconstructed track of $p_T > 6$ GeV/c is matched to the muon segments. The χ^2 of the distance matching (both x and z directions) at the CMU and (only the z direction) at the CMP are calculated. The standard deviations due to the effect of Coulomb scattering from the materials of CEM, CHA and magnet yoke *etc.* are all included. The selection cuts are

- $\chi^2_{\Delta x} < 9$ (both CMU and CMP) for the distance matching in x.
- $\chi^2_{\Delta z} < 12$ (CMU only) for the distance matching in z.

Chapter 5

Charm Meson Reconstruction

When a bottom hadron decays semileptonically, it produces a charmed hadron and a lepton which are charge correlated. We expect a 'right' sign correlation $\ell^-(c\overline{q})$ (or $\ell^+(\overline{c}q)$) which corresponds to the decay of b (or $\overline{b}$) as opposed to a 'wrong' sign correlation $\ell^+(c\overline{q})$.

In this chapter we discuss the topic of charm meson reconstruction. In particular, we are interested in the meson D_s^- which is the product of B_s semileptonic decay. We will first take a look at the D^0 and the D^{*+} reconstruction.

5.1 D^0 and D^{*+} reconstruction

Both D^0 and D^{*+} are the products of $\overline{B}^0$ and B^- semileptonic decays. Table 5.1 lists the exclusive channels and the branching ratios of $\overline{B}^0$ and B^- semileptonic decays which produce either a D^0 or a D^{*+}[23].

38% of the B semileptonic decays produce the D^{*+} and 70% lead to D^0.

Table 5.1: A list of the semileptonic decay modes for the $\overline{B}^0$ and B^-

					Branching Ratio
$\overline{B}^0$	$\rightarrow$	D^+	ℓ^-	$\overline{\nu}_l$	$1.6 \pm 0.4 \pm 0.6$ %
$\overline{B}^0$	$\rightarrow$	D^{*+}	ℓ^-	$\overline{\nu}_l$	$4.5 \pm 0.4 \pm 0.2$ %
		$\hookrightarrow$	D^0	π^+	55 ± 4 %
B^-	$\rightarrow$	D^0	ℓ^-	$\overline{\nu}_l$	$1.5 \pm 0.4 \pm 0.2$ %
B^-	$\rightarrow$	D^{*0}	ℓ^-	$\overline{\nu}_l$	$4.3 \pm 0.5 \pm 0.7$ %
		$\hookrightarrow$	D^0	$\pi^0(\gamma)$	100 %

5.1.1 $D^0 \rightarrow K^-\pi^+$

This decay channel has a branching ratio of 3.65%. Kaons and pions are not distinguished in the CDF detector. However, the kaon from a D^0 should have the same charge sign as the lepton in the decay sequence $b \rightarrow c \rightarrow s$. We form all possible $K^-\pi^+$ combinations with tracks found inside a cone of radius of 0.7 around the lepton candidate. The cone size is designed to contain most (> 90 %) of the B decay products. The kaon mass is assigned to the track with the same charge sign as the lepton (the 'right sign' combination), and the pion mass is assigned to the one with the opposite sign charge. The K^- and π^+ candidates are required to pass the transverse momentum requirements:

- $P_T(K^-) > 1.5$ GeV/c
- $P_T(\pi^+) > 0.8$ GeV/c

to maximize the signal to noise ratio. Only those events which have both $b \rightarrow c\ell^-\overline{\nu}$ and subsequent $c \rightarrow s$ decay vertices well measured inside the SVX will be useful. Therefore at least two daughters from the charm decay and the lepton from the B decay are required to be the SVX tracks with some minimum quality requirements. The quality cuts include both CTC and SVX. We require

for the CTC

- At least 2 axial superlayers with 4 or more hit wires each,
- At least 2 stereo superlayers with 2 or more hit wires each.

For the SVX

- Number of SVX hits ≥ 2
- $\chi^2_{SVX}/dof < 6$.

We use the technique of common vertex constraining described in Chapter 3 to achieve good resolutions on both the mass and the decay vertex position. In the case of $D^0 \rightarrow K^-\pi^+$, both the K^- and the π^+ tracks must come from a common vertex point in 3-D . This constraint is a fit with one degree of freedom and it improves the mass resolution. The χ^2 probability of this fit is required to be larger than 1%.

Bottom decay events are expected to have a large displaced vertex in the boost direction. Since a neutrino is missing from the semileptonic decay, the $\hat{P}_T(\ell^- D^0)$ must be used as an approximation of the B direction. The vertex of the $K-\pi$ is required to be 1 σ away from the production point along that direction. Since backgrounds from random combinations give only fake vertices, they are usually near the primary vertices and have no bias toward any preferred direction. The cut

- $L_{xy} > \sigma_{L_{xy}}$

reduces these backgrounds significantly. The formula for L_{xy} can be found in chapter 6. Briefly, it is the transverse projection of the displacement of the $K-\pi$ vertex (with respect to the beam position) along $\hat{P}_T(\ell D)$. σ_{Lxy} is the measurement error of this quantity.

Since a bottom quark has a fairly hard fragmentation function, we also introduce an isolation cut to improve the signal to noise ratio. Any 'excess' energy inside a small cone with $R = 0.4$ around the high p_T lepton comes from the B fragments. We compute a quantity called E_T^{iso} by summing all the transverse tower energy inside this cone. If the lepton is an electron, the tower of the electron is excluded from this summation. For muons, the minimum ionizing energy is subtracted from the total. Most of this 'excess' energy is expected to be carried by the charm meson D^0, and we required that

- $E_T^{iso}/P_T(K^-\pi^+) < 1.2$

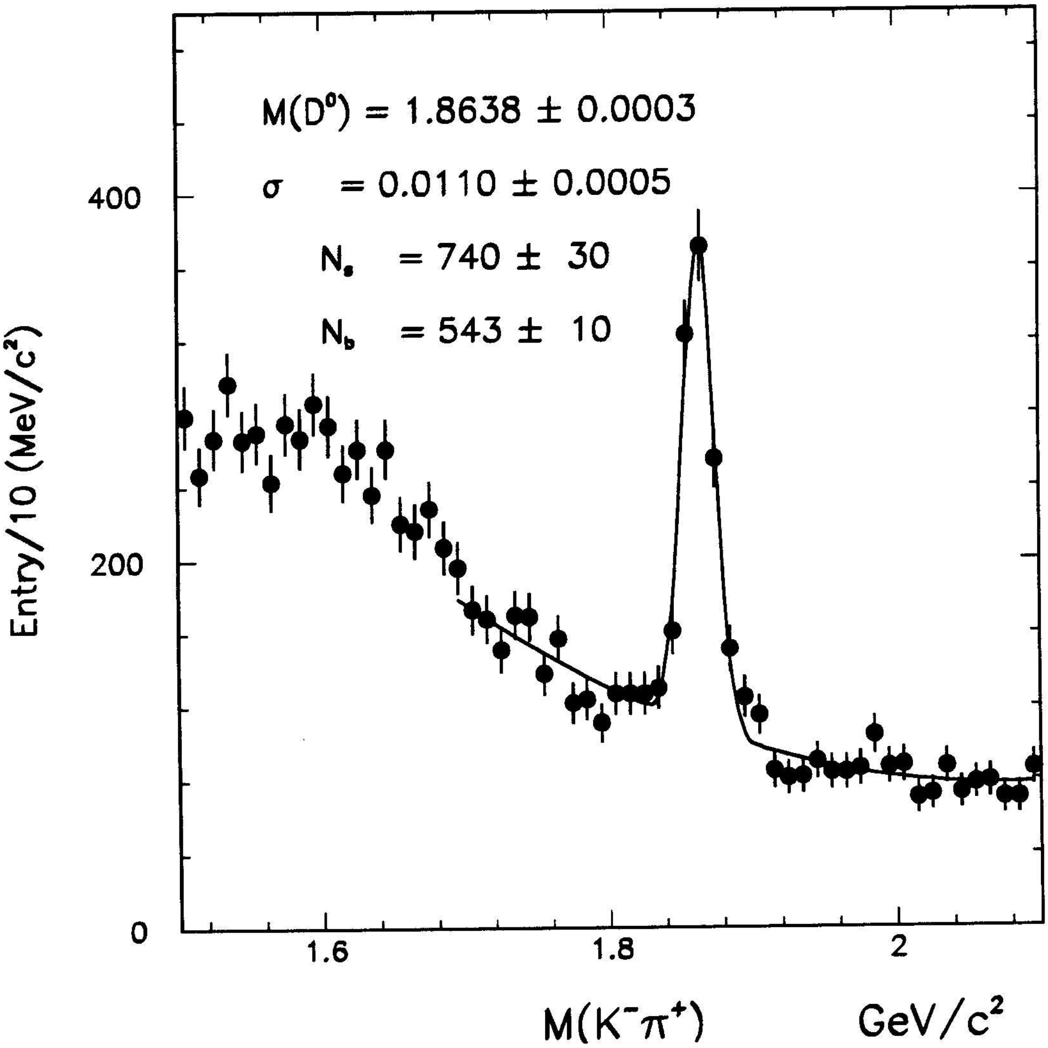

Figure 5.1: Mass spectrum of right sign $K^-\pi^+$ combinations from both electron and muon data. The D^0 peak and its background are fit with a Gaussian function and a 2nd order polynomial function.

A plot of right sign $K^-\pi^+$ mass combinations from the combined electron and muon data is shown in Figure 5.1. The spectrum above the region of $M(D^0) - m(\pi)$ is fitted with a gaussian function plus a second order polynomial function using a binned log-likelihood method. The resulting mean and width of the D^0 are

$$\begin{aligned} M(D^0) &= 1.864 \pm 0.0003 \text{ GeV}/c^2 \\ \sigma(D^0) &= 11.1 \pm 0.5 \text{ MeV}/c^2 \end{aligned}$$

There are 740 $\pm$ 30 D^0 signals in the region of $1.844 < M(K^-\pi^+) < 1.884$ GeV/c^2 where the backgrounds are estimated to be 543 $\pm$ 10.

5.1.2 $D^{*+} \rightarrow D^0\pi^+$, $D^0 \rightarrow K^-\pi^+$

Some of the D^0 signals above are from the D^{*+}, in which case there should be another soft π nearby. Since the Q value from the decay $D^{*+} \rightarrow D^0\pi^+$ is only $\sim$ 40 MeV, this π should be quite soft and very collimated along the D^0. Since this soft π may suffer huge multiple scattering, it is not used for vertexing, nor for the direction of the B. For this track, in order to increase the efficiency, the L_{xy} cut is changed to

- $L_{xy} > 0$

and the isolation cut to

- $E_T^{iso}/P_T(K^-\pi^+\pi^+) < 1.2$

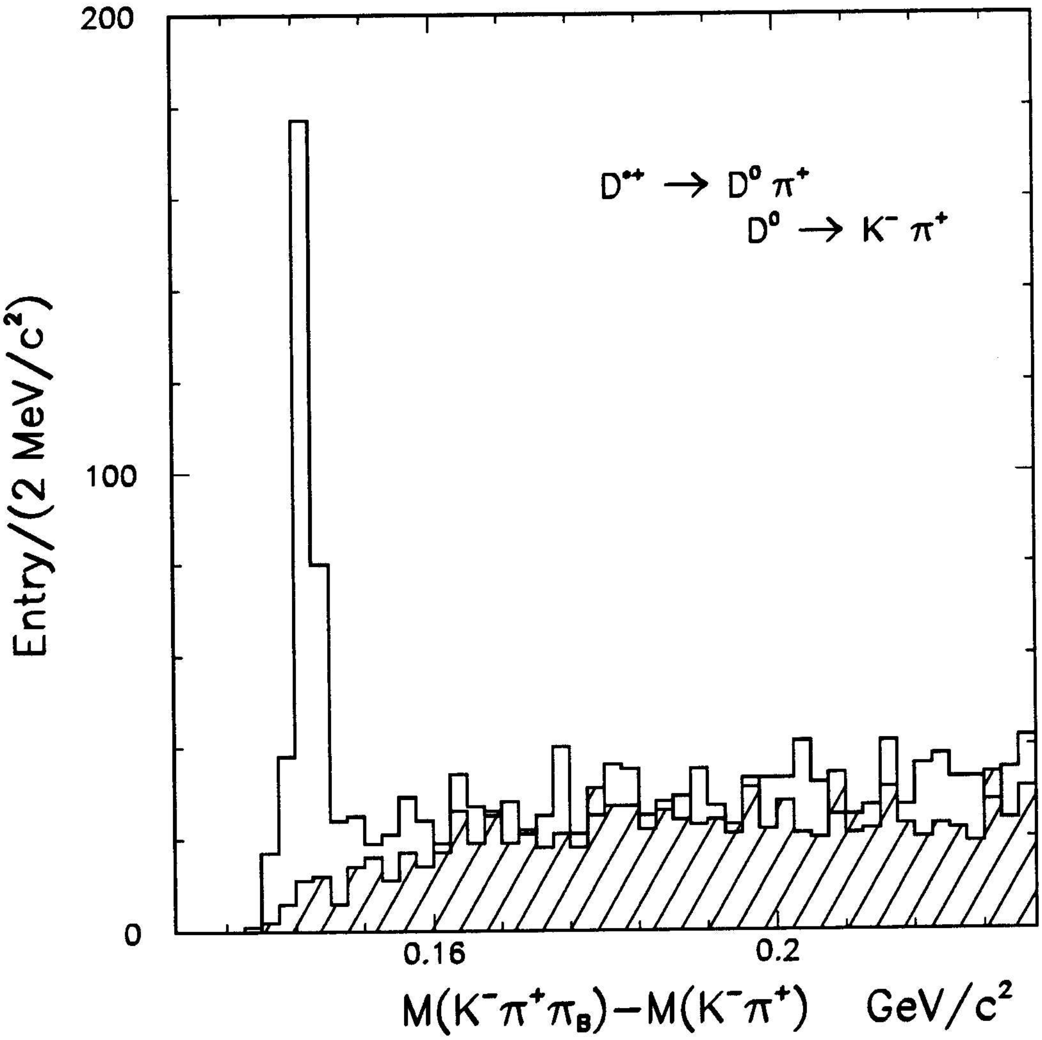

Figure 5.2: ΔM between $K^-\pi^+\pi_B^\pm$ and $K^-\pi^+$ combinations. The right sign ($K^-\pi^+\pi_B^+$) combinations are plotted as an open histogram and the wrong sign ($K^-\pi^+\pi^-$) are plotted as a hatched histogram. The D^{*+} signal is shown as a narrow peak in the right sign plot below $\Delta M = 156$ MeV/c^2.

D^0 candidates are selected from the mass region $|M(K^-\pi^+) - 1.864| < 0.025$ GeV/c^2. A D^{*+} object is formed by combining a $K^-\pi^+$ pair with another soft track found inside the same 0.7 cone. This pion is often called the 'bachelor' pion. A 'right' sign bachelor pion should have the opposite sign charge of the lepton thereby making a $K^-\pi^+\pi^+$ combination. We plot the mass difference between the $K^-\pi^+\pi$ and $K^-\pi^+$ in Figure 5.2 for both the right and wrong sign combinations. A narrow peak due to D^{*-} production is observed in the right sign plot as expected but not in the wrong sign one.

5.1.3 $D^{*+} \rightarrow D^0\pi^+$, $D^0 \rightarrow K^-\pi^+\pi^0$

This D^0 decay mode has a larger branching ratio than the $K^-\pi^+$ mode, and is dominated by the decay chain

$$D^0 \rightarrow K^-\rho^+, \ \rho^+ \rightarrow \pi^+\pi^0 \tag{5.1}$$

Because the ρ meson is polarized in this decay, the distribution of the $K^-\pi^+$ mass exhibits a characteristic peak just below the kinematic limit (satellite peaks) and at very low mass region (see the Monte Carlo plot in Figure 5.3). Because of the small Q value in the D^{*+} decay, the mass difference between $K^-\pi^+\pi_B^+$ and $K^-\pi^+$ for the high peak of $M(K^-\pi^+)$ is also kinematically limited to be near the π mass. So these decays can still be identified using the same technique as before, without worrying about the missing π^0. All $K^-\pi^+$ combinations with $M(K^-\pi^+) > 1.5$ GeV/c^2 are

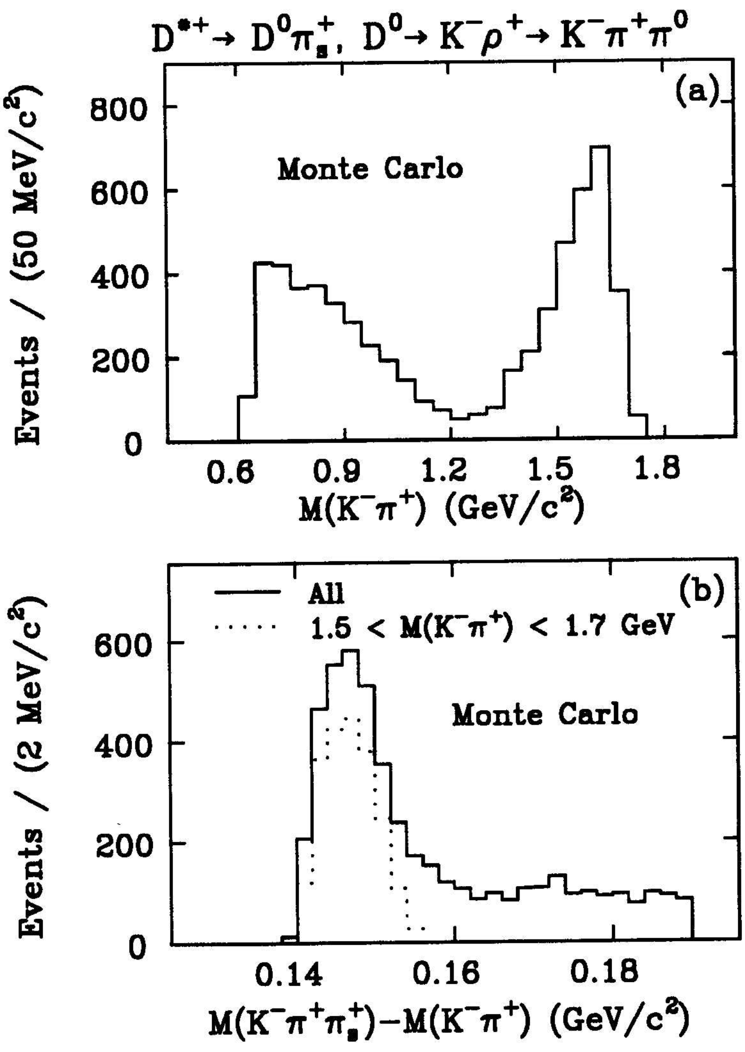

Figure 5.3: (top) Combined $K^-\pi^+$ mass from $D^0 \to K^-\rho^+$, $\rho^+ \to \pi^+\pi^0$, where D^0 from the D^{*+}. (bot) Mass difference between the $K^-\pi^+\pi_B^+$ and $K^-\pi^+$ from the events in the top plot. The dashed histogram represents those events which are $M(K^-\pi^+) > 1.5$ GeV/c^2.

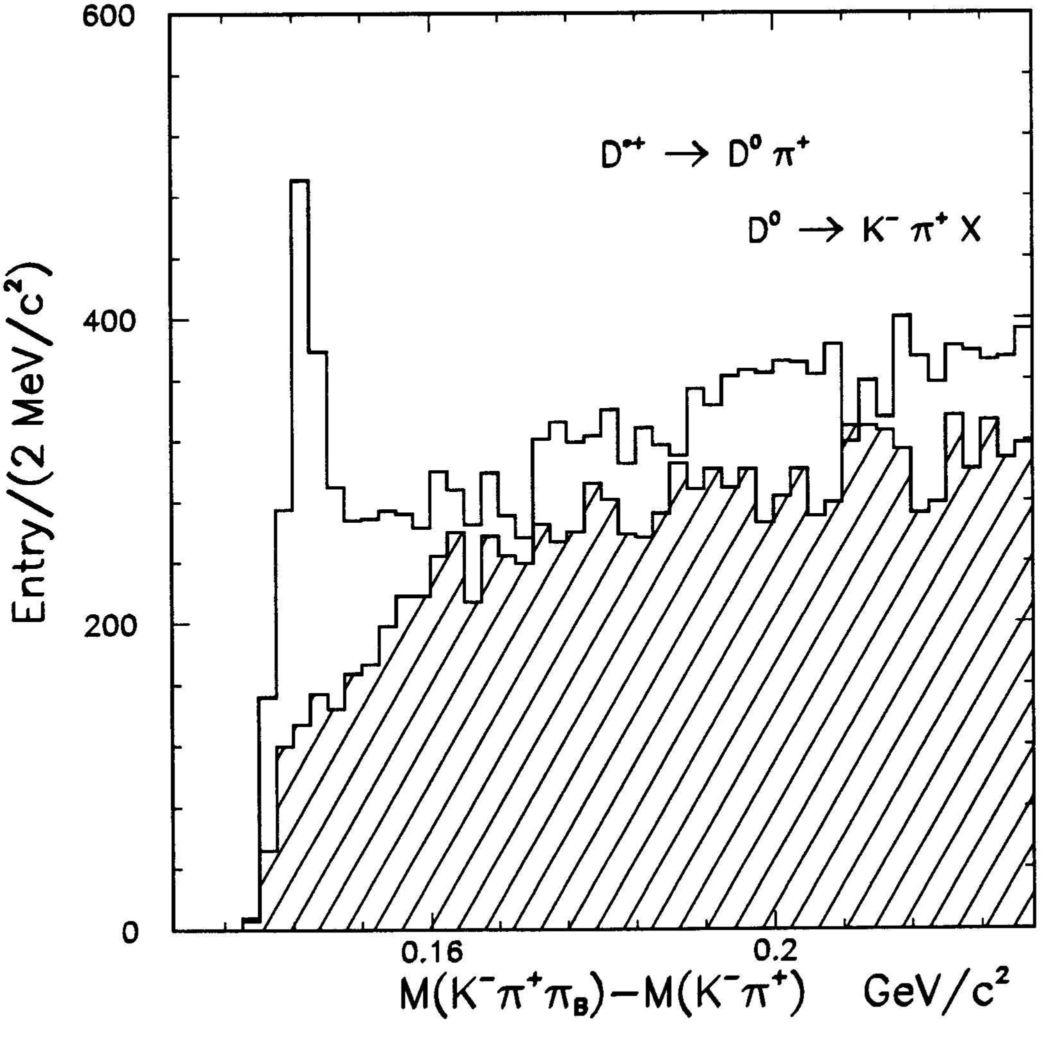

Figure 5.4: ΔM between $K^-\pi^+\pi_B^\pm$ and $K^-\pi^+$ combinations. The right sign $(K^-\pi^+\pi_B^+)$ combinations are plotted as an open histogram and the wrong sign $(K^-\pi^+\pi^-)$ are plotted as a hatched histogram. The D^{*+} signal is shown as a narrow peak in the right sign plot below $\Delta M = 156$ MeV$/c^2$.

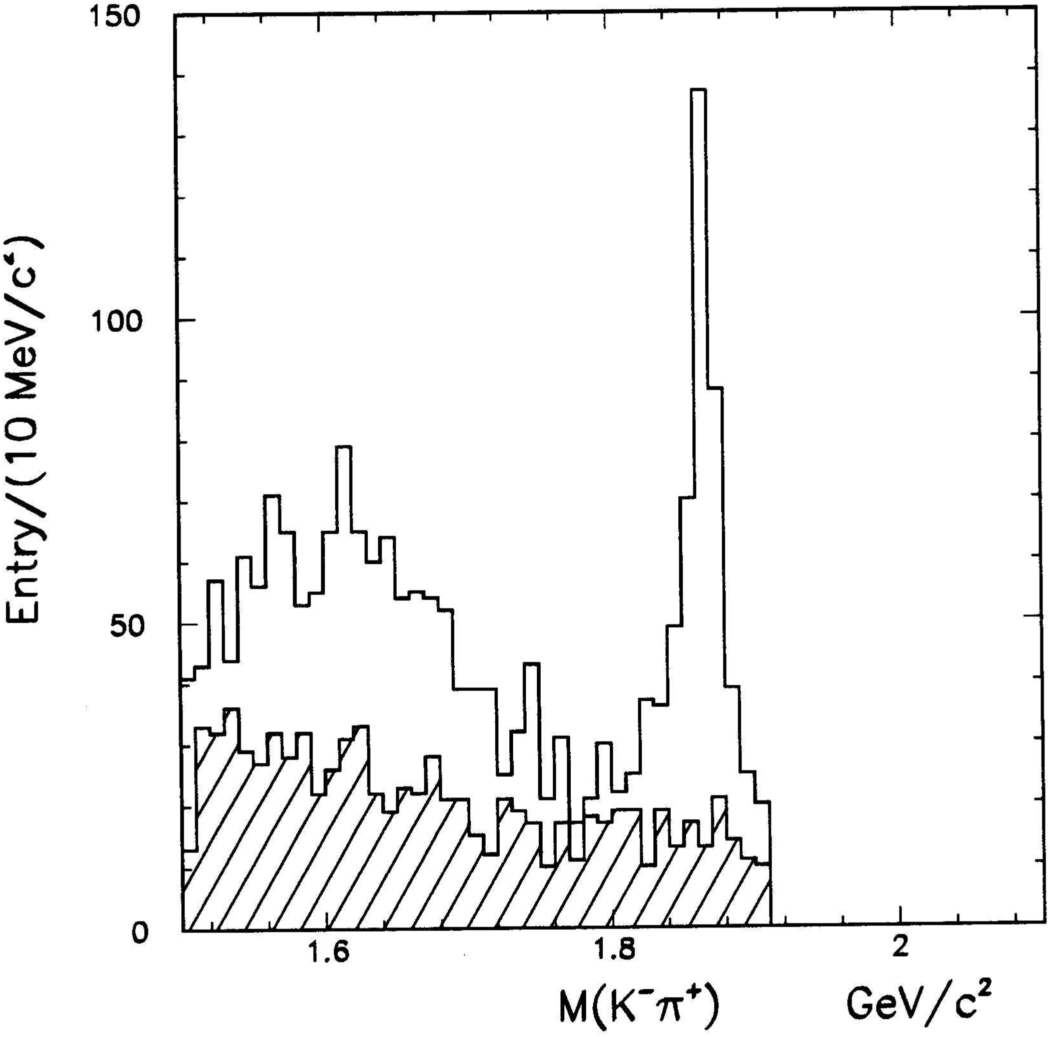

Figure 5.5: Spectrum of $M(K^-\pi^+)$ for both right sign (open hist) and wrong sign (hatched hist) combinations with $\Delta M = 156$ MeV$/c^2$.

used. Figure 5.4 shows the mass difference plot for both right sign and wrong sign situations. We see clearly a peak which is wider than the one in Figure 5.2 and only appears in the right sign case. D^{*+} signals are selected from the region

- $M(K^-\pi^+\pi_B^+) - M(K^-\pi^+) < 0.156$ GeV/c^2

Figure 5.5 shows the $M(K^-\pi^+)$ of those candidates for the right sign and wrong sign cases. In addition to the $D^0 \rightarrow K^-\pi^+$ peak, there is also a broad enhancement in the mass region of 1.5 -1.75 GeV/c^2 which is a satellite peak of the D^{*+}. Combining the two regions, there are a total of 640 D^{*-} candidates.

5.2 D_s reconstruction

Several decay modes of the D_s have been measured with quite large branching ratios[23]. Four of them are listed in the following Table 5.2 along with subsequent decays which are detectable in CDF. In this analysis, we choose only the easiest decay, namely $D_s^- \rightarrow \phi\pi^-$ because of the narrow ϕ width ($\Gamma \sim 5$ MeV). First we define a search cone of size of $\Delta R = 0.8$ around the lepton candidate. This cone covers about 90% of the region where the decay products from the B ($p_T(b) > 15$ GeV/c, the trigger sensitive region) are located. Any pair of oppositely charged tracks with $p_T > 1$ GeV/c within that cone are assigned kaon masses and combined to form a ϕ candidate. Because soft ϕ production comes primarily from heavy quark fragmentation, a p_T cut on the ϕ is made.

Table 5.2: Some exclusive modes of the D_s^- decays.

D_s^-	$\rightarrow$	ϕ	π^-	$2.8 \pm 0.5\%$
		↳	K^+K^-	$49.1 \pm 0.8\%$
D_s^-	$\rightarrow$	K^{*0}	K^-	$2.6 \pm 0.5\%$
		↳	$K^+\pi^-$	100%
D_s^-	$\rightarrow$	K^{*-}	K^0	$3.3 \pm 0.9\%$
		↳	$\overline{K}^0\pi^-$	2/3
D_s^-	$\rightarrow$	K^-	K^0	$2.8 \pm 0.7\%$

- $P_T(K^+K^-) > 2.0$ GeV/c.

A typical K^+K^- mass spectrum from an electron data sample is shown in Figure 5.6 where the ϕ signal is visible after requiring that the K^+K^- vertex be displaced from the origin. ϕ candidates are defined to be the K^+K^- pairs which satisfy

- $|M(K^+K^-) - 1.019| < 8$ MeV/c^2.

A Monte Carlo plot of the $\phi \rightarrow K^+K^-$ mass spectrum is shown in Figure 5.7, where the detector simulation package CDFSIM has been used. The signal is fit with a Breit-Wigner function and determined that the FWHM is determined to be 4.9 ± 0.4 MeV/c^2. This includes the ϕ natural width as well as the detector resolution. Therefore the mass window defined for ϕ candidates covers about 90% of the signal.

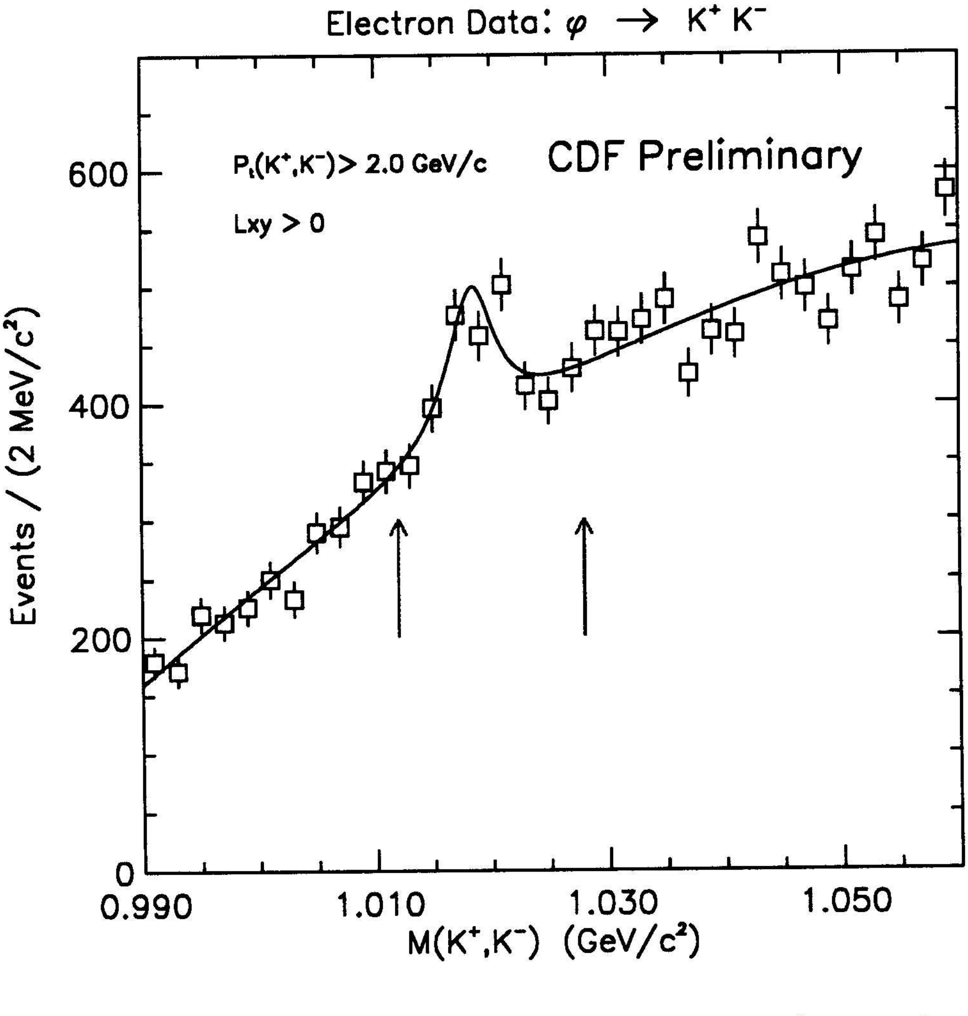

Figure 5.6: An inclusive spectrum of $M(K^+K^-)$ from ~ 4 pb^{-1} of the electron data.

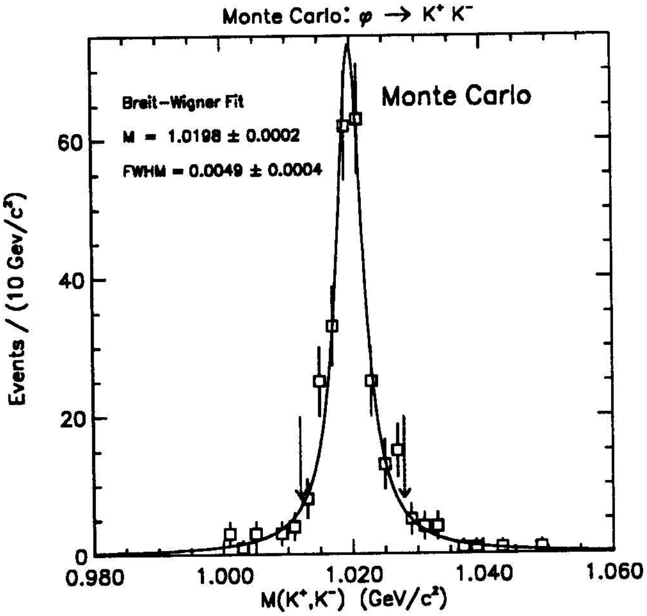

Figure 5.7: Monte Carlo M_{KK} distribution for the $\phi \rightarrow K^+K^-$.

ϕ candidates are combined with another track of $p_T > 0.8$ GeV/c which has an opposite charge to the lepton and which is also inside the cone for the D_s^-. Such combinations are called 'right sign' combinations. This third track is assigned the pion mass.

All three candidate tracks (K^+, K^- and π^-) are vertex constrained in 3-D space as described in the Chapter 3. The resulting vertex point is called V_D. The χ^2 probability of the vertex fit has 3 degrees of freedom and is required to satisfy

- Prob$(3, \chi^2) > 0.1\%$

At least 2 out of the three candidates (K^+, K^- and π^-) must pass the following track quality requirements.

- At least 2 axial superlayers which have 4 or more hit wires.
- At least 2 stereo superlayers which have 2 or more hit wires.
- Number of SVX hits ≥ 2 and $\chi^2_{SVX} < 30$.

Furthermore, the D_s^- decay vertex, V_D is required to be positively displaced from the primary vertex along the direction of the lepton-D_s momentum: i.e.

- $L_{xy} > 0$

The efficiencies of the selection criteria (χ^2 probability cut, the L_{xy} cut and even the isolation cut) can be estimated using the $D^{*-} \rightarrow K^+\pi^-\pi^-$ events as a control sample. The topology and the kinematics of the $D^{*-} \rightarrow K^+ \pi^-\pi^-$ and the $D_s^- \rightarrow K^+K^-\pi^-$ cases are very similar. For this efficiency estimate, D^{*-} candidates are selected using the previous cuts but without the χ^2 probability, the L_{xy}, and the isolation cuts. Two samples are defined, one for the signal, and one for the background. Both samples use only the right sign combinations ($K^+\pi^-\pi^-$):

signal sample	$\Delta M < 0.155$ GeV/c^2
	$\lvert M(K^+\pi^-) - 1.864\rvert < 0.025$ GeV/c^2
background sample	$\Delta M > 0.155$ GeV/c^2

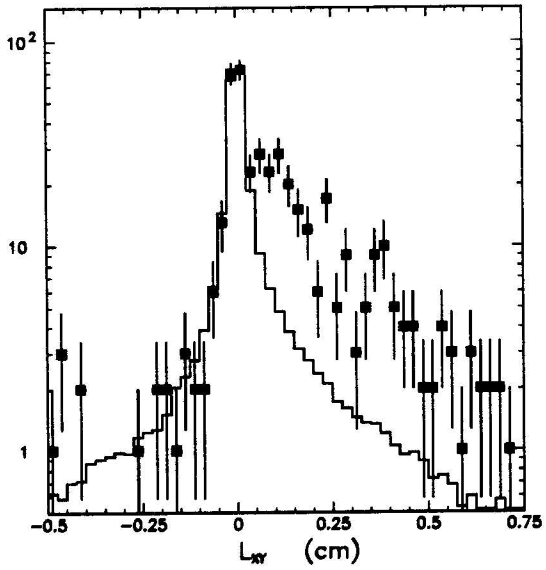

Figure 5.8: L_{xy} distribution of the $\ell^- D^{*+}$ sample (points) and the background sample (histogram).

The L_{xy} distributions are shown in Figure 5.8 for the signal and background samples. The backgrounds are distributed quite symmetrically around zero, but the signals are more positive. The efficiency for $L_{xy} > 0$ cut is $\sim$ 87%. Distributions of the Prob(3, χ^2) for the D^{*-} signal and its background samples are shown in Figure 5.9. The 1% cut efficiency is estimated to be about 84%.

For a better D_s identification, the isolation cut discussed earlier must be used to remove the large fake background which are due primarily to light QCD jets with soft fragmentation and high multiplicity. The isolation cut used is

- $E_T^{\text{iso}}/P_T(K^+K^-\pi^-) < 1.2$

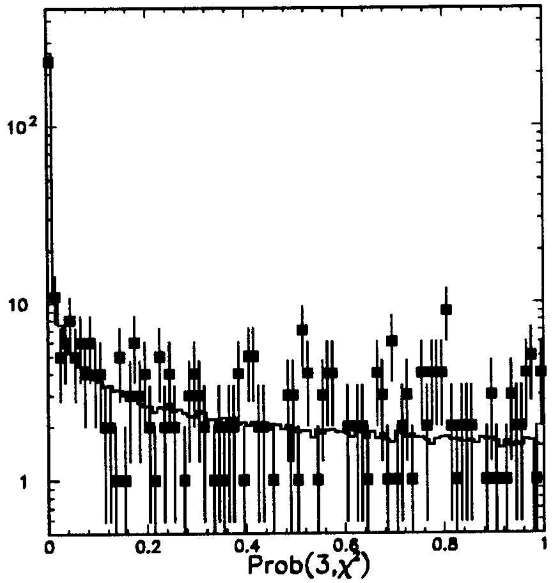

Figure 5.9: Distribution of the probability of the vertexing χ^2 from the e^-D^{*+}(see points) and from the 'background sample'(histogram).

The D^{*-} control samples can also be used to study the efficiency of this isolation cut. The plots of the $E_T^{\text{iso}}/P_T(K^+\pi^-\pi^-)$ from the D^{*-} control samples are shown in Figures 5.10(a) (b) for the electron and muon data respectively. The points are the background subtracted D^{*-}. A large portion ($> 50\%$) of the backgrounds can be eliminated by this cut while keeping about 76% and 78% efficiency for the signals (electron and muon respectively). It is also worth noting that since the D^{**}, which contributes to the D^{*-} but not the D_s sample, would make the actual efficiency for the D_s higher than the numbers we get here.

One useful aspect of the $D_s \rightarrow \phi\pi^-$ decay is that it has a non-uniform helicity angle distribution. In the ϕ rest frame where the K^+ and K^- go back to back, the

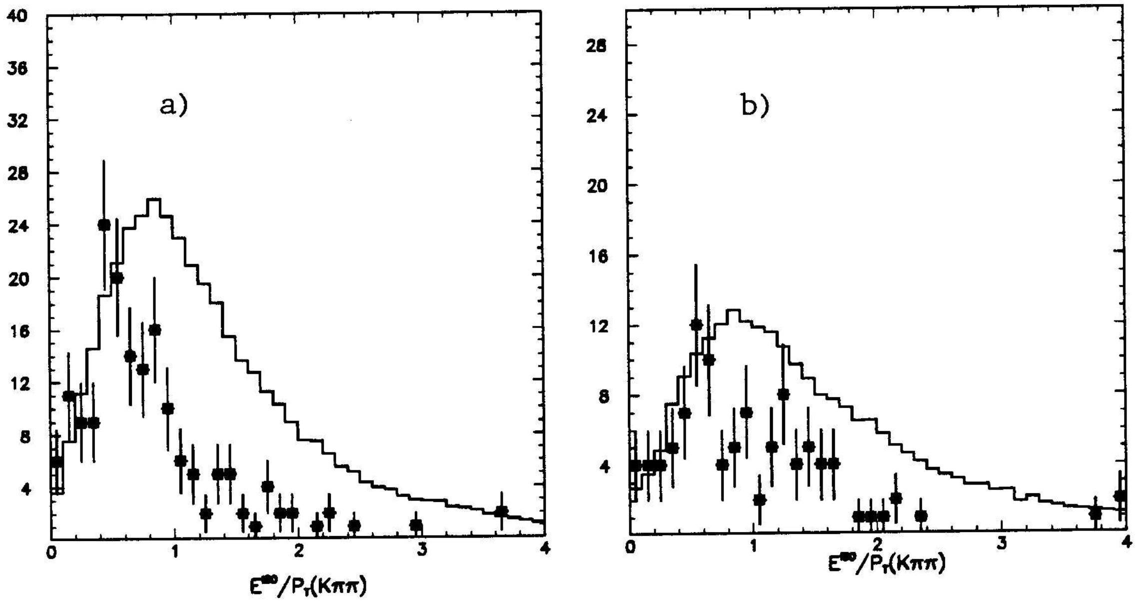

Figure 5.10: $E_T^{iso}/P_t(D^{*+})$ plots (a) for $e^- D^{*+}$ sample after the background subtraction (points) and the background sample (histogram). (b) for $\mu^- D^{*+}$ sample after the background subtraction (points) and the background sample (histogram).

'helicity' angle Ψ is defined as the opening angle between the K^+ and the pion (see Figure 5.11). The backgrounds have no preferred direction and should have a flat $\cos\Psi$ distribution. However in the decay of $D_s^- \rightarrow \phi\pi^-$, because the ϕ is a spin 1 vector meson and all the other particles (D_s^-, π^-, $K^\pm$) are spinless pseudo scalars, total angular momentum conservation permits only the $L = 1$ state of orbital angular momentum for the K^+K^- system. This leads to a unique helicity angle distribution of $dN/d(\cos\Psi) \sim \cos^2\Psi$. The cut requires that

- $|\cos\Psi| > 0.4$.

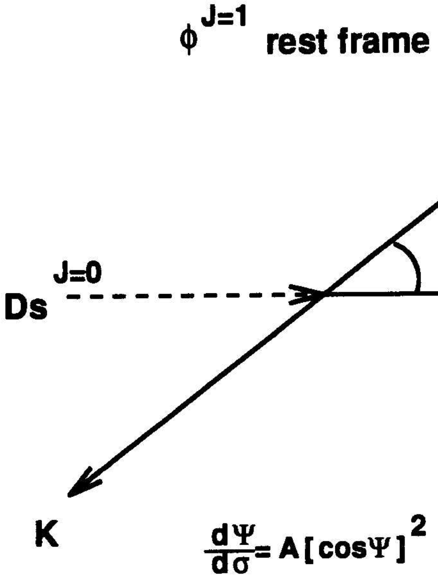

Figure 5.11: Definition of the helicity angle

This rejects 40% of the background while keeping 92% of the signal. A comparison of the $\cos\Psi$ distributions between the candidate D_s signals and the sideband data (normalized to the background level within the signal region) is plotted in Figure 5.12. All the selection cuts described in this section are used in this plot except the helicity cut. The window for the signal is $1.953 - 1.981$ GeV/c^2 and the sidebands are $1.885 - 1.945$ GeV/c^2 and $1.990 - 2.050$ GeV/c^2. The curve represents a fit of the form $C + A\cos^2\Psi$.

Finally, the mass of the ℓD_s system is required to be

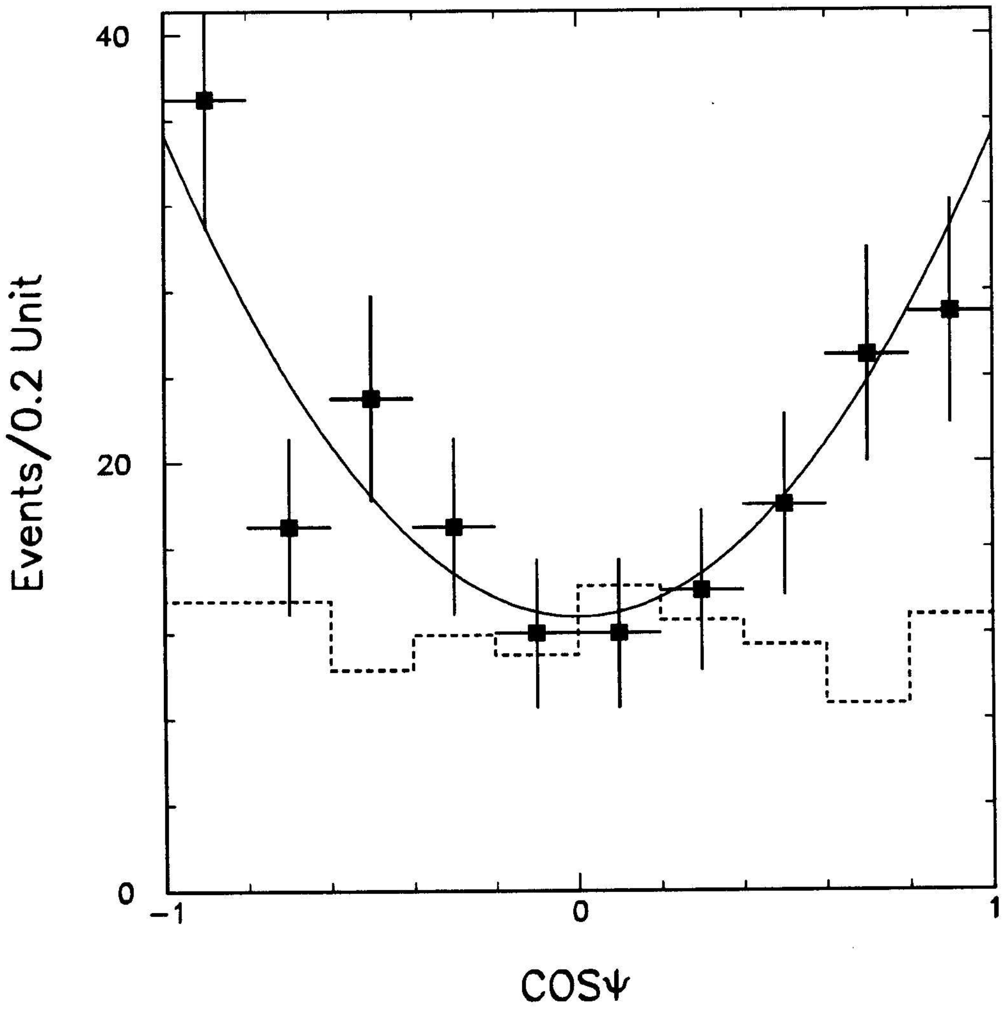

Figure 5.12: $\cos(\psi)$ distributions of the data from the signal region $1.953 < M(K^+, K^-\pi^-) < 1.981$ GeV/c^2 (points) and from the sideband region 1.885-1.945 and 1.990-2.050 GeV/c^2 normalized to the number of background events in the signal region (dashed histogram). The curve is a fit to the data of the form $C + A\cos^2\psi$.

- $3 < M(\ell D_s) < 6$ GeV/c^2

A Monte Carlo plot of the $M(\ell D_s)$ is shown in Figure 5.13 (a) where the corresponding distribution for the sideband data is also plotted. The cut is almost 100% efficient for the signal. Shown in Figure 5.13(b) is the $M(\ell D_s)$ distribution for the signal region after the background subtraction. This has a distribution similar to that of the Monte Carlo signal but quite different from the sideband distributions.

All cuts and efficiencies are summarized in Table 5.3.

Figure 5.14(top) shows the $\phi\pi^-$ invariant mass distribution for the 'right sign' lepton-D_s combinations. The D_s peak is shown and a hint of the Cabibbo suppressed $D^- \rightarrow \phi\,\pi^-$ decay signals is also seen. No enhancements are seen in the corresponding distribution for the 'wrong sign' combinations (see Figure 5.14 (bottom)).

The fit shown in Figure 5.14(a) is performed with the following requirements: (1) The background is parameterized by a linear function, (2) the gaussian width of the D_s^- is allowed to float, (3) the gaussian width of the D^- is fixed by the ratio $M(D^-)/M(D_s^-)$ times the width of the D_s^- (4) The mass region $M(\phi\pi^-) <$ 1.833 GeV/c^2 is excluded from the fit. A binned log-likelihood method is used. The results of the fit are listed in Table 5.4. The signal region is defined to be $1.953 < M(\phi\pi) < 1.981$ GeV/c^2 (or $\pm 2.5\sigma$). A total of 147 events are observed in this interval. The number of signal event is 77 ± 8.6 after subtracting the expected background. Figure 5.15 also shows the $M(K^+K^-\pi^-)$ spectrum for the electron and the muon

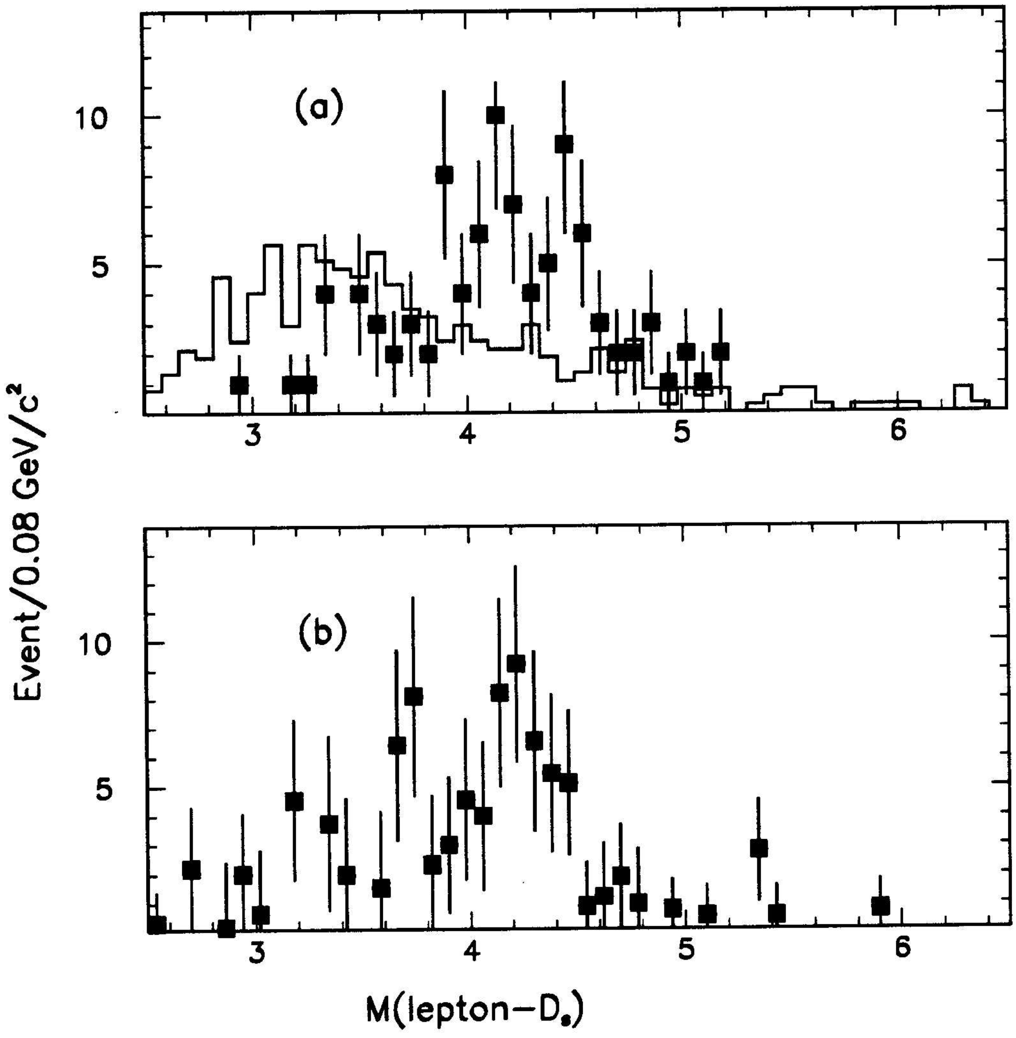

Figure 5.13: (a) The $M(\ell D_s)$ distribution for the Monte Carlo data (points). The histogram is a distribution for the sideband data. (b) The $M(\ell D_s)$ distribution for the signal region after the background subtraction.

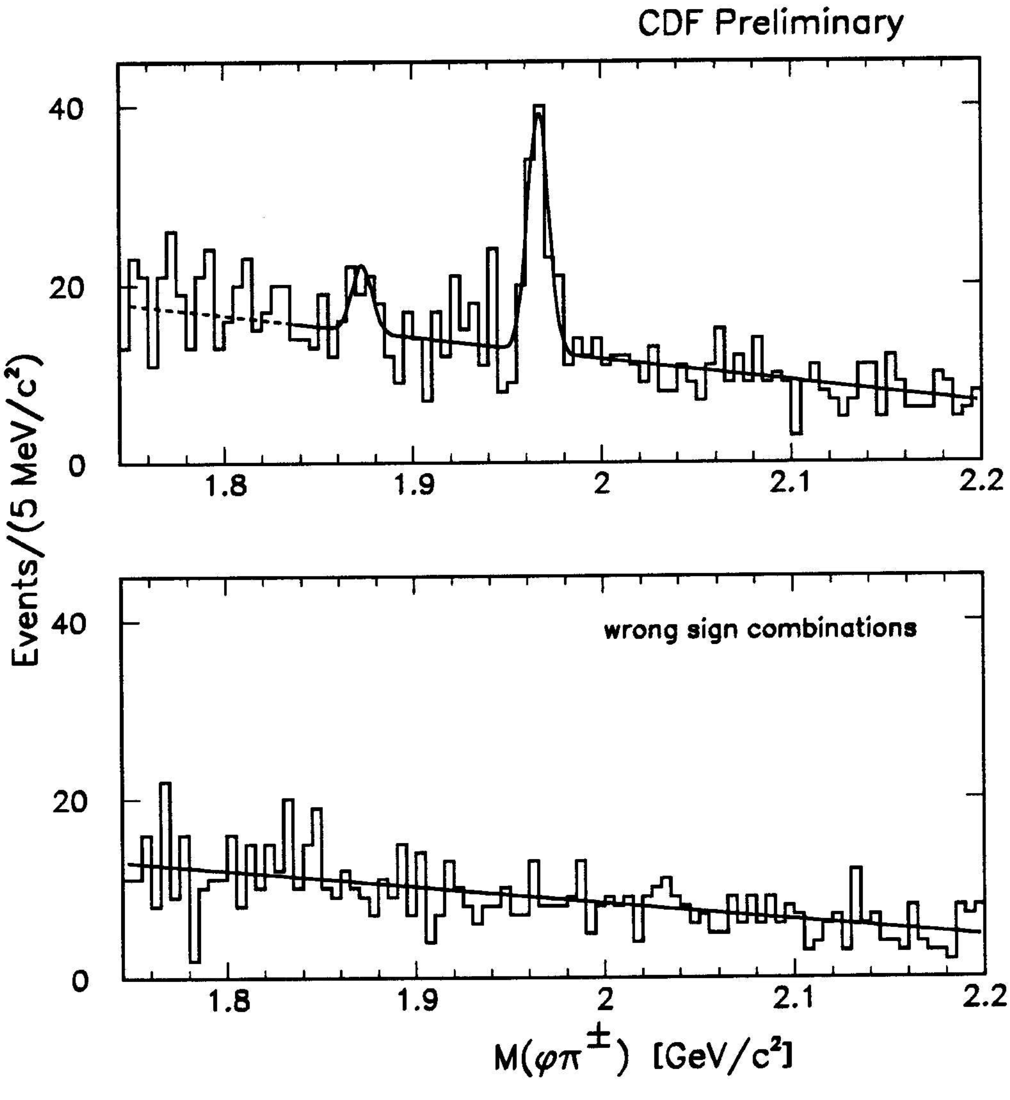

Figure 5.14: $M(\phi\pi^{\pm})$ from right sign combinations $(\ell^{\mp}\phi\pi^{\pm})$. (bottom) $M(\phi\pi^{\pm})$ from wrong sign combinations$(\ell^{\pm}\phi\pi^{\pm})$.

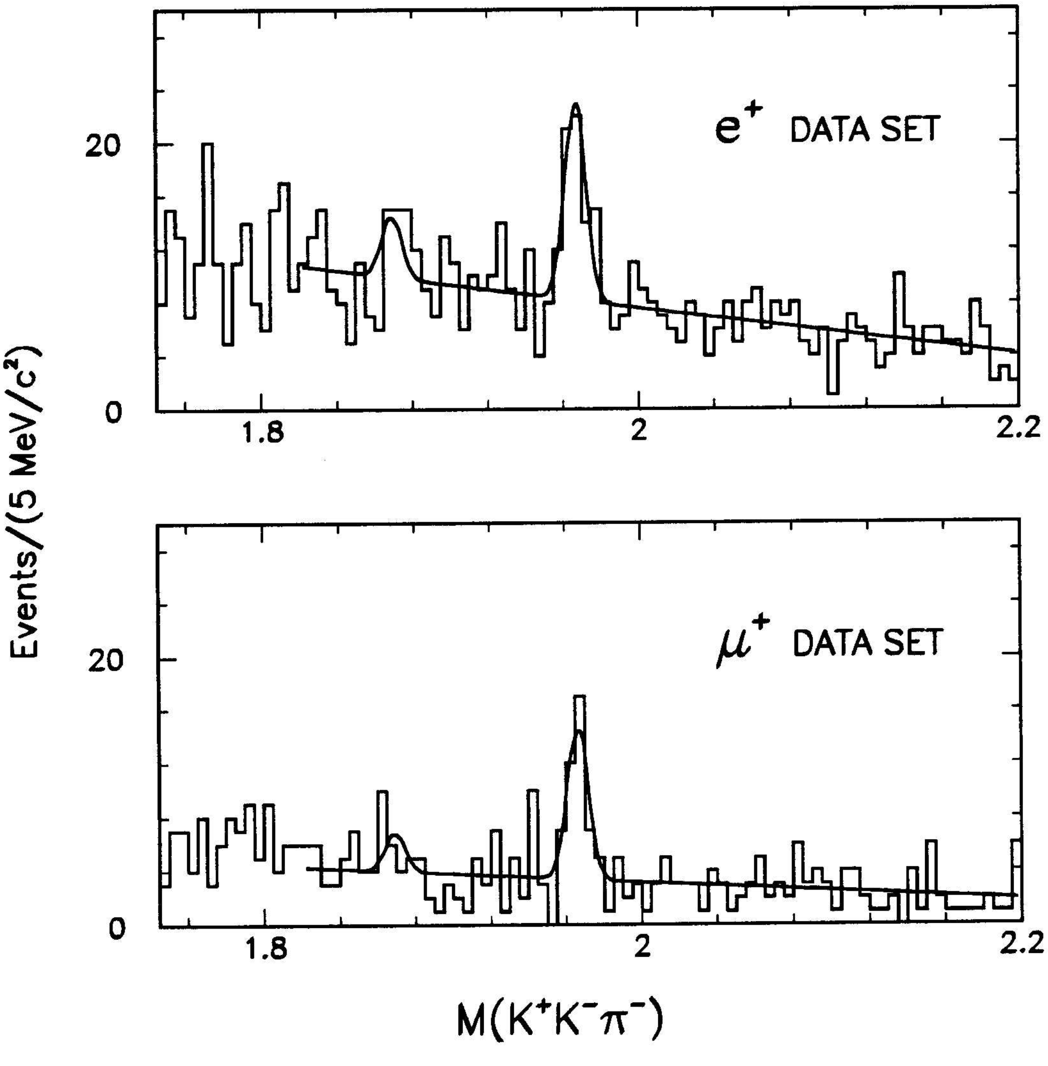

Figure 5.15: (top) $M(\phi\pi^-)$ from the electron data sample. (bottom) $M(\phi\pi^-)$ from the muon data sample.

Table 5.3: A list of the D_s^- selection cuts and efficiencies

D_s^- selection cuts	Estimated Efficiency e$^-$(μ^-)
Geometry + offline tracking	61%
$R = \sqrt{\Delta\phi^2 + \Delta\eta^2} < 0.8$	91%
p_T cut (K,π), $p_T(\phi) > 2$ GeV/c	66%
$\mathrm{Prob}(3, \chi^2) > 1\%$	84%
$\lvert M(K^+K^-) - 1.020\rvert < 8$ MeV/c^2	90%
$\lvert \cos\Psi \rvert > 0.4$	92%
$3 < M(\ell^-, \phi\pi^+) < 6$ GeV/c^2	99%
$E_T^{iso}/P_t(\phi\pi^+) < 1.2$	76% (78%)
SVX$\geq$ 2 hits,$\chi^2_{SVX} < 30$	84%
$L_{xy} > 0$	87%
Total	14%

data separately.

Table 5.4: A table of fitting results of the $\phi\pi^-$ mass spectrum

Parameters	value	description
1	73.7 ± 8.6	gaussian area of D_s
2	1.9667 ± 0.0009 GeV/c^2	mean of D_s
3	5.5 ± 7 MeV/c^2	σ of D_s
4	19.4 ± 6.9	gaussian area of D^-
5	1.873 ± 0.003 GeV/c^2	mean of D^-
6	70.0 ± 2.0	number of background 1.953-1.981
7	-24.6 ± 2.7	slope of the background

Chapter 6

Vertices and Decay lengths

This chapter presents the basic elements of the lifetime measurement which are vertices and decay lengths. Of particular importance are those measurements made in the transverse plane, where the tracking detectors, especially the vertex detector, have the best precision.

6.1 Vertices

6.1.1 The Primary Vertex

The $p\bar{p}$ interaction point is where all primary particles are created. It is called the primary vertex V_p. As mentioned earlier in section 3.3, for a given event, the primary vertex can be approximated without bias by the averaged beam position from the same run. The resolution of the beam position is usually the size of the beam spot, $\sim$ 35 μm in both x and y directions. This is quite small compare to the typical resolution of a reconstructed secondary vertex ($\sigma \sim 100$ μm).

A transverse beam position can be expressed as a linear function of the event z vertex:

$$\begin{aligned} x_p &= x_0 + z \cdot s_x \\ y_p &= y_0 + z \cdot s_y, \end{aligned} \tag{6.1}$$

where the parameters x_0, y_0 and s_x, s_y are the offsets and the slopes of the beam position which are stored in the data base for each run. The lepton track is used to determine the z position here. A simple error matrix is assigned to this primary vertex.

$$\sigma_p = \begin{pmatrix} (35\ \mu\text{m})^2 & 0 \\ 0 & (35\ \mu\text{m})^2 \end{pmatrix} \tag{6.2}$$

6.1.2 The Secondary and Tertiary vertices

In addition to the primary vertex, the secondary and tertiary decay vertices must be measured, where the primary particle (B) and the secondary ones (D) decay respectively. Since charm also has a long lifetime, these two vertices can be separable in the experiment. A drawing of a typical B_s semileptonic decay event followed by a D_s decay is shown in Figure 6.1.

To determine the tertiary decay vertex V_D in our analysis, the vertex is reconstructed in 3-dimensional space with a constrained fit using all the tracks from the D meson decays(see section 3.4 for detail). The vertex position V_D and its covariance

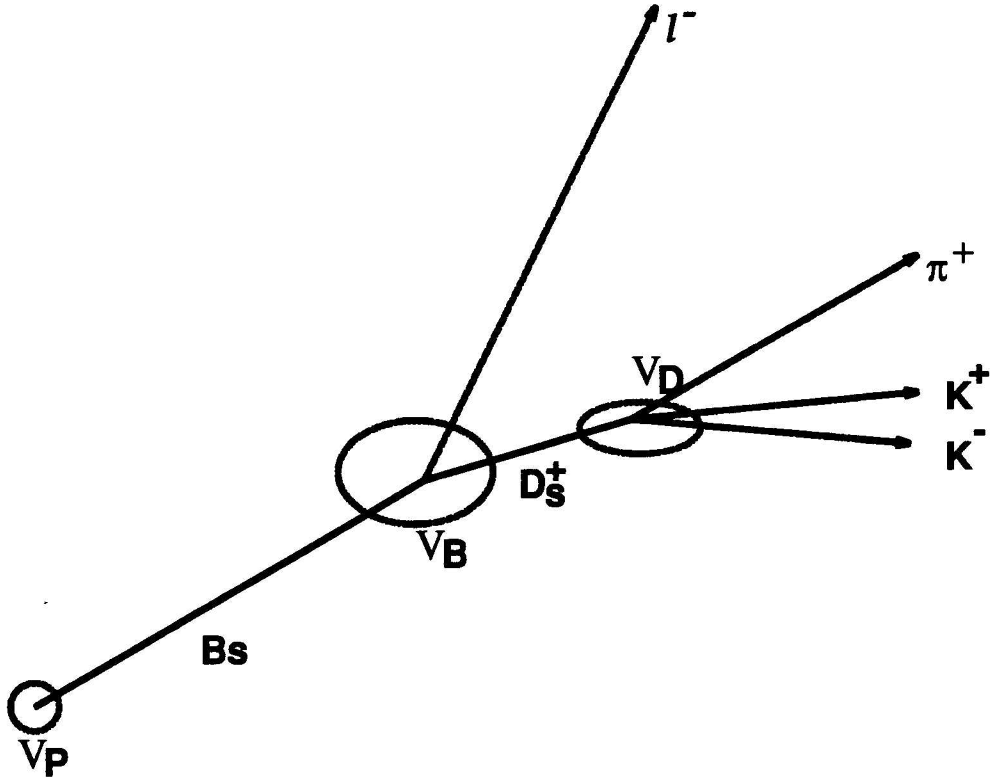

Figure 6.1: A diagram of a typical B_s semi-leptonic decay event

matrix σ_D are both improved by minimizing the χ^2:

$$\chi^2 = \sum_{i=1}^{3} \delta \mathbf{p_i}^t G_i^{-1} \delta \mathbf{p_i} \tag{6.3}$$

Given the position V_D and the flight direction $\vec{P}_T(D)$, the trajectory of the D can be determined in the transverse plane by

$$\begin{aligned} x &= X_D + r_D \sin\phi_D - r_D \sin\phi_D^0 \\ y &= Y_D - r_D \cos\phi_D + r_D \cos\phi_D^0, \end{aligned} \tag{6.4}$$

where ϕ_D^0 is the angle of the D at the decay point V_D, and r_D is the radius of the trajectory. The lepton trajectory is also defined by its track equation,

$$\begin{aligned} x &= r_\ell \sin\phi_\ell - (r_\ell^0 + d_\ell)\sin\phi_\ell^0 \\ y &= (r_\ell + d_\ell)\cos\phi_\ell^0 - r_\ell \cos\phi_\ell. \end{aligned} \tag{6.5}$$

Here d_ℓ and ϕ_ℓ^0 are the impact parameter and azimuthal angle of the lepton at the closest approach point, and r_ℓ is the radius of the lepton trajectory. In a magnetic field of 1.5 Tesla, any track of $p_T > 1$ GeV/c has a curvature of 0.15 m^{-1} or less. And so $\delta\phi$ is ≤ 0.3 mR for a travel length of 1000 μm. Therefore we can ignore the curvature effect here and the two trajectories can then be represented by two straight lines:

$$\begin{aligned} x &= S_\ell \cos\phi_\ell^0 - d_\ell \sin\phi_\ell^0 \\ y &= S_\ell \sin\phi_\ell^0 + d_\ell \cos\phi_\ell^0, \end{aligned} \tag{6.6}$$

where

$$\begin{aligned} x &= X_D - L_D \cos\phi_D^0 \\ y &= Y_D - L_D \sin\phi_D^0. \end{aligned} \tag{6.7}$$

The secondary decay vertex V_B can be found by intersection of these two lines. The covariance matrix of this vertex, σ_B can also be obtained from transforming the covariance matrix of the V_D, $\vec{P}_T(D)$ plus the covariance matrix of the lepton track (see appendix for detail).

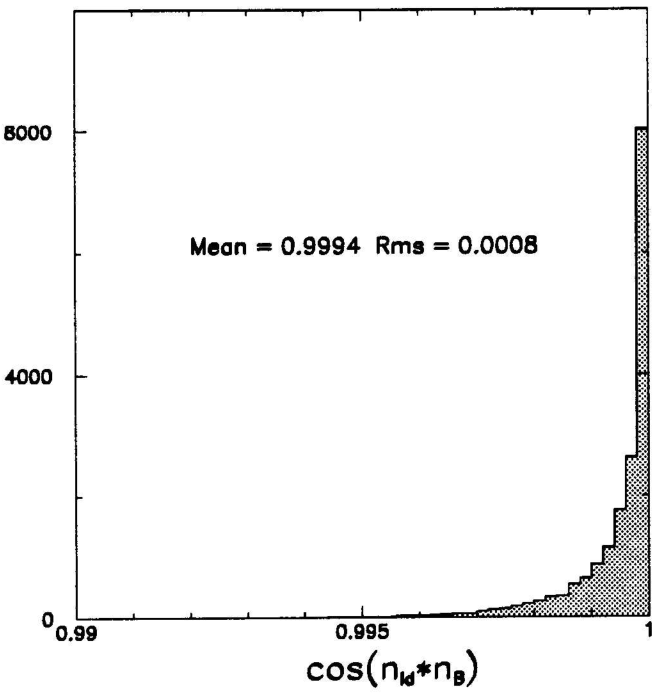

Figure 6.2: A Monte Carlo plot of the $\cos(\vec{n}_{\ell D_s} \cdot \vec{n}_B)$

6.2 Decay Lengths

In the semi-leptonic decay, the direction of the B in the laboratory is defined almost entirely by the direction of the ℓ-D system. The difference between the direction $\hat{P}_T(B)$ and the direction $\hat{P}_T(\ell D)$ is tiny. A Monte Carlo plot of the $\cos(\hat{P}_T(B)\cdot\hat{P}_T(\ell D))$ from the decay $B_s \to D_s^- \ell^+ \nu X$ is shown in Figure 6.2. The measurement uncertainty on the direction (typical a few MR) is also negligible in comparison to the vertex uncertainty.

One standard way of defining a decay length from any two vertex measurements is to find a scalar L^{prob} which minimizes

$$\chi^2 = (\vec{V}_2 - \vec{V}_1 - L\,\vec{n})^T \sigma^{-1} (\vec{V}_2 - \vec{V}_1 - L\,\vec{n}) \tag{6.8}$$

Here the covariance matrix σ includes the contributions from both vertices, ie. $\sigma = \sigma_1 + \sigma_2$ and $\vec{n}$ denotes the direction of the lepton-charm. The solution which is usually called the 'most probable' decay length is

$$L^{prob} = \frac{\vec{n} \cdot \sigma^{-1} \cdot (\vec{V}_2 - \vec{V}_1)}{\vec{n} \cdot \sigma^{-1} \cdot \vec{n}} \tag{6.9}$$

with its uncertainty

$$\sigma^2_{L^{prob}} = \frac{1}{\vec{n} \cdot \sigma^{-1} \cdot \vec{n}} \tag{6.10}$$

Another way of constructing a signed decay length is to take the displacement vector of the two vertices $\vec{V}_2 - \vec{V}_1$ and to find its projection length on the direction $\vec{n}$.

$$L = \vec{n} \cdot (\vec{V}_2 - \vec{V}_1). \tag{6.11}$$

The uncertainty of that is simply

$$\sigma^2_L = \vec{n} \cdot \sigma \cdot \vec{n}. \tag{6.12}$$

In the following, the latter decay length will be used, and a Monte Carlo calculation will be used to show that there is no bias between the two ways of defining the decay length.

This analysis must deal with three transverse decay lengths. The first is the transverse decay length of the B meson, which uses the vertex difference between V_B and V_P, and the direction $\vec{n} = \hat{P}_t(\ell D)$:

$$L_B = (\vec{V_B} - \vec{V_P}) \cdot \hat{P}_t(\ell D). \tag{6.13}$$

The second is the D meson transverse decay length. It is measured between V_D to V_B and the direction $\vec{n}$ is defined by the $\hat{P}_t(D)$:

$$L_D = (\vec{V_D} - \vec{V_B}) \cdot \hat{P}_t(D) \tag{6.14}$$

Finally, the apparent transverse decay length, L_{xy} which has been used for the previous event selection is from vertex V_D to V_P and in the direction $\vec{P}_t(\ell D)$:

$$L_{xy} = (\vec{V_D} - \vec{V_P}) \cdot \hat{P}_t(\ell D) \tag{6.15}$$

The decay lengths and their error calculations can be verified with Monte Carlo. In the following excise, the decay lengths measured from the Monte Carol data sample are compared with the decay lengths calculated from the true vertex positions that were generated before the simulation. The distributions of the differences between the two quantity are weighted by their uncertainties. Distributions of both the $\Delta L_{xy}/\sigma_{L_{xy}}$ and $\Delta L_B/\sigma_{L_B}$ are shown in Figure 6.3, where we also plot the most probable decay lengths L_{xy}^{prob} and L_B^{prob}. All the distributions shown are symmetric

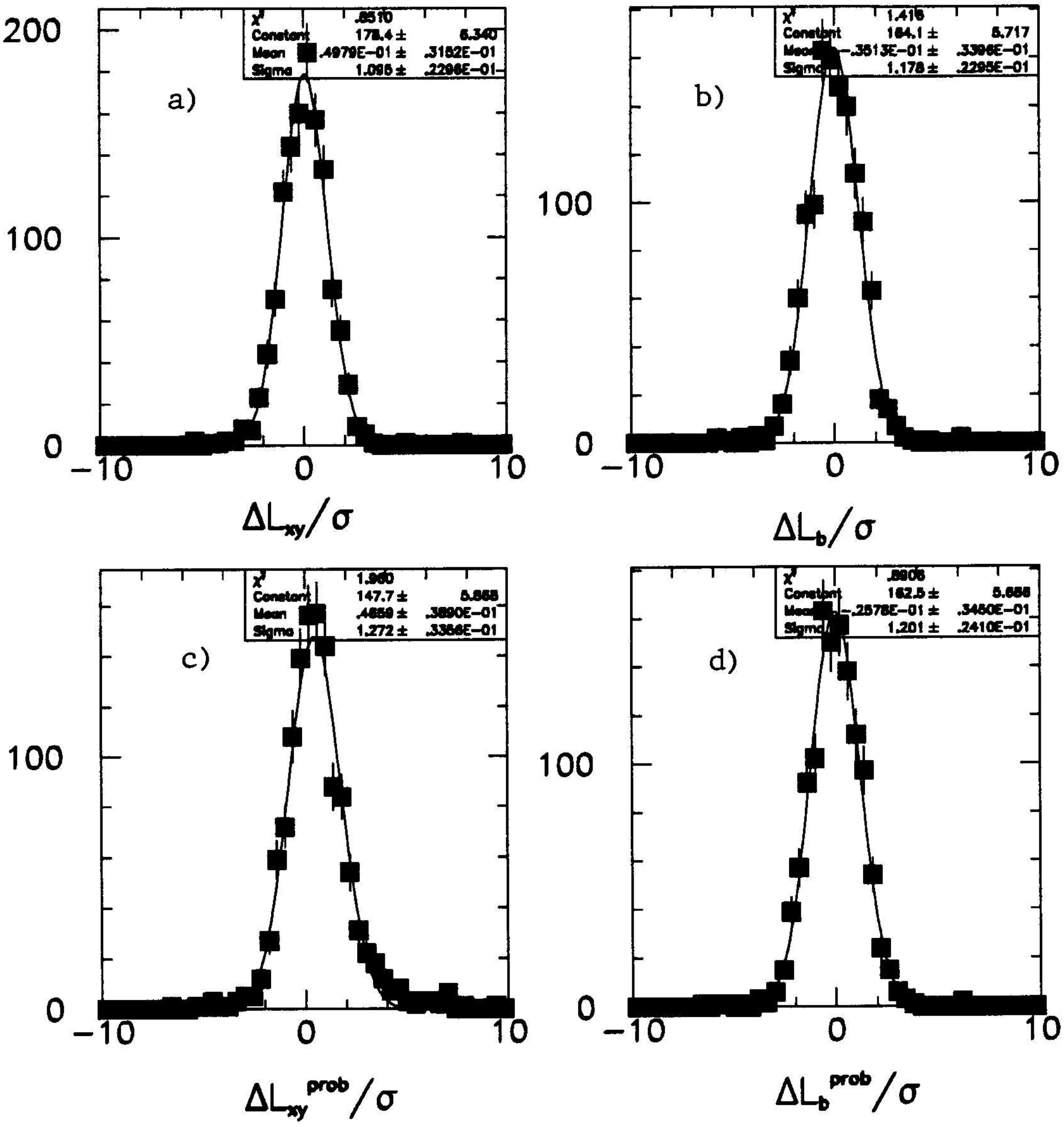

Figure 6.3: a)$(L_{xy}(OBSV) - L_{xy})/\sigma$, b)$(L_b(OBSV) - L_b)/\sigma$, c)$(L_{xy}(OBSV) - L_{xy}^{prob})/\sigma$, d)$(L_b(OBSV) - L_b^{prob})/\sigma$

around zero and can be well fitted by a single gaussian shape. The widths of all the gaussian distributions are also consistent (the fact that the widths are slightly larger than 1 is not understood yet). From this we conclude that both definitions of decay length are equally unbiased.

6.3 Proper Decay Length

The proper decay length ℓ is the decay length of a particle in the rest frame. It is related to the decay length L in the laboratory frame by a relativistic boost factor $\beta\gamma$.

$$\ell = \frac{L}{\beta\gamma} = \frac{L}{P(B)/M(B)} = \frac{LM(B)}{P(B)} \tag{6.16}$$

This can be expressed using the quantities in the transverse plane as

$$\ell = \frac{M(B)L\sin\theta}{P(B)\sin\theta} = \frac{ML_B}{P_t(B)} \tag{6.17}$$

where the L_B is the transverse decay length defined previously, and P_T is the transverse momentum of the B. However $P_T(B)$ is not completely measured in the semileptonic decays due to fact that the missing neutrino carries away some energy. The best that can be done then is to use the transverse momentum of the lepton-charm system as a partial replacement for $P_T(B)$. It has a ratio

$$K = \frac{P_T(\ell D)}{P_T(B)}, \tag{6.18}$$

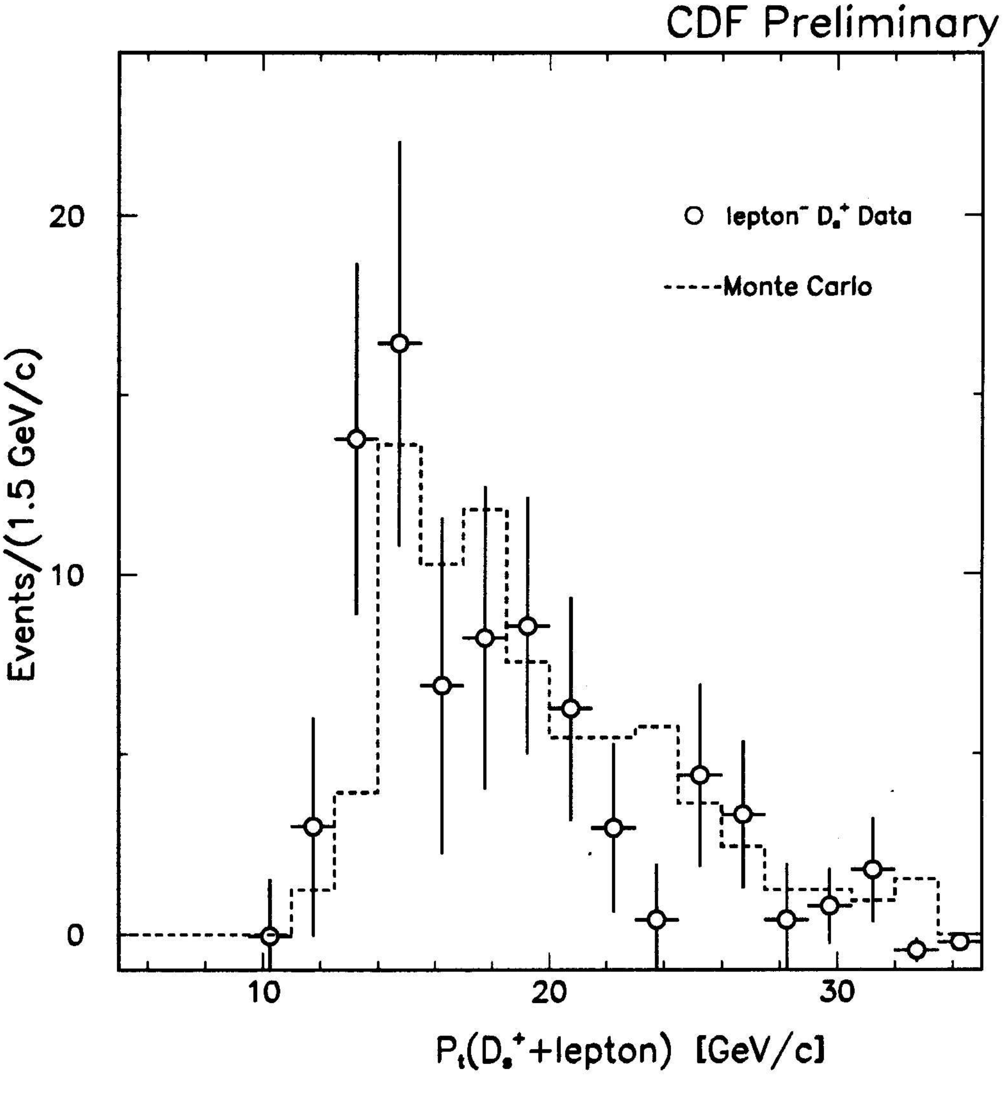

Figure 6.4: Comparison of the $P_t(\ell^- D_s^+)$ spectrum. Data (after the sideband subtraction) is plotted as points and Monte Carlo ($P_t(b) > 15$ GeV/c^2) distribution is plotted as a dashed histogram.

which is on average $\sim$ 85%. The proper decay length thus includes two parts, the quantities which are measured event-by-event and the factor K which is not known for each individual event, ie.

$$\ell = \ell_B \times K. \tag{6.19}$$

The ℓ_B is the transverse decay length L_B with the boost partially removed by the factor $P_T(\ell D)/M(B)$,

$$\ell_B \equiv \frac{L_B M(B)}{P_T(\ell D)} \tag{6.20}$$

This decay length ℓ_B is usually called pseudo $c\tau$ or $c\tau^*$.

The distribution of K, which will be referred to as the K^{dist} can be obtained from Monte Carlo data. A comparison of the $P_T(\ell D_s)$ distribution between the data and Monte Carlo is shown in Figure 6.4 to make sure that Monte Carlo gives the right P_T distribution of the lepton-D_s system. The K^{dist} generated from this Monte Carlo sample is now shown in Figure 6.5. The distribution has a mean of 0.86 and a RMS of 0.11. We also plot the K distribution (dashed histogram) from the events before the detector simulation (generator level). In this case, kinematic cuts on the decay products are the same as those used for selecting real data. The two K distributions are very close. This actually means the K behavior can be studied (see later chapter) without time consuming detector simulations.

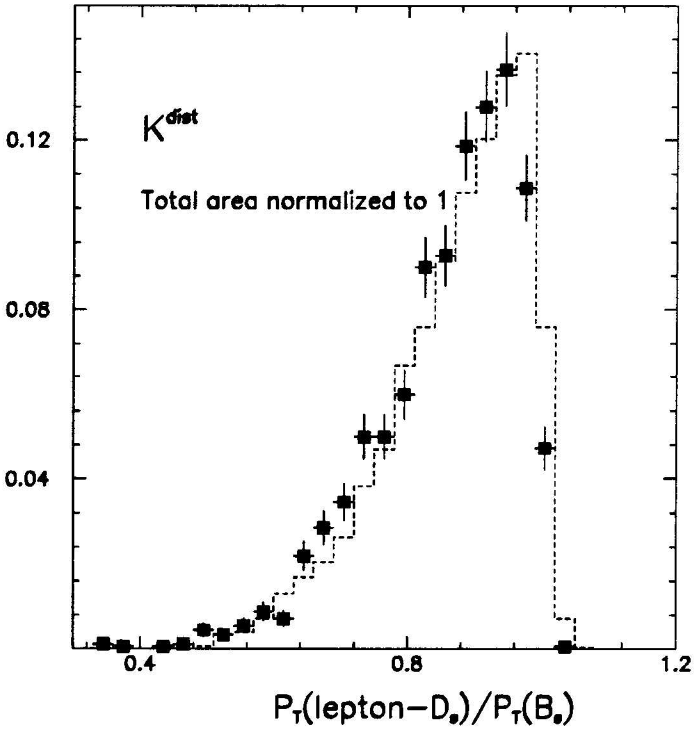

Figure 6.5: K distribution from $B_s \to D_s^- \ell^+ \nu X$ Monte Carlo decays. The points are from fully simulated events. The dashed histogram comes from generation level events.

Chapter 7

Data Sample

This chapter discusses the data samples for the lifetime measurement and the sources of background.

7.1 Signal Sample

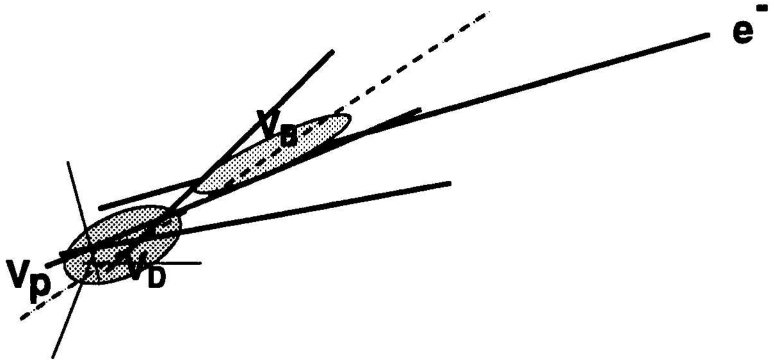

Figure 7.1: Schematic drawing of the fake vertices V_D and V_B which result in an anti-correlation between the ℓ_B and ℓ_D.

Before discussing the data sample, let us take a look at another selection cut which will help to reduce background combinations. For the signal, the B and D decay lengths

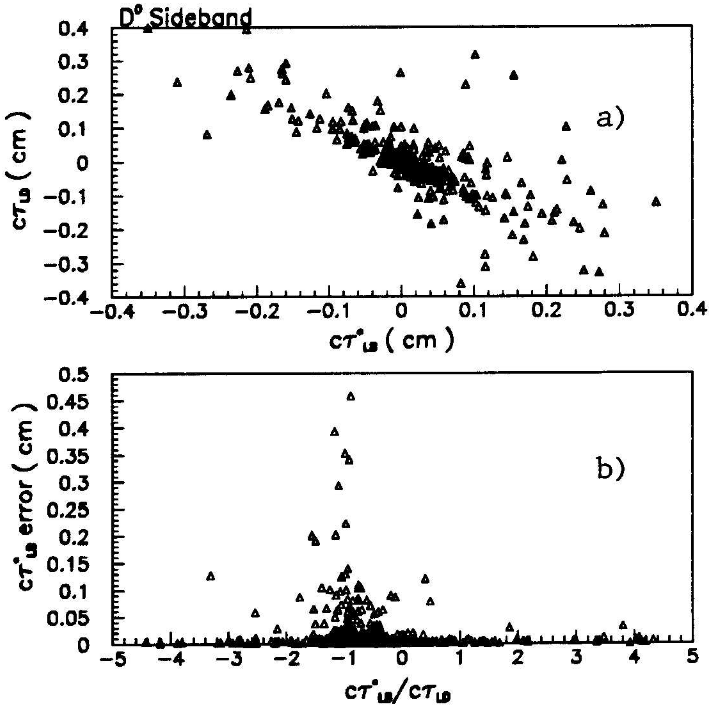

Figure 7.2: Decay length distributions for the D^0 side band. (a) Correlation between ℓ_D and ℓ_B. (b) Correlation between σ_{ℓ_B} and ℓ_B/ℓ_D.

ℓ_B and ℓ_D should be two independent quantities. However, in a situation, where the vertex V_D is a fake and the lepton track has large impact parameter (see Figure 7.1), or vice verse, the two measurements ℓ_B and ℓ_D are actually anti-correlated. As an example, Figure 7.2(a) shows the two decay lengths ℓ_B and ℓ_D in a scatter plot for D^0 sideband events. It shows a clear correlation along the diagonal line of $\ell_B + \ell_D = 0$ between the two lengths. Often these type of events also have unexpectedly large σ_{ℓ_B} as well. In Figure 7.2(b) is shown σ_{ℓ_B} versus the ratio ℓ_B/ℓ_D. It can be seen that points with large σ_{ℓ_B} tend to cluster around the line $\ell_B = -\ell_D$ which is the

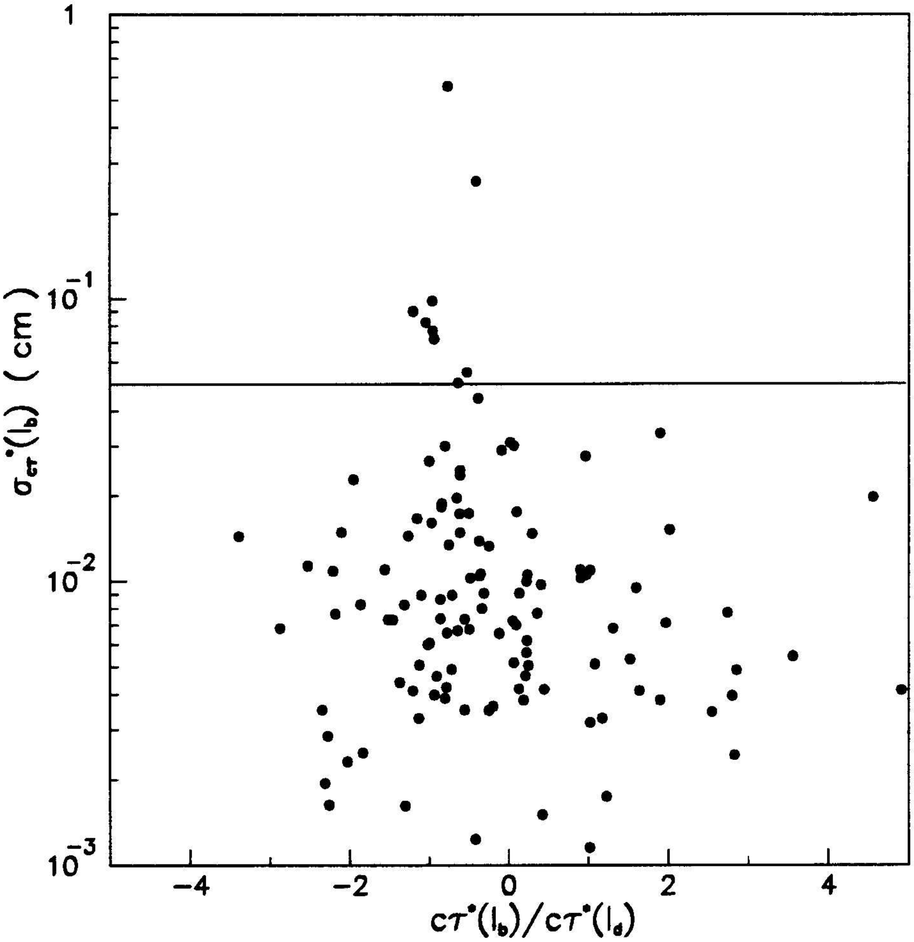

Figure 7.3: A scatter plot of the σ_{ℓ_B} verse the ratio ℓ_B/ℓ_D for the D_s^- signal region events

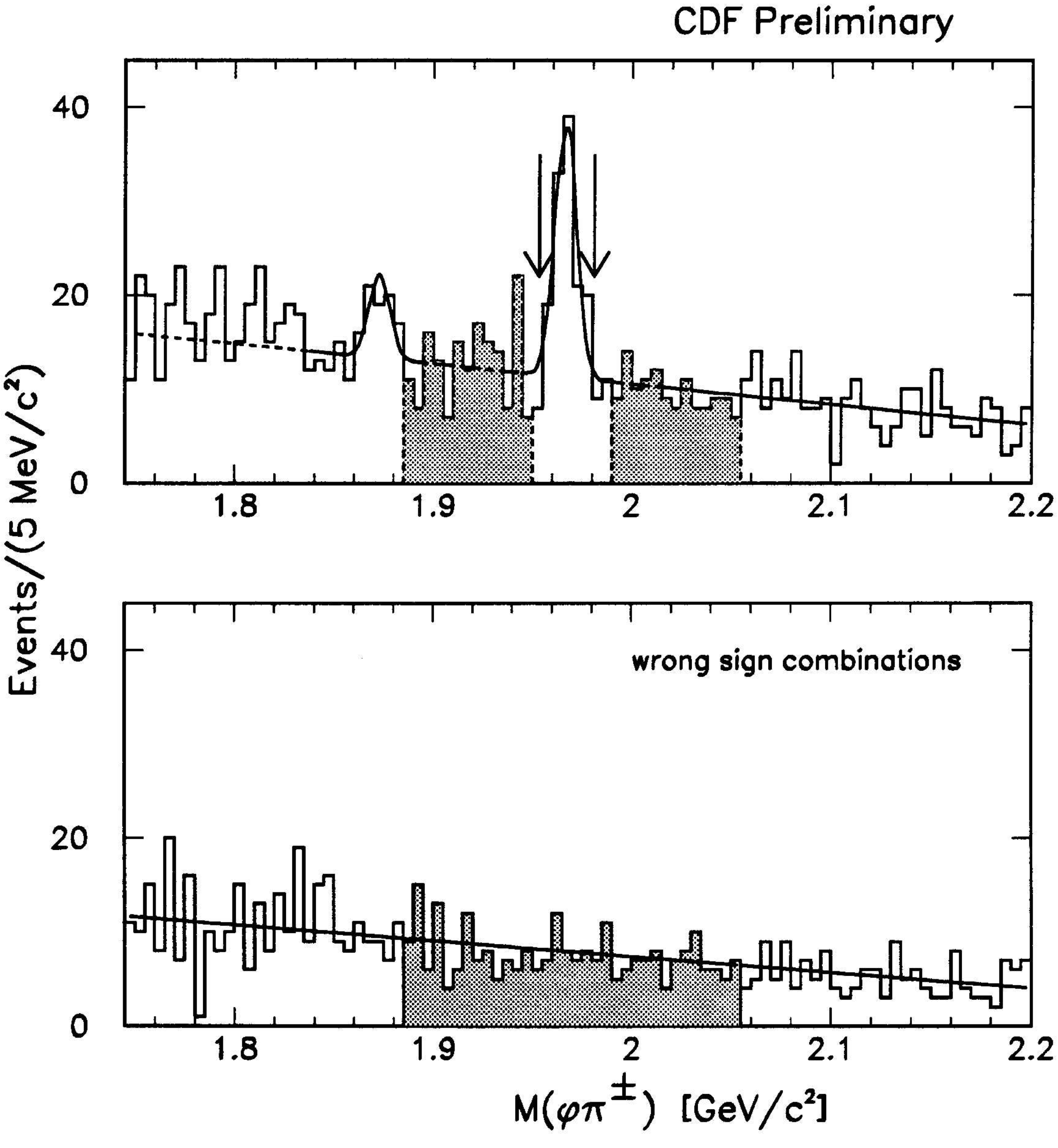

Figure 7.4: The three regions of the background samples (hatched) on the mass spectrum of $\phi\pi^-$. The arrows point to the interval for the signal sample which also contains the background events.

Table 7.1: A list of the fit parameters for the $\phi\pi^+$ mass spectrum after the σ_{ℓ_B} cut

Parameters	value	comments
1	73.4 ± 8.4	Gaussian area of D_s
2	$1.9664 \pm 0.0008\mathrm{GeV}/c^2$	mean of D_s
3	$5.4 \pm 0.7\mathrm{MeV}/c^2$	σ of D_s
4	23.2 ± 6.7	Gaussian area of D^+
5	$1.873 \pm 0.002\mathrm{GeV}/c^2$	mean of D^+
6	63.0 ± 1.9	number of background 1.953-1.981
7	-21.5 ± 2.5	slope of the background

anti-correlation. Those points can be removed by a cut

- $\sigma_{\ell_B} < 0.05$ cm.

The plot of the σ_{ℓ_B} versus the ratio ℓ_B/ℓ_D for the D_s signal region events is shown in Figure 7.3. 8 events which are along the line $\ell_B = -\ell_D$ will be removed by the above cut. The $\phi\pi$ mass spectra after applying this cut is shown in Figure 7.4. The parameters determined from the fit of the spectrum are listed in Table 7.1. There are a total of 139 events in the signal region where the expected number of background events from the fit is 63. The background ratio f_{bg} is thus 0.45. We can see by comparing with the Table 5.4 that the background ratio is reduced while the number of the signals seems unchanged, i.e 76.0 ± 8.2.

7.2 Non-B_s Background

B_s semileptonic decay is not the only source of the right sign signature $\ell^+ D^-$. In fact, there are three processes which can also lead to the same signature. Shown in Figure 7.5 are the Feynman diagrams of all the processes which in principle could contribute to $\ell^+ D_s^-$ production. Process(a) is the semileptonic B_s decay, which is the signal. Processes(b)(c) are the background sources from non-strange B meson decays. In the following we are going to discuss these two sources of background and will show that they are actually quite small. Process(d) which is a special case of (c) is negligible.

The process (b) can be written as

$$B_{u,d} \rightarrow D_s^{(*)-} \mathbf{K}\ \ell^+ \nu \tag{7.1}$$

which is a four body decay with the **K** (stands for any type of Kaon meson) emitted either before or after the weak decay vertex. So far there has been no experimental evidence of its existence. The ARGUS collaboration searched decays $B \rightarrow D_s^- K^-\ \ell^+ X$ and $B \rightarrow D_s^- K^0\ \ell^+ X$[24] and they set a limit (90% CL) on the branching ratio to be

$$\mathcal{B}(B \rightarrow D_s^- \mathbf{K} \ell^+ \nu X) < 1.2\%. \tag{7.2}$$

This number is less than 10% of the semileptonic B branching ratio. A detailed

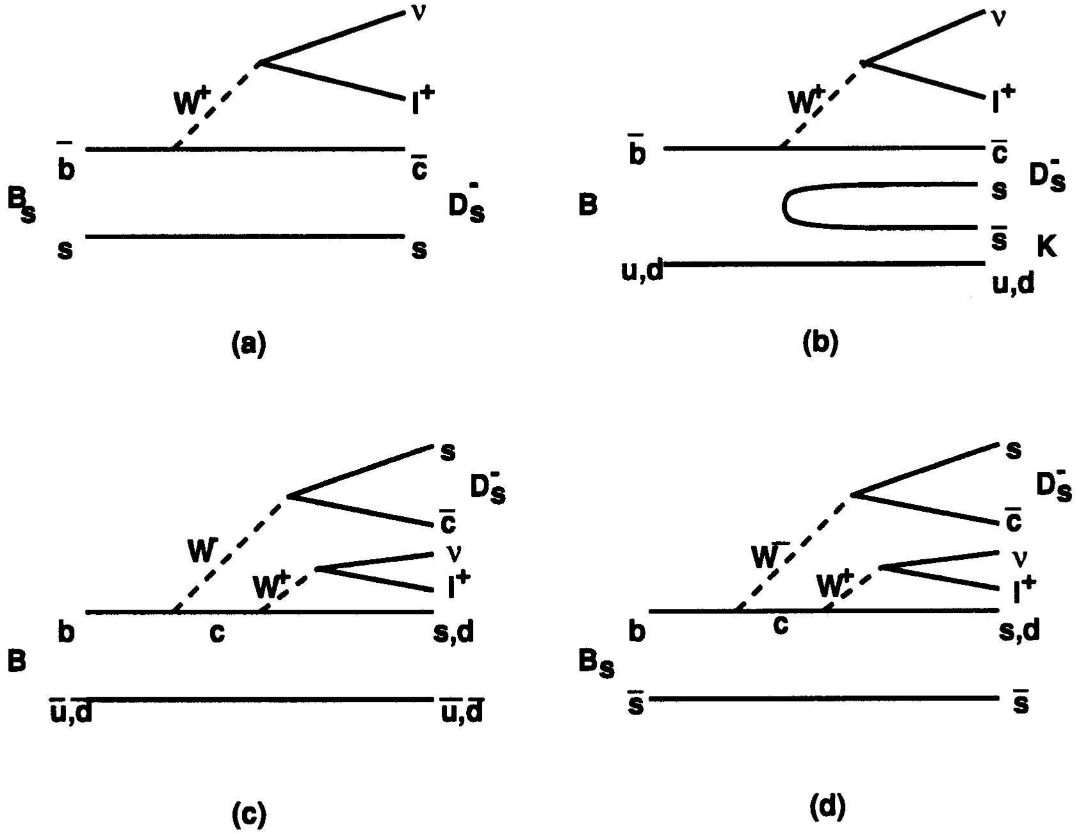

Figure 7.5: Feyman diagrams of all sources which lead to the $\ell^+ D_s^-$ associated production.

analysis based on the 'resonance model' was given by E. Golowich *et al.*[25]. They studied the contributions from real and virtual intermediate states.

- If the intermediate state is a real resonance, the only possible state allowing decay to the $D_s^- K$ are D^{**}. The branching fraction of D^{**} to $D_s K + \cdots$ is suppressed by two factors: the probability of creating the $s\bar{s}$ over say the $u\bar{u}$ from the sea which is $\leq 1/3$, and phase space suppression since only the highest $J^p = 2^+$ state $D^{**\pm}$ can decay to the lightest final state $D_s K^\pm$. The conservative assumption is 1/10. Therefore the decay width can be related to $\Gamma(B_{u,d} \rightarrow D^{**}\ell^+\nu)\mathcal{B}(D^{**} \rightarrow D_s K X) < 2.1\%\ \Gamma(B_s \rightarrow \ell^+\nu X)$.

- If the intermediate state is virtual, there are two diagrams (see Figure 7.6), the s-channel and u-channel, depending on whether the weak transition occurs before or after the strong K-production, i.e the $b\bar{q} \rightarrow (b\bar{s})K \rightarrow W^+ D_s^- K$ and the $b\bar{q} \rightarrow W^+(c\bar{q}) \rightarrow W^+ D_s^- K$. According to heavy quark symmetry, only the contribution from the ground states of virtual $b\bar{s}$ and $c\bar{q}$ is important, in which case, the two diagrams, cancel each other. A quantitative calculation yielded $\Gamma(B_{u,d} \rightarrow D_s \ell \nu X) < 0.5\%\ \Gamma(B_s \rightarrow D_s \ell^+ \nu X)$

The contributions from the two above cases lead to a limit on the branching ratio of the decay process(b)

$$\frac{\mathcal{B}(B_{u,d} \rightarrow D_s^- \mathbf{K} \ell^+ \nu)}{\mathcal{B}(B_d \rightarrow \ell^+ \nu X)} < 0.025 \tag{7.3}$$

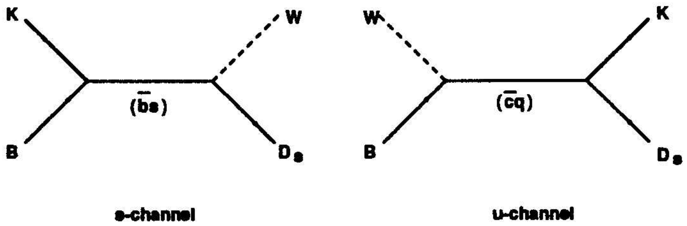

Figure 7.6: Diagrams of virtual intermediate states contributing to the process $B \rightarrow Ds^- K W^+$.

Also, the efficiency of finding the ℓ^+ and D_s^- from this type of decay is smaller compared to that from the B_s semileptonic decay. This is because the lepton spectrum tends to be softer. The extra kaon also reduces the efficiency of lepton identification. The Monte Carlo result is listed in Table 7.2, where the efficiency for the $B_s \rightarrow D_s^- \ell^+ X$ is normalized to 1. In the following we assume that $\mathcal{B}(B_s \rightarrow D_s^- \ell^+ \nu X) = 0.80\, \mathcal{B}(B_d \rightarrow \ell^+ \nu X)$. Assuming the production ratio of the flavors u, d, s to be $f_u : f_d : f_s = 3 : 3 : 1$, the background fraction of source(b) can be estimated using the branching ratio limit.

$$f_1 \;=\; \epsilon_1 \cdot \frac{(f_u + f_d)}{f_s} \cdot \frac{\mathcal{B}(B_{u,d} \rightarrow D_s^+ X_s \ell^- \bar{\nu})}{\mathcal{B}(B_s \rightarrow D_s^+ \ell^- X)} < 0.026 \qquad (7.4)$$

As for process(c), where the B decays hadronically to the D_s and D followed by the D semileptonic decay, ie.

$$\bar{B}_{u,d} \rightarrow D_s^{(*)-} D^{(*)} X, D^{(*)} \rightarrow \ell^+ \nu X \qquad (7.5)$$

the lepton comes from the cascade charm semileptonic decay. It is much softer and non isolated. As listed in Table 7.2 the lepton acceptance and identification efficiency is

Table 7.2: Efficiencies of all the $\ell^+ D_s^-$ sources

Selection	Efficiency		
	Process (a) $B_s \to \ell^+ D_s^- \nu$	Process (b) $B \to \ell^+ D_s^- \mathbf{K} \nu$	Process (c) $\overline{B} \to D_s^- D, D \to \ell^+ \nu X$
lepton acceptance	1.0	0.25	0.09
lepton efficiency	1.0	0.63	0.52
D_s acceptance	1.0	1.00	0.56
Total	1.0	0.16	0.026

very small. Even the D_s reconstruction efficiency is only 56% of the semileptonic case. The background fraction can be determined using the current measured branching ratios. Both the CLEO and ARGUS $\Upsilon(4S)$ experiments measured inclusive $B \to D_s X$ branching ratios: $\mathcal{B}(B \to D_s X)\mathcal{B}(D_s \to \phi\pi) = (3.06 \pm 0.47) \times 10^{-3}$ from CLEO and $\mathcal{B}(B \to D_s X)\mathcal{B}(D_s \to \phi\pi) = (2.92 \pm 0.50) \times 10^{-3}$ from ARGUS. The average value is $\mathcal{B}(B \to D_s X)\mathcal{B}(D_s \to \phi\pi) = (2.99 \pm 0.34) \times 10^{-3}$ from these two measurements. The branching ratio $\mathcal{B}(D_s \to \phi\pi)$ was inferred from the $\mathcal{B}(D^+ \to K^{*0} e^+ \nu)$ using the lifetimes $\tau(D^+)$ and $\tau(D_s^+)$ and assuming $\Lambda(D^+ \to K^{*0} e^+ \nu) = \Lambda(D_s^+ \to \phi e^+ \nu)$. The world average value is $\mathcal{B}(D_s \to \phi\pi) = (2.8 \pm 0.5)\%$ [23]. The number $\mathcal{B}(B \to D_s D X) < 0.80\, \mathcal{B}(B \to D_s X)$ will also be assumed. The charm meson semileptonic branching ratios are $\mathcal{B}(D^+ \to e^+ \nu X) = (17.2 \pm 1.9)\%$,

$\mathcal{B}(D^0 \rightarrow e^+\nu X) = (7.7 \ \pm 1.2)\%$ and $\mathcal{B}(D^0 \rightarrow \mu^+\nu X) = (8.8 \ \pm 2.5)\%$[23]. The background source(c) fraction is thus

$$f_2 \ = \ \epsilon_2 \cdot \frac{(f_u + f_d)}{f_s} \cdot \frac{\mathcal{B}(B \rightarrow D_s X) \cdot \mathcal{B}(D \rightarrow X\ell^+\nu)}{\mathcal{B}(B_s \rightarrow D_s^+ \ell^- X)} \simeq 0.026 \qquad (7.6)$$

7.3 Background Sample

In order to study the background events contained in the signal sample, a background sample is formed by using D_s^- sidebands and its wrong sign combinations. The sidebands are defined as the follows:

1. The low mass region is $1.885 \ \simeq M \ \simeq 1.945$ GeV/c^2. (Below 1.833 GeV/c^2, where $D^- \rightarrow \phi\pi^-$ happens, is excluded.)
2. The high mass region between 1.990 and 2.050 GeV/c^2.

Events from wrong sign combinations are used together with the sidebands , in order to gain statistics. We use the region between 1.885 and 2.050 GeV/c^2. The three regions of the background sample are high lighted in Figure 7.4. We summarize all the signal and background samples is in Table 7.3.

Table 7.3: A list of the signal and background samples for the lifetime measurement.

Sample	Selection (GeV/c^2)	Events
Signal	‘right sign’	139
	1.953-1.981	(f_b=0.45)
Background	‘right sign’	
	1.885-1.945	118
	1.990-2.050	158
	‘wrong sign’	
	1.885-2.050	276

Chapter 8

Lifetime Fitting

This Chapter discusses the determination of the B_s lifetime from the distribution of the decay length ℓ_B using selected data samples. Maximum log-likelihood methods are used in fitting the data, the overall likelihood function $\mathcal{L}$ is computed as a function of fitting parameters by multiplying together the normalized probability $\mathcal{P}^i$ of every event,

$$\mathcal{L} \;=\; \mathcal{P}^1 \cdot \mathcal{P}^2 \cdot \mathcal{P}^3 \cdots \tag{8.1}$$

The best fit is the one which maximizes the $\log \mathcal{L}$.

8.1 Unbinned Log-likelihood Function

In the selected 'signal sample', in addition to the source of signal (B_s) there is a fraction ($f_{bg} = 0.45$) of background from combinatorial sources. In order to determine the lifetime of the signal, the decay length ℓ_B distribution of the background must be known. This background shape is obtained from the ℓ_B distribution of the selected 'background sample'. The shape can then be subtracted from the 'signal sample' later. In practice however, both samples (signal and background) are used to fit for the lifetime and the background shape together. In this way, the background statistics are effectively increased by including those background events contained in the 'signal sample' in the fitting as well as those in the background sample. The joint likelihood function $\mathcal{L}$ can be written as

$$\mathcal{L} = \prod_{i}^{\{\mathrm{S}\}}\{(1-f_{bg})\mathcal{F}_{SG}^{i} + f_{bg}\mathcal{F}_{BG}^{i}\} \cdot \prod_{j}^{\{\mathrm{B}\}} \mathcal{F}_{BG}^{j}. \tag{8.2}$$

Here i and j are the index of the event from the 'signal sample' and 'background sample' respectively. {S} denotes the 'signal sample', the likelihood function of which contains a sum of two probabilities: $(1 - f_{bg})\mathcal{F}_{SG}$ for the signal contribution and $f_{bg}\mathcal{F}_{BG}$ for the background contribution. {B} stands for the 'background sample', which has a likelihood function of simply $\mathcal{F}_{BG}$.

8.2 The Signal Function

For a particle which decays with lifetime τ, the normalized distribution of the proper decay length is represented by an exponential function with only positive decay lengths, i.e,

$$\mathcal{E}_{\ell>0}(\ell, c\tau) \equiv \begin{cases} \frac{1}{c\tau}e^{-\ell/c\tau} & \text{if } \ell > 0 \\ 0 & \text{otherwise} \end{cases} \tag{8.3}$$

However, the measured quantity is the decay length in the lab, $\ell_B = \ell/K$, not the proper decay length, and there is no information about K directly from the data. Therefore all possible K values must be included in the probability distribution according to the K distribution (referred to as the K^{dist}), i.e,

$$\mathcal{E}_{\ell_B>0}(K\ell_B, c\tau) \overset{K}{\otimes} K^{dist} \tag{8.4}$$

Here, $\overset{K}{\otimes}$ represents a convolution over K. This is done with the histogram in Figure 6.5.

The above distribution must be further modified by smearing it with the measurement uncertainty in ℓ_B, i.e. σ_{ℓ_B} using a single Gaussian function

$$\mathcal{G}(x, \mathrm{s}\sigma_{\ell_B}) = \frac{1}{\sqrt{2\pi(\mathrm{s}\sigma_{\ell_B})}} e^{-\frac{x^2}{2(\mathrm{s}\sigma_{\ell_B})^2}}. \tag{8.5}$$

Here each decay length uncertainty σ_{ℓ_B} is multiplied by an overall scale factor **s**. The probability function for the signal is then:

$$\mathcal{F}_{SG} = \mathcal{E}_{x>0}(Kx, c\tau) \overset{K}{\otimes} K^{dist} \overset{x}{\otimes} \mathcal{G}(\ell_B - x, \mathrm{s}\sigma_{\ell_B}) \tag{8.6}$$

8.3 The Background Function

The background function is described by three distributions. The first is a pure Gaussian distribution, which represents the events that are composed of primary tracks.

$$\mathcal{F}_{BG_1} = \mathcal{G}(\ell_B, \mathrm{s}\sigma_{\ell_B}) \tag{8.7}$$

Since the measurement errors are not strictly gaussian, some fraction of the background events can have wider tails on both sides of the decay length due to poorly measured vertices. This should happen equally on the positive side and on the negative side. This kind of distribution can be parameterized by two symmetrically falling exponential functions with the same magnitude and slope, smeared with σ_{ℓ_B}.

$$\mathcal{F}_{BG_2} = [\mathcal{E}_{x<0}(x, -\lambda_-) + \mathcal{E}_{x>0}(x, \lambda_-)] \overset{x}{\otimes} \mathcal{G}(\ell_B - x, s\sigma_{\ell_B}) \tag{8.8}$$

Finally, since a large fraction of prompt leptons come either from bottom or charm decays, some real decay vertices are expected due to the combined bottom and charm lifetimes. There are represented by an exponential function convoluted with $\mathcal{G}$,

$$\mathcal{F}_{BG_3} = \mathcal{E}_{x>0}(x, \lambda_+) \overset{x}{\otimes} \mathcal{G}(\ell_B - x, s\sigma_{\ell_B}) \tag{8.9}$$

Thus, the background ℓ_B distribution function can be written as

$$\mathcal{F}_{BG}(\alpha_-, \alpha_+, \lambda_-, \lambda_+, s\sigma_{\ell_B}) = (1 - 2\alpha_- - \alpha_+)\ \mathcal{F}_{BG_1} + \alpha_-\ \mathcal{F}_{BG_2} + \alpha_+\ \mathcal{F}_{BG_3} \tag{8.10}$$

where $2\alpha_-$, α_+ are the non gaussian tails, and real decay contributions respectively.

8.4 Data Fitting

Before doing a unbinned fit, we have to make sure there is no correlation between the decay length ℓ_B and its uncertainty. Indeed Figure 8.1 shows an uncorrelated distribution of the σ_{ℓ_B} vs. ℓ_B from the 'signal sample' data. The average decay length uncertainty σ_{ℓ_B} of the data is 82 μm and the rms is 8.0 μm.

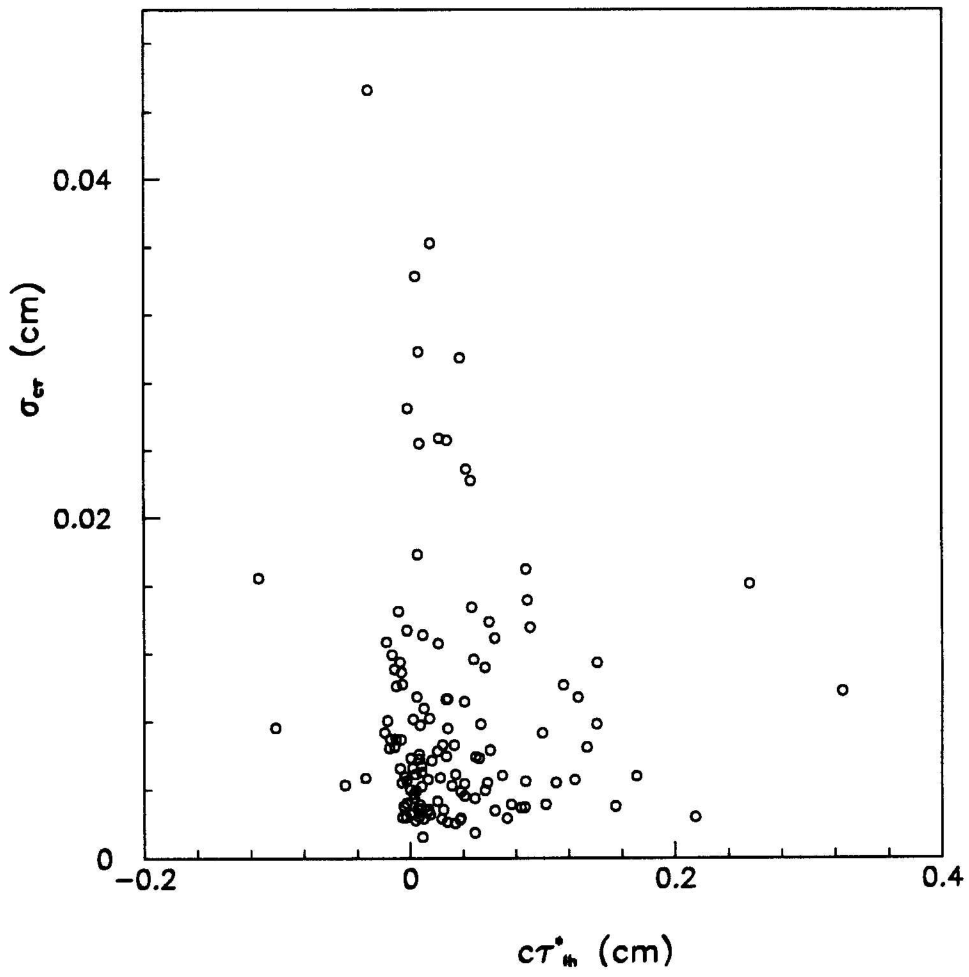

Figure 8.1: Distribution of σ_{ℓ_B} versus ℓ_B from the signal sample

In the fitting procedure, the f_{bg} variation is treated by an extra χ^2 term

$$-\frac{1}{2}\frac{(f_{bg}- < f_{bg} >)^2}{\sigma^2_{f_{bg}}} \tag{8.11}$$

which is added to the $\log \mathcal{L}$. This term constrains the background fraction to the value $< f_{bg} >= 0.45$ which was determined from the $\phi\pi^-$ mass spectrum fit. Since $\sigma_{f_{bg}}$ is 0.014 (see Table 7.1), the uncertainty (3%) of f_{bg} has a negligible effect on the fit.

Only the range [−0.4, 0.4] cm in the decay distribution is used to perform the fit. This is done because (a) few signals are expected beyond 0.4 cm, and (b) the background parameterization may not be appropriate for events at very large decay lengths.

The free parameters in fit are $c\tau$, **s** the error scale factor, f_{bg} the background fraction and the four parameters defining the background shape which are α_-, α_+, λ_-, λ_+. The fit results are listed in Table 8.1. The B_s lifetime is determined to be

$$\tau(B_s) \quad = \quad 1.42 \ ^{+0.27}_{-0.23} \text{ ps}. \tag{8.12}$$

The statistical error of the lifetime is $\sim$ 18%. Since this error is determined by varying all other parameters including the ones that define the background shape, the error quoted also includes the systematic uncertainty from the variation of the background shape.

We find that the background distribution contains a 9% contribution from long tails (α_-) ($\lambda_- > 1$ mm) on each side of the decay distribution (18% total). About 27%

Table 8.1: B_s lifetime fit result

Parameter	Best Fit Value
$c\tau$ (μm)	$426\ ^{+80}_{-68}$
s	$1.42\ \pm 0.10$
f_{bg}(%)	45.5 ± 1.3
λ_+(μm)	$371\ \pm 76$
α_+(%)	$27\ \pm 3$
λ_-(μm)	$1373\ \pm 278$
α_-(%)	$9\ \pm 2$

of the background distribution (α_+) comes from long lived particles ($\lambda_+ \sim 370$ μm). The rest ($1 - 2\alpha_- - \alpha_+ \approx 50\%$) is the prompt gaussian contribution.

The error scale factor required by the fit is about 40% larger than 1.0. This indicates that the decay length uncertainties are under estimated. The average decay length uncertainty σ_{ℓ_B} for the 'signal sample' data should then be $\sim$ 116 μm instead of 82 μm. We will discuss the error scale factor in chapter 9 which deals with systematic uncertainties.

Linear and semi-log plots of the ℓ_B distribution of the 'signal sample' data are plotted in Figure 8.2(a) and 8.3(a). The fitting function of the background and

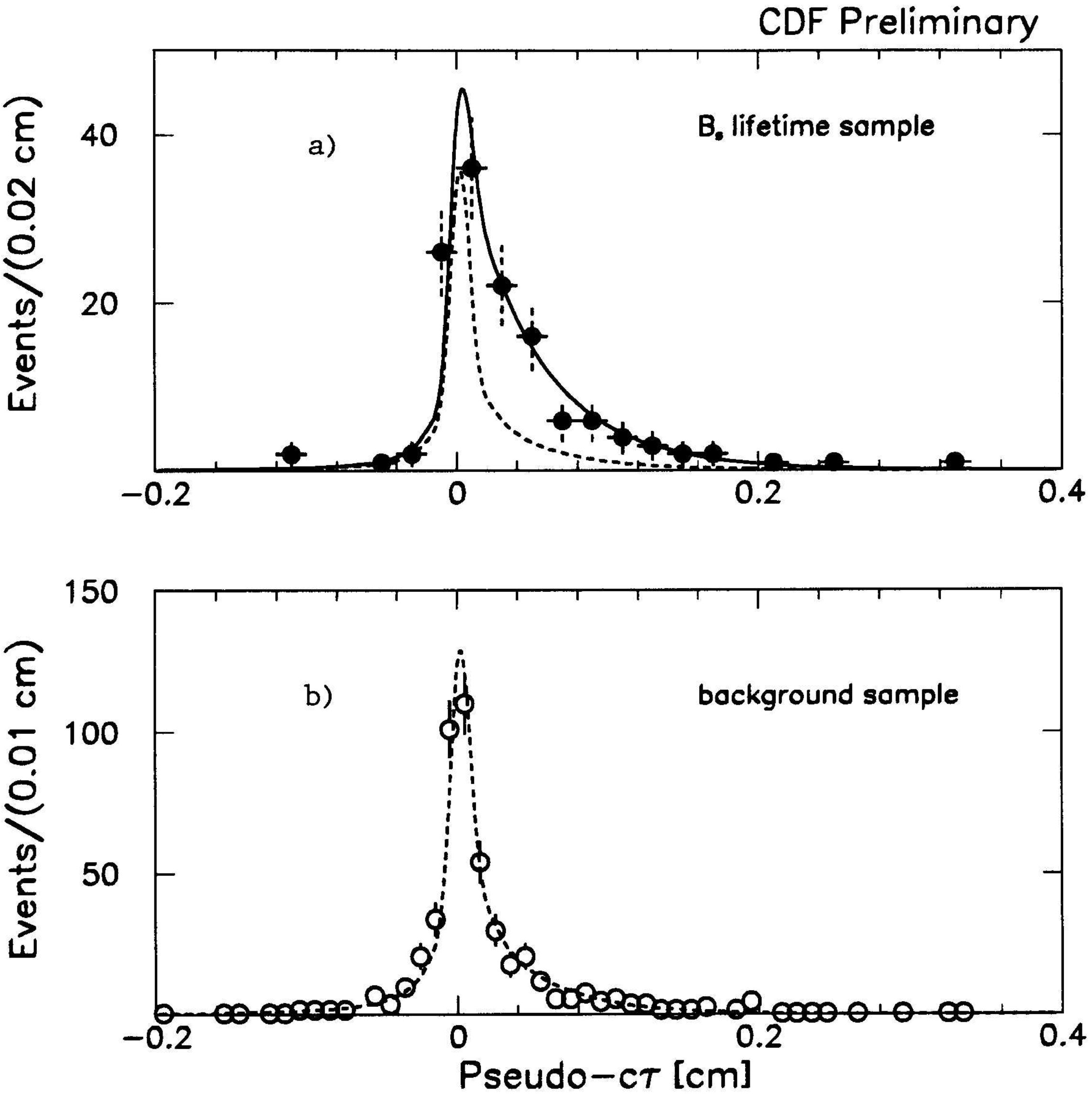

Figure 8.2: Distribution of the decay length ℓ_B for (a)the 'signal sample' and (b)the 'background sample'.

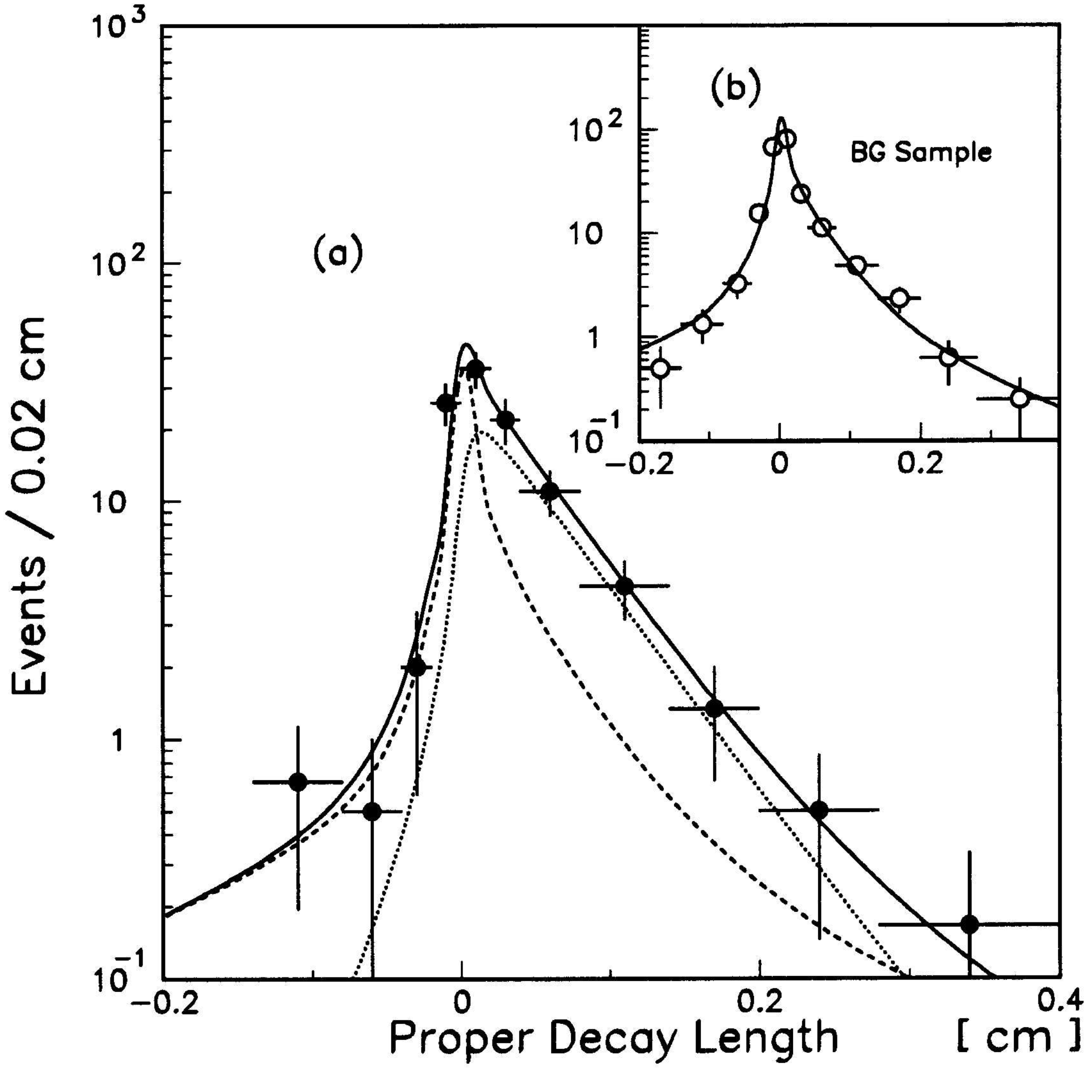

Figure 8.3: Distribution of the decay length ℓ_B for (a)the 'signal sample' and (b) the 'background sample' (semi-log plot).

Table 8.2: D_s lifetime fit results

Parameter	Best Fitted Value
$c\tau$ (μm)	$135\ ^{+40}_{-30}$
s	$1.17\ \pm 0.09$
f_{bg}(%)	$45.6\ \pm 1.3$
λ_+(μm)	$129\ \pm 48$
α_+(%)	$33\ \pm 8$
λ_-(μm)	$633\ \pm 116$
α_-(%)	$14\ \pm 2$

the signal plus background contributions are also plotted. The value of the fitting function at any point x is calculated using $s\sigma_{\ell_B}$ of the data and summing over all the events in the sample. The background sample ℓ_B distribution and the fitting function of the background are also shown in 8.2(b) and in Figure 8.3(b).

The proper length ℓ_D distribution can be used to measure the charm meson D_s^- lifetime. This can in fact verify the fitting method, and can also tell us if the sample really is $\ell^+ D_s^-$. The fitting procedure here is essentially the same except since $P_T(D_S)$ is measured, the distribution does not need to be corrected by K. The fitting range in this case is from -0.2 cm to 0.2 cm. The fit results are listed in Table 8.2. We

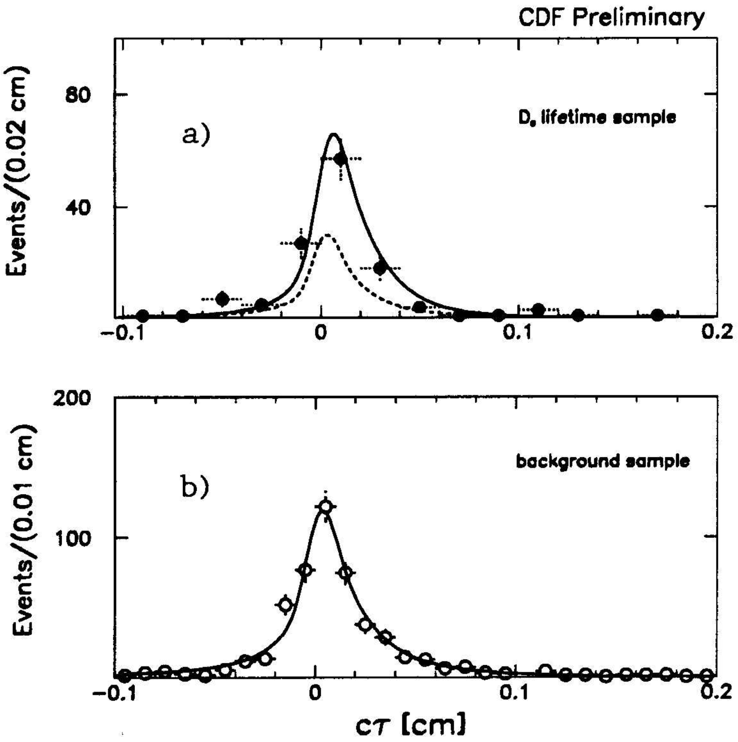

Figure 8.4: Distribution of $c\tau(D_s)$ (a) lifetime sample (b) background sample.

find that the lifetime of D_s is

$$\tau(D_s) = 0.45 \ \pm 0.10 \text{ ps.} \tag{8.13}$$

This is same as the world averaged D_s lifetime value quoted by the Particle Data Group[23]. The ℓ_D distributions of the signal and background samples along with the fitting functions are shown in Figure 8.4.

Chapter 9

Systematic Uncertainties

This chapter discusses the systematic uncertainty in the B_s lifetime. There are several sources which contribute to the systematics, namely the combinatorial background which is a large fraction of the signal sample and also the physics background which is small but important. The decay length resolution and the relativistic boost correction are both sensitive to the result. And the selection $L_{xy} > 0$ effect and the residual misalignment effect will also be included.

9.1 Combinatorial Background

The decay length distribution of the background events in the selected signal sample has to be determined in an unbiased fashion. Tails on the positive side are especially relevant to the measurement. The fit, combines both sideband events and events from wrong sign combinations in the background sample. The shape of the background is determined from the background sample above and the backgrounds in the signal sample. These regions are marked in Figure 7.4. The background shape is plotted

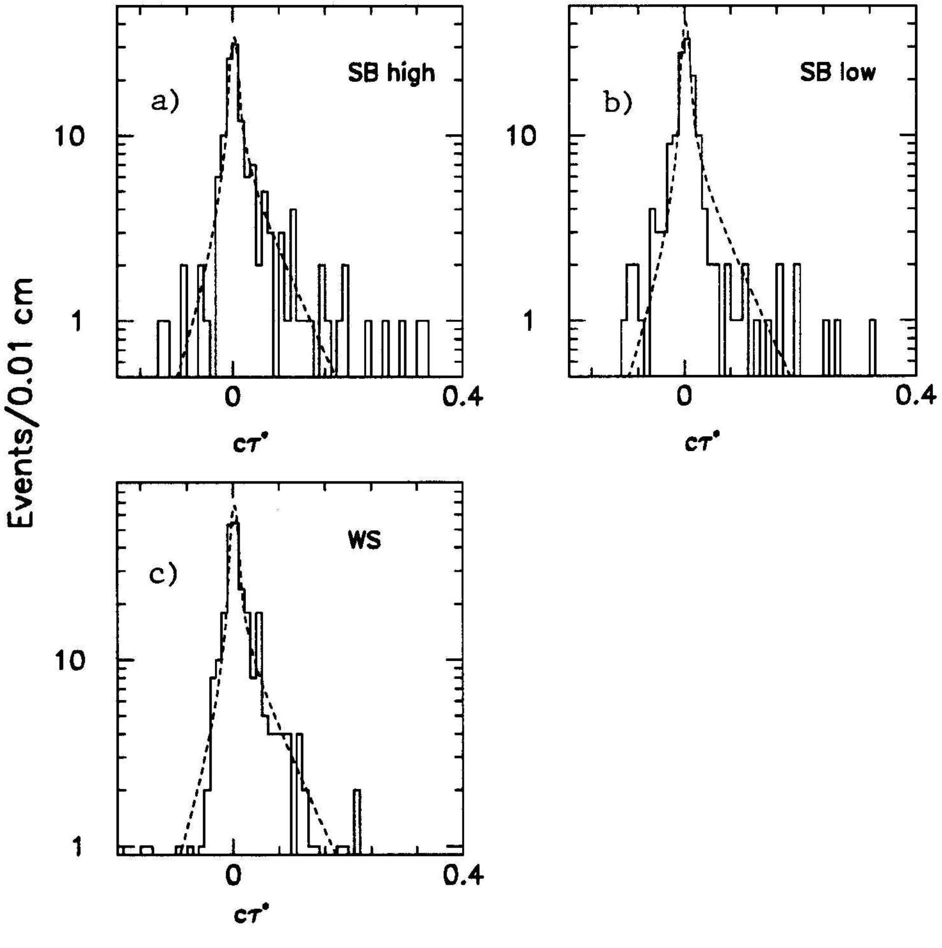

Figure 9.1: Distribution of ℓ_B from (a)High mass sideband,(b)Low mass sideband and from (c)Wrong sign. The curves are from the lifetime fit.

on top of the distributions for the sidebands and the wrong sign (see Figure 9.1) data for comparison. The background samples from the high mass sideband, the low mass sideband, and the wrong sign mass band can be studied separately, but in order to increase the statistics for each sample, wider mass windows are used. The three individual samples are

- right sign 1.99-2.2 Gev/c^2 (high mass)
- right sign 1.75-1.945 (excluding 1.854-1.886) GeV/c^2 (low mass)
- wrong sign 1.75-2.2 GeV/c^2

Parameters	High mass	Low mass	Wrong sign
$c\tau$	384 ± 69 μm	421 ± 73 μm	422 ± 72 μm
s	1.40 ± 0.11	1.53 ± 0.11	1.51 ± 0.09
λ_+	491 ± 116 μm	337 ± 80 μm	384 ± 88 μm
α_+	0.23 ± 0.04	0.28 ± 0.04	0.24 ± 0.03
λ_-	0.183 ± 0.049 cm	0.124 ± 0.022 cm	0.121 ± 0.02 cm
α_-	0.11 ± 0.02	0.11 ± 0.02	0.10 ± 0.02

Table 9.1: Fit results from using three different background samples

The lifetime fit results from using the three background samples are listed in Table 9.1. Half of the maximum difference between the lifetime results is used as the systematics error ie. ±18 μm or 4%.

9.2 Non Strange B Background

As mentioned before, a small fraction of the $\ell^+ D_s^-$ events are not from B_s semileptonic decays. They are the products of the non-strange B meson decays, and have been ignored in the lifetime fit because the number of such events is expected to be small. Since there is no measurement of their production, only fraction relative to the B_s signals are used here to estimate their contribution to the systematic error.

The background fraction from the decay process

$$B_{u,d} \rightarrow D_s^{-(*)} X_s \ell^+ \nu$$

should be limited by its small production cross-section. In chapter 7, this fraction is determined to be smaller than 2.6%. Given this limit, its contribution can be added into the $\mathcal{F}_{SIG}$ with the same function as the B_s signals and replace the $c\tau$ with the average b lifetime (1.5 ps). The systematic effect is less than 1% and can then be ignored in comparison to the other decay source,

$$B_{u,d} \rightarrow D_s^{+(*)} \overline{D}^{(*)}, \overline{D}^{(*)} \rightarrow \ell^- \overline{\nu} X.$$

For this background, the decay branching ratio $\mathcal{B}(B_{u,d} \rightarrow D_s^{+(*)} \overline{D}^{(*)})$, the semileptonic branching ratios of the D mesons, and the experimental acceptance relative to the B_s signals have all been used to derive the background estimate of 2.6%. This

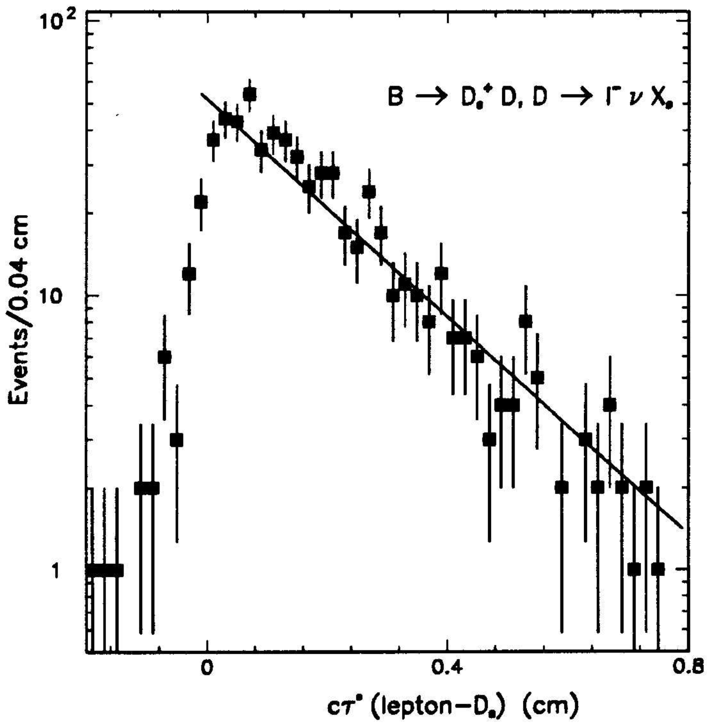

Figure 9.2: Distribution of ℓ_B from the Monte Carlo $B \to D_s^{(*)-} D^{(*)}, D^{(*)} \to \ell^+ \nu X$.

small background however has an impact on the result of the measurement. This has been studied by generating Monte Carlo events of this process and their pseudo-$c\tau$ distribution in exactly the same way as described earlier (see Figure 9.2). The distribution is parameterized as a single source with the decay function

$$\mathcal{G} \otimes \exp[-x/c\tau_{D_s D}]. \tag{9.1}$$

The pseudo-$c\tau$ distribution of this lepton-D_s system appears to be quite long compared to the average B lifetime of 450 μm used to generate the events. This is because (a) the lepton and the D_s do not originate from the same decay vertex, and (b) the momentum missing from the semi-leptonic D decay (carried by X) means the $P_t(B)$ is underestimated by the P_T of the lepton-D_s system. The $c\tau_{D_sD}$ is found to be about 0.206 cm. Including this extra source in the fit causes a 4% shift toward lower values for the B_s lifetime.

9.3 Decay Length Resolutions

In the unbinned log-likelihood fit, each decay length measurement has been smeared by a resolution function $G(\ell, s\sigma_{\ell_B}) = \frac{1}{\sqrt{2\pi(s\sigma_{\ell_B})}} \exp(-\ell^2/(s\sigma_{\ell_B})^2)$, where the σ_{ℓ_B} is the error of the decay length determined from the individual event reconstruction (see the appendix), and s is the scale factor for all the errors.

The Scale Factor

The uncertainty of the decay length is dominated by the uncertainty of the secondary vertex position which in turn is related to the error matrix of all the track parameters and the topology of the individual event. It may be under or over estimated. Because of this, a scale factor must be used. In the lifetime fit, this scale factor is allowed to float. The best fit result for s is 1.47 ±0.11. This suggests that the decay length errors are underestimated by about 30-50%. This scale factor can be checked independently

Table 9.2: The control sample and the electron-rich sample

Selection Cuts	Control Sample	Electron-rich Sample
HAD/EM	> 0.04	< 0.04
ShowMax/p*	< 0.4	> 1.0
PreShower/p*	< 3.0	> 8.0

with another 'control' sample. The control sample means a data sample which does not have real displaced secondary vertices other than the false ones caused by the resolution. To be useful, the event kinematics of this sample should be quite similar to the sample used for the lifetime measurement. As discussed in Chapter 4, the fake hadron residuals in the inclusive electron sample are nearly a good control sample. These are light quark hadronic events which are short lived and have similar kinematic properties to the prompt electrons. Such a control sample and an electron-rich sample (for the comparison) can be made from the inclusive electron data by selecting on the CES and CPR quantities as shown in Table 9.2 (see Chapter 4).

The $L_{xy}/\sigma_{L_{xy}}$ and L_B/σ_{L_B} distributions from the control sample shall be used to determine the scale factor. The fake electrons are first selected with the electron cuts described in Chapter 4, except for the HAD/EM cut which is not used. Then three tracks are selected in each event with the same quality and p_T requirements as described in Chapter 5, i.e.

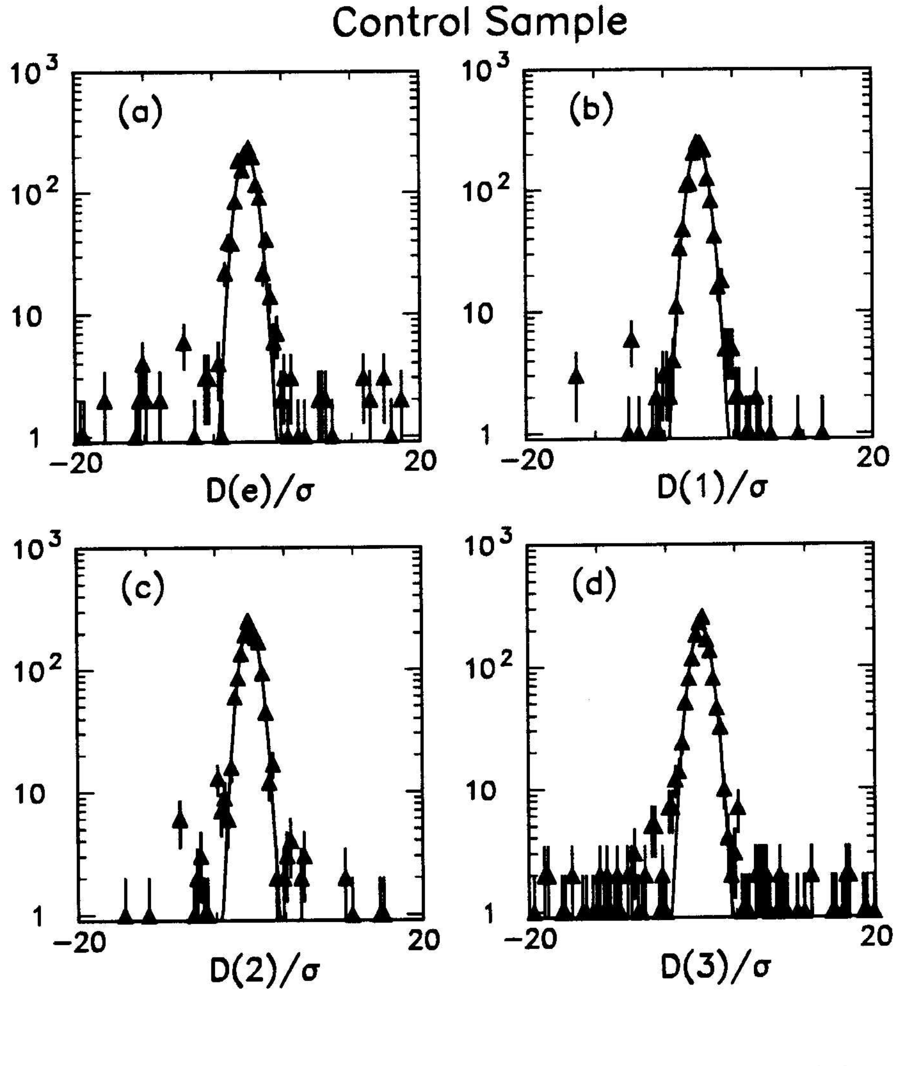

Figure 9.3: Impact parameter over its error for (a) fake electron candidate, (b) track 1 ,(c) track 2, (d) track 3

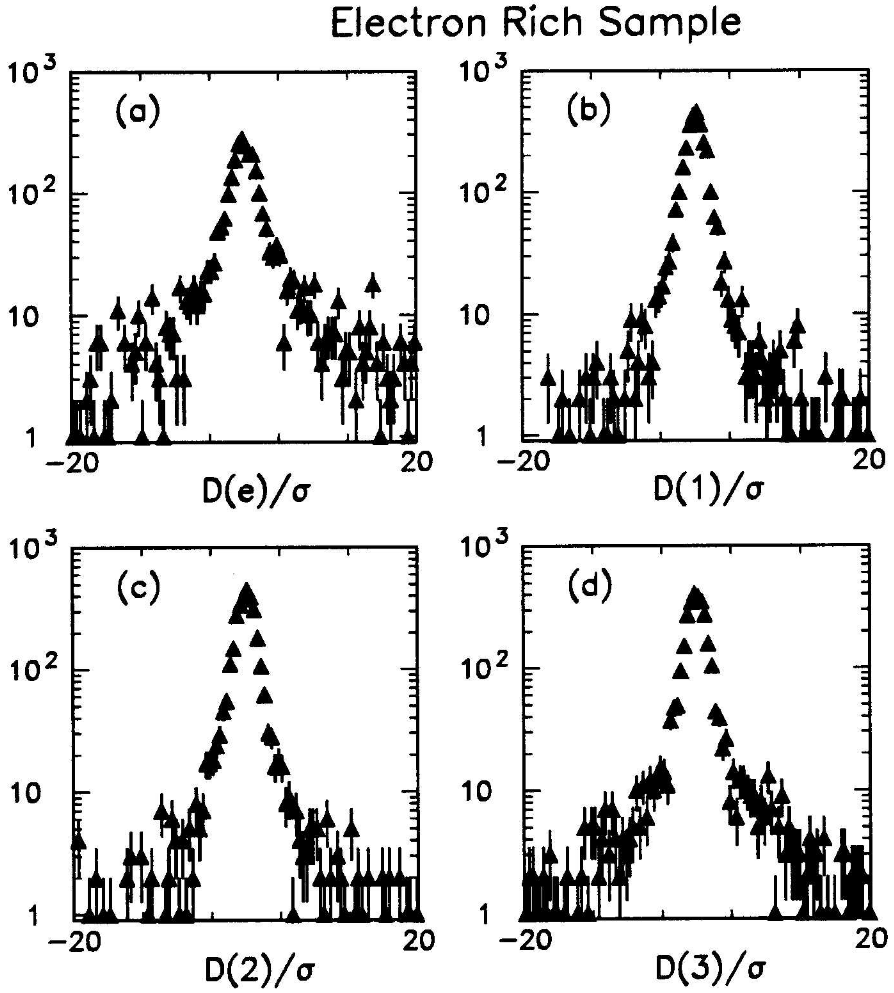

Figure 9.4: Impact parameter over its error for (a) electron candidate, (b) track 1 ,(c) track 2, (d) track 3

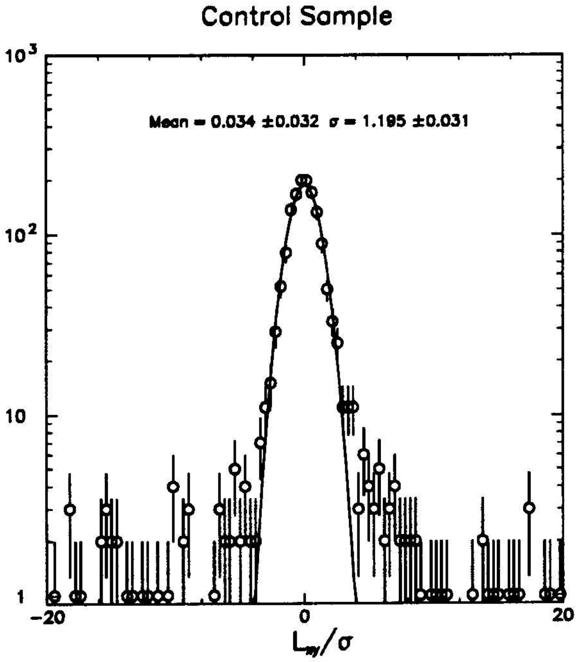

Figure 9.5: The decay length L_{xy} over its error for the control sample which consists of fake electrons.

- $P_t(K^+) > 1.0$ GeV/c, $P_t(K^-) > 1.0$ GeV/c and $P_t(\pi) > 0.8$ GeV/c
- At least 2 out of 3 tracks are:
  - SVX tracks with 2 or more hits and $\chi^2 < 30$.
  - Having ≥ 2 axial super-layers with at least 4 hits and ≥ 2 stereo super-layers with at least 2 hits.

These three tracks are vertex constrained and the probability of that fit is required to be larger than 1%. To convince ourselves that it has no lifetime, we plot the

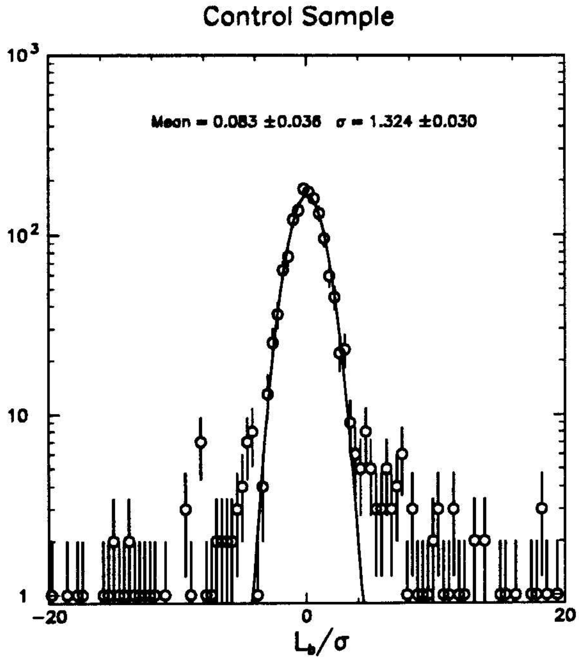

Figure 9.6: The decay length L_B over its error for the control sample which consists of fake electrons.

impact parameters over the errors for the fake electron and the three track candidates in Figure 9.3. Most of the events can be described by a zero centered gaussian distribution of width 1. This is what is expect for a control sample, consistent with no lifetime. The small fraction of residuals which are not consistent with the gaussian part can be real electrons from heavy quark decays. The comparison plot of the corresponding distributions from the electron-rich sample data is shown in Figure 9.4, where the wide distributions are caused by the events which have quite large impact parameters. Those electrons represent the long lived heavy quark decays.

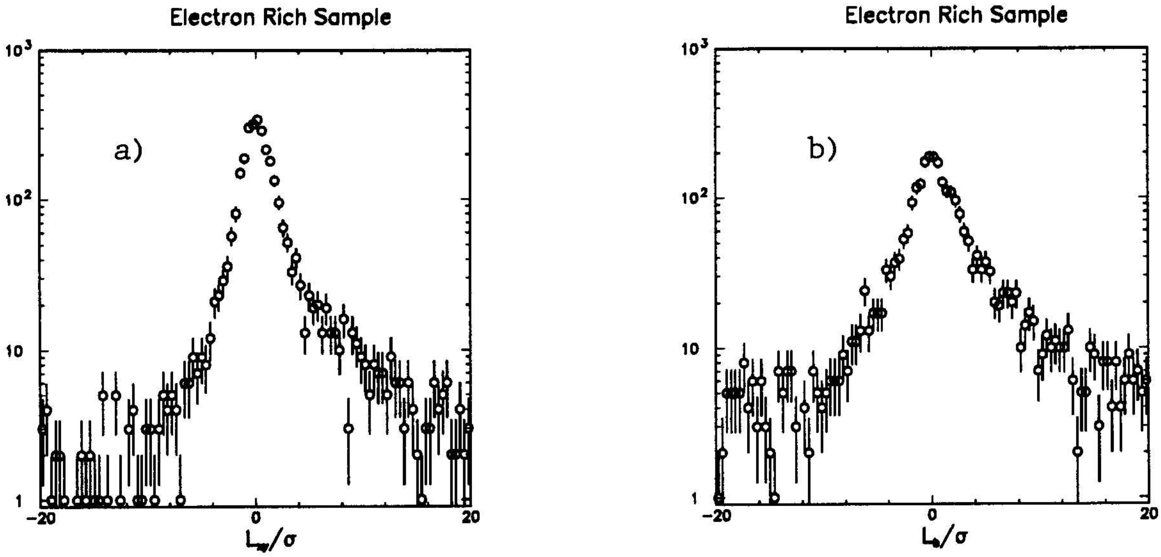

Electron Rich Sample

Electron Rich Sample

Figure 9.7: The decay length L_{xy} over its error (left) and the decay length L_B over its error (right) for the electron rich sample.

The L_{xy} and L_B from the control sample events are calculated the same way as in the lifetime data. The direction is the P_T of the fake electron-D_s system. The plots of the quantities over their errors are shown in Figures 9.5 and 9.6. If the real resolution is consistent with the calculated errors, one would expect the gaussian width to be unity. The measured widths are 1.20 ± 0.03 and 1.32 ± 0.03, respectively. The fact that they are not equal to unity indicates that the calculated errors of the decay length are under estimated. The scale factor (of L_B) seems to be consistent with the value determined from the lifetime fit. To compare, the same plots from the electron-rich sample data are shown in Figure 9.7(a)(b) where larger decay lengths are obviously noticed.

Measurements from both the control sample and lifetime sample have consistently pointed out that the decay length errors are underestimated. The cause of this can be complicated. The residuals used in the tracking may be overestimated. It could also be that the resolution function is more than a gaussian function. To evaluate the systematic effect however , we vary the scale factor from 1.0-2.0 and fix the value in the lifetime fit. The lifetime result changes by 10 μm or 2.5% over this range.

9.3.1 The Resolution Function

The lifetime fit assumed a single gaussian shape to describe the resolution of the decay lengths. The real data may however contain more than one source of error. As an alternative description, a double gaussian can be used.

$$f \cdot \mathcal{G}(\mathbf{s_1}\sigma) + (1 - f) \cdot \mathcal{G}(\mathbf{s_2}\sigma), \tag{9.2}$$

where $\mathbf{s_1}$ and $\mathbf{s_2}$ are the two different resolution scale factors. This form is used in the fit, and both scale factors are determined by the data. The result of the decay length fit changes by 4 μm or 1%.

In summary, we assign a total of 3% systematic uncertainty due to resolution effects.

9.4 Relativistic Boost Corrections

In semileptonic decays, the B meson momentum is not fully reconstructed. The relativistic boost effect is only partially removed event-by-event using the best estimator of the B transverse momentum, the P_T of the lepton-D_s. Inevitably we have to make an average P_T correction on an statistical basis with the distribution of

$$K = P_T(\ell D_s)/P_t(B_s).$$

This K distribution has to be obtained from Monte Carlo. It is in principle sensitive to changes from the following sources:

- The parent b quark momentum spectrum.
- The lepton selection.
- The fractions of the D_s^* and maybe the D_s^{**} in semi-leptonic B_s decays.

The standard bottom quark spectrum NDE[16] has been used. An earlier study of the electron p_T spectrum (see reference [26]) suggested a better fit to the data with a distribution which is steeper than NDE by the weight $1/p_T^{0.8}$ (see Figure 3.9). With this new spectrum for $p_T(b)$, one gets a slightly harder K distribution. As a consequence, the lifetime result is increased by about 6 μm or 1%.

The effects of the lepton trigger threshold and the lepton isolation cuts are also considered. Here a simple model is used to simulate the trigger turn on effect, a

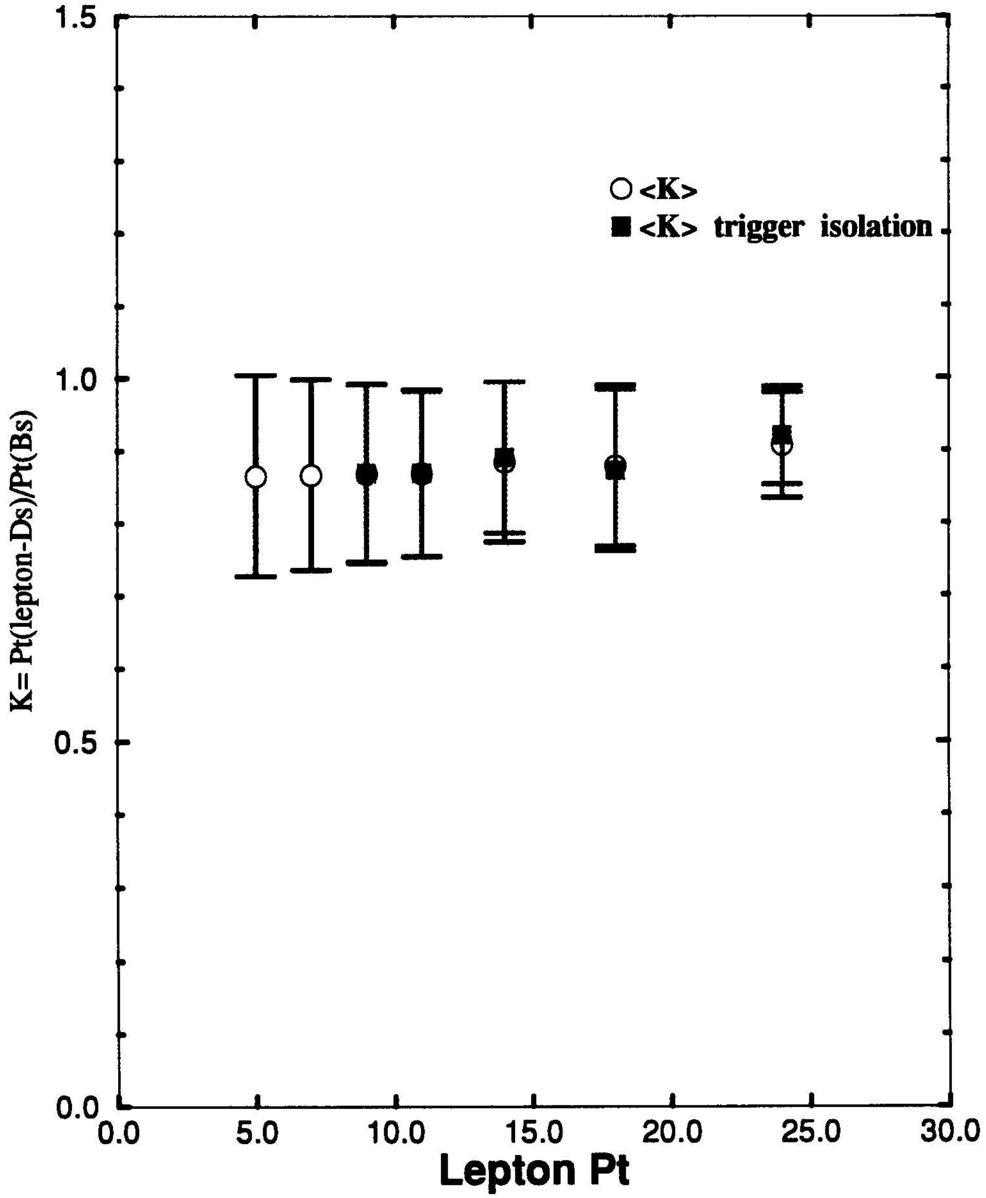

Figure 9.8: Mean of the $K = P_t(\ell^+ D_s^-)/P_t(B_s)$ as a function of the lepton p_T (circle). The effect of the trigger (9 GeV threshold) and the isolation of the lepton are shown as the square points.

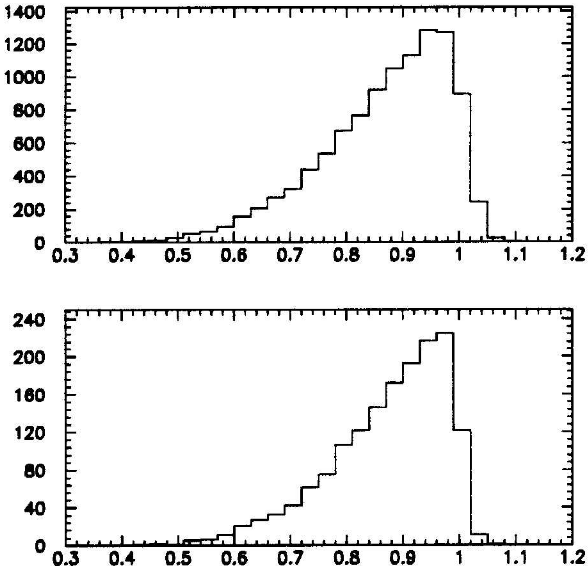

Figure 9.9: $P_t(l^- D_s^+)/P_t(B_s)$ distributions (a) No trigger or isolation requirement. (b) after requiring the lepton to be isolated and pass the 9 GeV threshold.

near-step function,

$$f = \frac{1}{1 + \exp(-(p_T - p_T^{th})/\Omega)} \tag{9.3}$$

where the p_T^{th} is the p_T threshold of the lepton trigger. The Ω represents the turn on resolution which is taken to be approximately 1 GeV/c. Electrons are classified as isolated if no other tracks are in the same electron tower. The K distributions are generated according to different bins of lepton p_T, one set with the trigger and isolation requirements and one set without. The mean and the RMS of each K distribution is then plotted as a function of the lepton p_T (see Figure 9.8). The result is a flat distribution which does not seem to be affected by either the isolation or

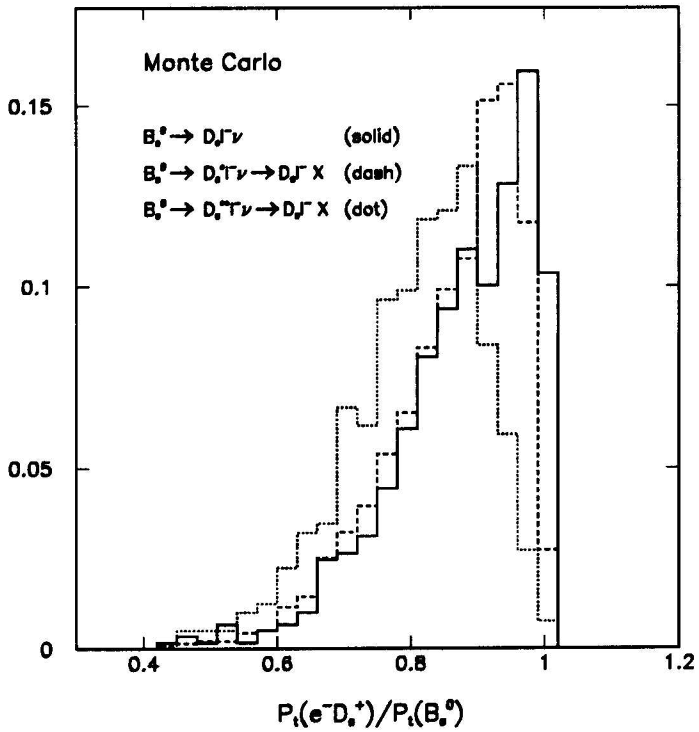

Figure 9.10: Distribution of 'K factor' for cases: (a) $B_s \rightarrow D_s \ell^- X$ (solid) (b) $B_s \rightarrow D_s^* \ell^- X$ (dash) (c) $B_s \rightarrow D_s^{**} \ell^- X$ (dot).

the trigger turn on of the lepton. The effect of the lepton selection makes the K distribution width slightly narrower (see Figure 9.9). The results of the lifetime fit using these two distributions for the boost correction only differ by 5 μm or 1%.

The contributions of the D^-, D^{*-} and possibly D^{**-} to the final state $\ell^+ D_s^-$ are clearly important in generating the K factor distribution. Shown in Figure 9.10 are the three distributions normalized to an area of 1 from each of the following exclusive channels:

$$
\begin{aligned}
B_s &\rightarrow D_s^- \ell^+ \nu \\
B_s &\rightarrow D_s^{*-} \ell^+ \nu, D_s^{*-} \rightarrow D_s^- X \\
B_s &\rightarrow D_s^{**-} \ell^+ \nu, D_s^{**-} \rightarrow D_s^{*-} \gamma, D_s^{*-} \rightarrow D_s^- X \qquad (9.4)
\end{aligned}
$$

The differences between the first and second channels are small. The mean is quite lower however for the third case. On the other hand, due to the isospin symmetry, we expect most D_s^{**-} decay via

$$D_s^{**-} \rightarrow D^{(*)} K \qquad (9.5)$$

where $D^{(*)}$ here are non-strange D mesons. It is suggested that maybe only 20% of D_s^{**-} would decay to the D_s^- [25]. The CLEO decay table is used to generate K^{dist} and the fractions of the D_s^-, D_s^{*-}, D_s^{**-} are assumed to be 2/3: 1/3: 0. The mixture of D_s^- and D_s^{*-} is now varied between 0-100% and the D_s^{**-} from 0-20%. The K distributions from figure 9.10 are used. The B_s lifetime is changed by 6 μm or 1.4% as a result.

All three effects above are added in quadrature and a total systematic uncertainty of 3% is therefore attributed to the boost correction.

9.5 Selection Biases

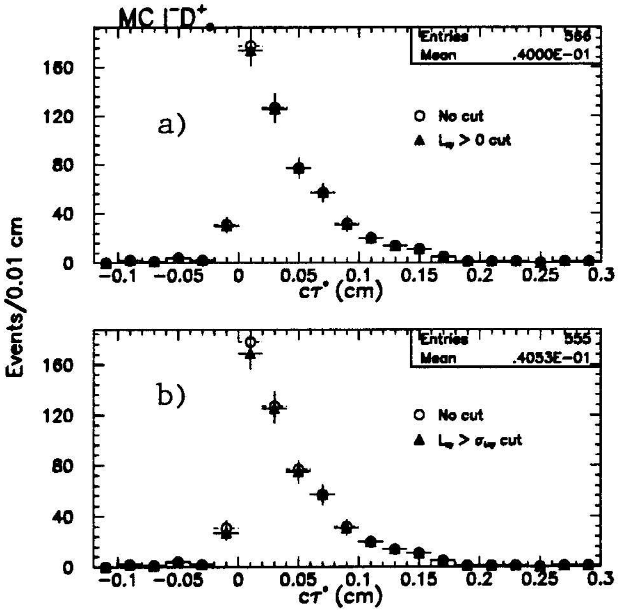

Figure 9.11: Monte Carlo distributions of the pseudo-$c\tau$ (a) without the L_{xy} cut (circle) and with $L_{xy} > 0$ cut (triangle). (b) without the L_{xy} cut (circle) and with $L_{xy} > \sigma$ cut (triangle).

A positive value of the apparent decay length L_{xy} is required in the D_s selection. Since the measured decay length L_B is in principle correlated with L_{xy}, an $L_{xy} > 0$ cut may cause some systematic effect on the measurement. This effect can be studied by using a Monte Carlo where the full detector simulation is applied. Shown in Figure 9.11 are the pseudo-$c\tau$ distributions before and after the $L_{xy} > 0$ and $L_{xy} > \sigma_{L_{xy}}$ cuts. Also plotted in Figure 9.12 is the efficiency as a function of pseudo-$c\tau$. The efficiency is a little lower in the small $c\tau$ region. The fit results are given in Table 9.3 where the effect on the lifetime is up to 7 μm, or a relative 2% (the bottom lifetime of 350 μm is used). The assumed systematic uncertainty is 2% from this source.

Table 9.3: Fit results of the Monte Carlo sample with and without the L_{xy} cut

Parameter	No L_{xy} cut	$L_{xy} > 0$	$L_{xy} > \sigma_{L_{xy}}$
$c\tau$ (μm)	352	354	359
shift (μm)	-	+2	+7
shift/$c\tau$ (%)	-	+0.6	+2.0

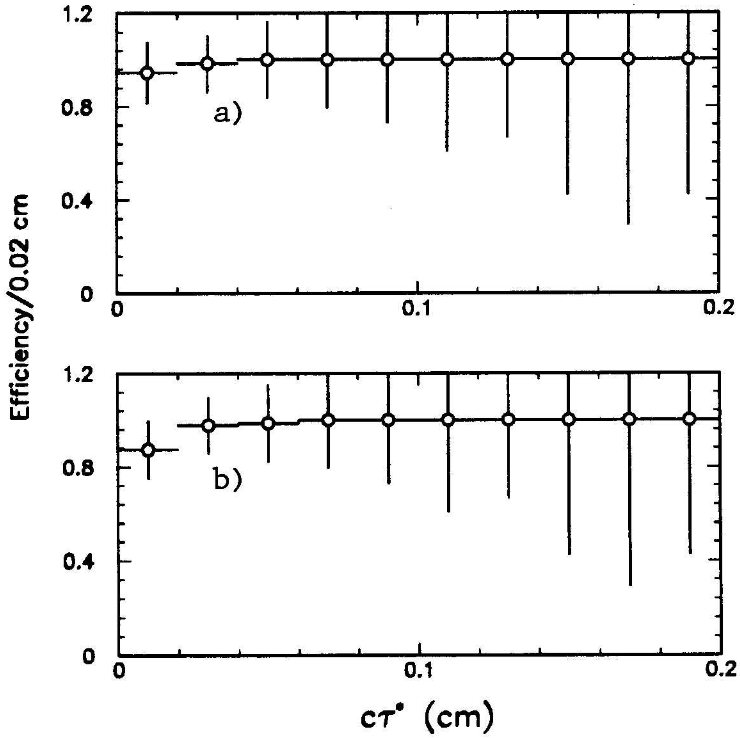

Figure 9.12: (a) Efficiency of the $L_{xy} > 0$ cut versus pseudo-$c\tau$. (b) Efficiency of the $L_{xy} > \sigma$ cut versus pseudo-$c\tau$.

9.6 Fit Method

The fitting program is tested by a simple Monte Carlo exercise. One thousand samples containing a mixture of signal and background events are generated. Each sample contains 139 events, while the background number is allowed to fluctuate according to Poisson statistics with a mean of 63. The decay lengths of the signal events are generated according to a pure exponential with mean lifetime of 426 μm and then are smeared by both resolution effects and the momentum correction factor K. Background events are generated by the probability density function $\mathcal{F}_B$, where the parameter values are fixed to those of the real data, given in Table 8.1. The generated decay distributions are then fitted by the same program to obtain the lifetime. The distribution of the fitted lifetimes is shown in Figure 9.13. The mean value is shifted by -10 μm from the input value of 426 μm. The statistical error on the Monte Carlo number is about ± 6 μm. Therefore ± 6 μm is used as a systematic uncertainty.

9.7 Residual Misalignment

The effect of residual misalignments in the SVX has been studied in the inclusive lifetime analysis[27] where the the wedge dependent offset has been evaluated from the wedge-by-wedge average of the impact parameter distribution with respect to the beam position as observed with W electrons. This yields a 2% systematic uncertainty in the lifetime result.

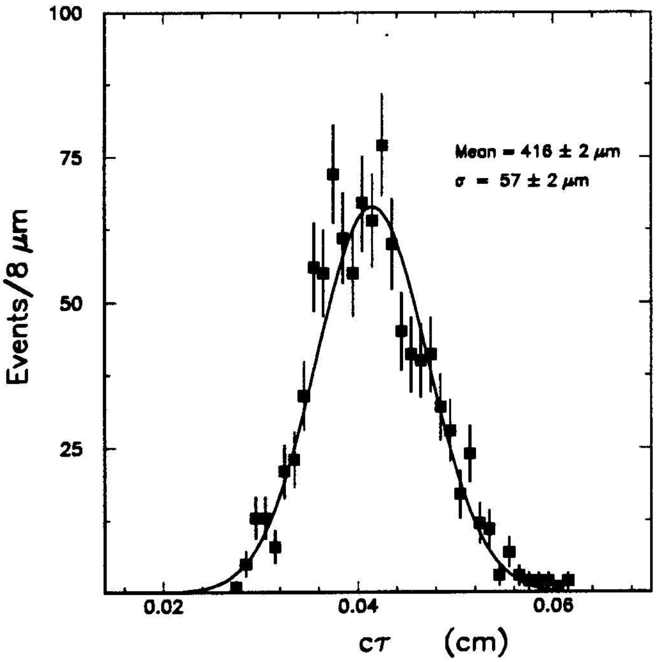

Figure 9.13: Fitted $c\tau$ distribution for MC samples generated with lifetime of 426μm.

All systematic sources and their contributions to the systematic error are summarized in Table 9.4. Assuming all of them are uncorrelated, they are add in quadrature which results in a 7% total systematic uncertainty on the B_s lifetime measurement.

Table 9.4: The systematic uncertainty and its sources

Systematic Source	Uncertainty
Combinatorial background	4%
Non-B_s background	4%
Decay length resolution	3%
Boost correction	3%
Selection bias	2%
Fitting method	1%
Misalignment	2%
Total	7%

Chapter 10

Conclusions

10.1 Summary of Lifetime Result

This thesis presents the first B_s meson lifetime measurement in a hadron collider. Semileptonic decay events of the B_s have been isolated from a total luminosity of 21 pb^{-1} $p\bar{p}$ collisions with the lepton-D_s correlation. Using both electron and muon data, 76±8 $\ell^{\pm} D_s^{\mp}$ events have been found after background subtraction. Other non-B_s background sources are estimated to be negligible ($< 5\%$). The result of the measurement of the lifetime of the B_s meson is

$$\boxed{\tau_{B_s} = 1.42\ ^{+0.27}_{-0.23}\ (\text{stat.})\ ^{+0.11}_{-0.11}\ (\text{syst.})\ \ \text{ps.}} \tag{10.1}$$

The error on the result is dominated by the statistical uncertainty which is $\sim 18\%$.

As a consistency check, the D_s lifetime has also been obtained from the same data sample to be

$$\tau_{D_s} = 0.45\ ^{+0.13}_{-0.10}\ (\text{stat.})\ \ \text{ps.} \tag{10.2}$$

Here, we ignore the systematic uncertainty. This result is consistent with the world average D_s^- lifetime 0.45 ± 0.03 ps.

10.2 B_s Lifetime From Around the World

Our B_s lifetime result can be compared with similar measurements made by other experiments around the world (see Figure 10.1). Table 10.1 lists all such measurements. These results are very recent. The average value can be obtained by minimizing the χ^2, i.e.

$$\chi^2 = \sum_i \frac{(\overline{\tau}_{B_s} - \tau^i_{B_s})^2}{{\sigma^i_\tau}^2}. \tag{10.3}$$

The averaged B_s lifetime is 1.45 ± 0.16 ps and the χ^2 per degree of freedom is 0.95. Within errors, the B_s lifetime is consistent with both the B_u and B_d lifetimes (see Table 1.2) and also with the average B hadron lifetime (Table 1.1).

10.3 Future Prospects

So far, only the $D_s^- \to \phi\pi^-$ channel was used in reconstructing the D_s. As listed in Table 5.2, there are a few more channels which may be used to increase the sample statistics. The channel $K^{*0}K^-$ may have an efficiency similar to the $\phi\pi^-$ mode, but the background is expected to be higher due to the broader K^{*0} width. Reflection from $D^- \to K^{*0}\pi^-$ where the π^- is mis-identified to be a K^- has to be considered. $K-\pi$ separation using dE/dx may help. The channel $K^{*-}K^0$ seems to be much less

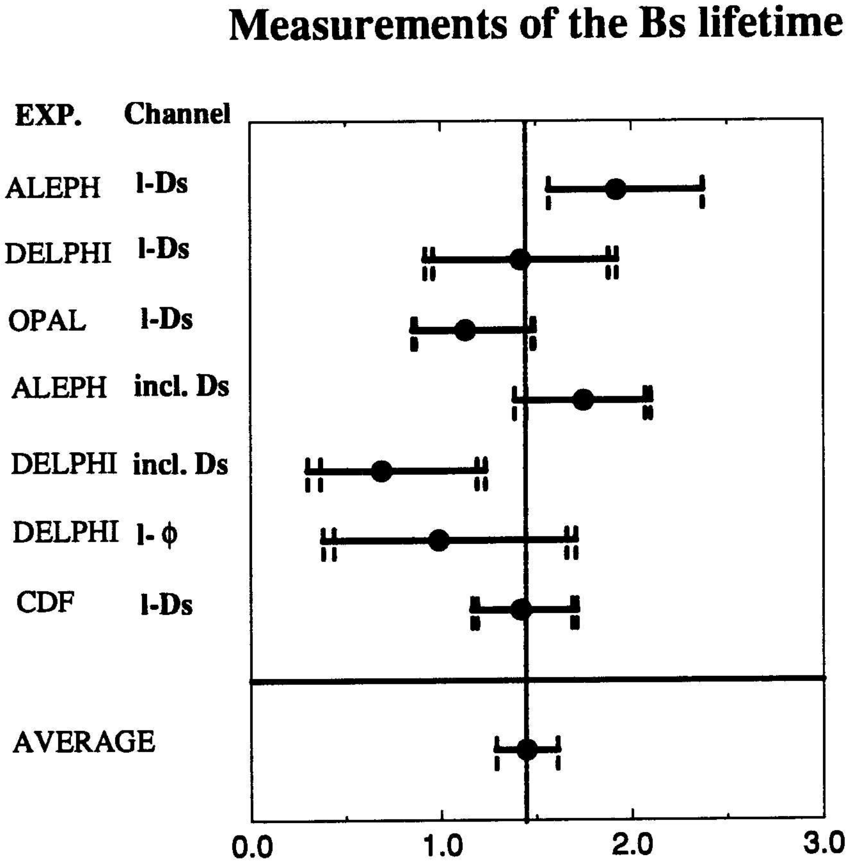

Figure 10.1: A list of the B_s lifetime measurements from around world

efficient than the channel K^-K^0 because of high multiplicity.

Because B_s^0 and $\overline{B}_s^0$ are both CP mixture states, the lifetime measured in the semileptonic decay mode has contributions from both the CP even and odd lifetimes. In order to compare the difference between these two lifetimes, the exclusive decay mode $B_s \rightarrow J/\psi\phi$ can be used. Since $J/\psi\phi$ decays are dominated by the CP even states, ignoring CP violation, this mode measures the $B_{s,\mathbf{short}}$ lifetime. In the present CDF data, only $\sim$ 10 good $J/\psi\phi$ signals have been located inside the SVX. The

Expt.	Ref.	Channel	B_s lifetime (ps)
ALEPH	PPE/93-214	$\ell^+ D_s^-$	$1.92\ ^{+0.45}_{-0.35} \pm 0.04$
DELPHI	Moriond-94	$\ell^+ D_s^-$	$1.42\ ^{+0.46}_{-0.46} \pm 0.20$ †
OPAL	PLB312,501	$\ell^+ D_s^-$	$1.13\ ^{+0.35}_{-0.26} \pm 0.09$
ALEPH	Moriond-94	incl. D_s	$1.75\ ^{+0.32}_{-0.30}\ ^{+0.14}_{-0.20}$
DELPHI	Moriond-94	incl. D_s	$0.69\ ^{+0.50}_{-0.32} \pm 0.22$ †
DELPHI	Moriond-94	$\ell\phi$	$0.99\ ^{+0.67}_{-0.55} \pm 0.26$ †
CDF	Moriond-94	$\ell^+ D_s^-$	$1.42\ ^{+0.27}_{-0.23} \pm 0.11$
Average(χ^2/dof)			1.45 ± 0.16 (0.94)

Table 10.1: A list of the B_s lifetime measurements. †scaled with the $\tau_b = 1.54$ps.

resulting lifetime, 1.74 $^{+0.90}_{-0.60}$ (stat.) $\pm$ 0.07 (syst) ps, has poor statistics. However, it is plausible to measure the $\Delta\tau_{B_s}$ in the future when more data are available.

Appendix A

Error Matrices of the V_B

The error matrix of the secondary vertex $\mathbf{M}(V_B)$ is in principle related in the transverse plane to a covariant matrix $\mathbf{G}^{-1}$ which includes the $\mathbf{M}(V_D)$ and the matrix of the lepton track parameters, ie.

$$\mathbf{M}(V_B) \;=\; \Lambda \times \mathbf{G}^{-1} \times \Lambda^T, \tag{A.1}$$

where the Λ is an error transform matrix which will be derived in the following.

The position of the secondary vertex V_B depends in principle on the coordinates (X_D, Y_D) of the V_D, the curvature C_D of the D, the azimuthal angle ϕ_D^0 of the D at V_D, the impact parameter d_ℓ of the lepton, the curvature C_ℓ of the lepton, the azimuthal angle ϕ_ℓ^0 of the lepton at the closet approach point.

The lepton and the D meson trajectories are described by the following equations:

$$\begin{cases} X_B &= r_\ell \sin\phi_\ell - (r_\ell + d_\ell)\sin\phi_\ell^0 \\ Y_B &= (r_\ell + d_\ell)\cos\phi_\ell^0 - r_\ell \cos\phi_\ell \end{cases} \quad \text{(for the lepton)}$$

$$\begin{cases} X_B & = X_D + r_D \sin\phi_D - r_D \sin\phi_D^0 \\ Y_B & = Y_D - r_D \cos\phi_D + r_D \cos\phi_D^0 \end{cases} \quad \text{(for the D meson)}$$

where $\phi_D - \phi_D^0 = -2C_D L_D$ and $\phi_\ell - \phi_\ell^0 = 2C_\ell S_\ell$. The L_D is the decay length of the D and the S_ℓ is the the travel length of the lepton between the closet approach point and the vertex point V_B.

The transform matrix elements can be calculated as

$$\Delta_1 \times \begin{cases} \frac{\partial X_B}{\partial X_D} & = \tan\phi_D \\ \frac{\partial X_B}{\partial Y_D} & = -1 \\ \frac{\partial X_B}{\partial C_D} & = -\frac{1-\cos(\phi_D-\phi_D^0)}{2C_D^2 \cos\phi_D} \\ \frac{\partial X_B}{\partial \phi_D^0} & = \frac{\sin(\phi_D-\phi_D^0)}{2C_D \cos\phi_D} \\ \frac{\partial X_B}{\partial d_\ell} & = \frac{\cos(\phi_\ell-\phi_\ell^0)}{\cos\phi_\ell} \\ \frac{\partial X_B}{\partial C_\ell} & = \frac{1-\cos(\phi_\ell-\phi_\ell^0)}{2C_\ell^2 \cos\phi_\ell} \\ \frac{\partial X_B}{\partial \phi_\ell^0} & = (r_\ell + d_\ell)\frac{\sin(\phi_\ell-\phi_\ell^0)}{\cos\phi_\ell} \end{cases} \qquad \Delta_2 \times \begin{cases} \frac{\partial Y_B}{\partial X_D} & = 1 \\ \frac{\partial Y_B}{\partial Y_D} & = -\tan\phi_D \\ \frac{\partial Y_B}{\partial C_D} & = -\frac{1-\cos(\phi_D-\phi_D^0)}{2C_D^2 \sin\phi_D} \\ \frac{\partial Y_B}{\partial \phi_D^0} & = -\frac{\sin(\phi_D-\phi_D^0)}{2C_D \sin\phi_D} \\ \frac{\partial Y_B}{\partial d_\ell} & = \frac{\cos(\phi_\ell-\phi_\ell^0)}{\sin\phi_\ell} \\ \frac{\partial Y_B}{\partial C_\ell} & = \frac{1-\cos(\phi_\ell-\phi_\ell^0)}{2C_\ell^2 \sin\phi_\ell} \\ \frac{\partial Y_B}{\partial \phi_\ell^0} & = (r_\ell + d_\ell)\frac{\sin(\phi_\ell-\phi_\ell^0)}{\sin\phi_\ell} \end{cases}$$

where $\Delta_1 = \tan\phi_D - \tan\phi_\ell$ and $\Delta_2 = \cot\phi_\ell - \cot\phi_D$.

To first order we are interested in the limit of $C_\ell \rightarrow 0$ and $C_D \rightarrow 0$, which is

$$\Delta \times \begin{cases} \frac{\partial X_B}{\partial X_D} & = \sin\phi_D^0 \cos\phi_\ell^0 \\ \frac{\partial X_B}{\partial Y_D} & = -\cos\phi_D^0 \cos\phi_\ell^0 \\ \frac{\partial X_B}{\partial C_D} & = -L_D^2 \cos\phi_\ell^0 \\ \frac{\partial X_B}{\partial \phi_D^0} & = L_D \cos\phi_\ell^0 \\ \frac{\partial X_B}{\partial d_\ell} & = \cos\phi_D^0 \\ \frac{\partial X_B}{\partial C_\ell} & = S^2 \cos\phi_D^0 \\ \frac{\partial X_B}{\partial \phi_\ell^0} & = S \cos\phi_D^0 \end{cases} \qquad \Delta \times \begin{cases} \frac{\partial Y_B}{\partial X_D} & = \sin\phi_D^0 \sin\phi_\ell^0 \\ \frac{\partial Y_B}{\partial Y_D} & = -\cos\phi_D^0 \sin\phi_\ell^0 \\ \frac{\partial Y_B}{\partial C_D} & = -L_D^2 \sin\phi_\ell^0 \\ \frac{\partial Y_B}{\partial \phi_D^0} & = L_D \sin\phi_\ell^0 \\ \frac{\partial Y_B}{\partial d_\ell} & = \sin\phi_D^0 \\ \frac{\partial Y_B}{\partial C_\ell} & = S^2 \sin\phi_D^0 \\ \frac{\partial Y_B}{\partial \phi_\ell^0} & = S \sin\phi_D^0 \end{cases}$$

where $\Delta = \sin(\phi_D^0 - \phi_\ell^0)$.

In a typical event $\delta X_D \sim \delta Y_D \sim L_D \sim S$ are about a few hundred micron to a few mm. In the CDF tracking, the error of the azimuthal angle ϕ is usually on the order of a couple milli-radians and error on the curvature is on the order of $10^{-4} - 10^{-5}$. Therefore we can see that the first order effect is mainly coming from the vertex position and the lepton impact parameter. The effect of the azimuthal angles of the D and lepton is next order. The error due to the curvatures are really negligible. We can simplify the Λ to a reduced form

$$\Lambda = \Delta^{-1} \times \begin{pmatrix} \sin\phi_D^0 \cos\phi_\ell^0 & -\cos\phi_D^0 \cos\phi_\ell^0 & L_D \cos\phi_\ell^0 & \cos\phi_D^0 & S\cos\phi_D^0 \\ \\ \sin\phi_D^0 \sin\phi_\ell^0 & -\cos\phi_D^0 \sin\phi_\ell^0 & L_D \sin\phi_\ell^0 & \sin\phi_D^0 & S\sin\phi_D^0 \end{pmatrix} \tag{A.2}$$

The reduced covariant matrix $\mathbf{G}^{-1}$ is

$$\mathbf{G}^{-1} = \begin{pmatrix} \mathbf{M}(V_D) & 0 & 0 & 0 \\ 0 & \sigma_{\phi_D^0} & 0 & 0 \\ 0 & 0 & \sigma_{d_\ell} & 0 \\ 0 & 0 & 0 & \sigma_{\phi_\ell^0} \end{pmatrix} \tag{A.3}$$

Bibliography

[1] N. Lockyer *et al.,* Phys. Rev. Lett. **51**, 1316 (1983).

[2] E. Fernandez *et al.,* Phys. Rev. Lett. **51**, 1022 (1983).

[3] H. Albrecht *et al.,* Phys. Lett. B **234** (1990) 409; *ibid.* **255** (1991) 297 D. Besson in Proceedings of the XVI International Symposium on Lepton and Photon Interactions, Cornell University, August 10-15, 1993.

[4] CLEO Collaboration, *A Measurement of* $BR(\overline{B}^0 \to D^{*+}\ell^-\overline{\nu})$, contributed paper to the 1993 Lepton and Photon Conference, August, 1993.

[5] R. Schindler, in *High Energy Electron-Positron Physics*, edited by A. Ali and P. Soding (World Scientific, Singapore, 1988), p. 234.

[6] N. Isgur,*et al.*, Phys. Rev. D **39** (1989) 799.

[7] I. I. Bigi *et al.*, CERN-TH.7132/94.

[8] S. R. Wagner, *et al.*, Phys. Rev. Lett. B **64** (1990) 1095.

[9] R. Aleksan *et al.*, Phys. Lett. B **316** (1993) 567.

[10] ALEPH collaboration, CERN-PPE/93-214.

[11] DELPHI Collab., P. Abreu *et al.*, CERN-PPE/93-176.

[12] OPAL Collab., P. D. Acton *et al.*, Phys. Lett. B. **312** (1993) 501.

[13] F. Abe *et al.,* Phys. Rev. Lett. **71** 1685 (1993).

[14] Y. Cen *et al.,QCD and High Energy Hadronic Interactions*, XXIXth Rencontres de Moriond, 1994.

[15] ALEPH collaboration, CERN-PPE/93-97.

DELPHI collaboration, CERN-PPE/94-22.

S. L. Wu, *Workshop on Physics at Current Accelerators and the Supercollider*, Argonne National Laboratory, 2-5 June, 1993.

[16] P. Nason, S. Dawson, and R. K. Ellis, Nucl. Phys. B **303** 607 (1988) ; Nucl. Phys. B **327** 49 (1989); Nucl. Phys. B **335** 260 (1990).

[17] Reference to specific charge state implies the charge-conjugate state as well.

[18] See F. Abe *et al.,* Nucl. Instr. and Meth. A271 (1988) 387 and references therein.

[19] D. Amidei *et al.,* Nucl. Instr. and Meth. A289 (1990) 388.

[20] P. Billoir *et al.,* Nucl. Phys. A **241** 115 (1985).

[21] C. Peterson *et al.*, Phys. Rev. D **27** 105 (1983).

[22] J. Chrin, Z. Phys. C **36** 163 (1987).

[23] Particle Data Group, K. Hikasa *et al.*, Phys. Rev. D **45**, (1992).

[24] ARGUS collaboration, Z. Phys. C **60** (1992) 11.

[25] E. Golowich,*et al.*, Z.Phys. C **48** (1990) 89.

[26] F. Ukegawa,*et al.*, CDF note 1862.

[27] F. Abe,*et al.*, Rev. Lett. **71** 3421 (1993).